INFORMATION TO USERS

THE UNIVERSITY OF OKLAHOMA

GRADUATE COLLEGE

A FULLY-COUPLED TWO-PHASE FLOW
AND ROCK DEFORMATION MODEL
FOR RESERVOIR ROCK

A DISSERTATION

SUBMITTED TO THE GRADUATE FACULTY

in partial fulfillment of the requirements for the

degree of

Doctor of Philosophy

By

MARISELA A. SANCHEZ DAGGER

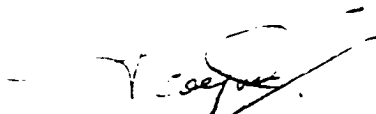Norman, Oklahoma

1997

UMI Number: 9808407

UMI
300 North Zeeb Road
Ann Arbor, MI 48103

A FULLY COUPLED TWO-PHASE FLOW
AND ROCK DEFORMATION MODEL
FOR RESERVOIR ROCK

A DISSERTATION
APPROVED FOR THE SCHOOL OF PETROLEUM &
GEOLOGICAL ENGINEERING

BY

Dedicated to my grandmothers Celia and Rosa, my mother Amanda and my daughters Hojamanda and Irene.

Acknowledgments

I would like to express my gratefulness to INTEVEP, S.A., PDVSA affiliate, for funding my studies at the University of Oklahoma. Thanks to those people who believed in me and gave me the opportunity to pursue my doctoral studies: Mr. Gustavo Inciarte, Dr. Hans Krausse, Mr. Jesús Bolívar, Dr. Carlos Espinoza, and Dr. Raúl Abreu.

My sincere and deep gratitude go to my advisor, Dr. Jean-Claude Roegiers, and other members of my doctoral committee: Dr. David Stearns, Dr. Roy Knapp, Dr. Djebbar Tiab, and Dr. Charles Bert.

Dr. Roegiers' encouragement and his "don't give up's" coming from overseas were really an empowerment to me. I acknowledge his technical and personal support in every detail of my career from the very beginning. His personality and driving force have been an inspiration to me.

I will be ever thankful to Dr. Stearns for devoting many of his "after retirement " days to put this document into a professional format. I enjoyed and appreciated his many technical and non-technical lessons very much and, as many other students, I consider him the best professor I have ever had.

Also, I want to thank Dr. Knapp, Dr. Tiab, and Dr. Bert for helping me accomplish this last part of my studies by making suggestions, raising questions, and reviewing the document.

In addition I must express my gratitude to my fellow students: Freddy Escobar, Sergio Berumen, Ion Ispas, Sandro Gasbarri, Ahmad Ghassemi, Steve Webber, Mazen Kanj, Yanguang Yuan, and See Hong Ong for so many intelectual and personal exchanges from which I have learned so much.

From the Rock Mechanics Group staff, my appreciation goes to Carla Cates, who helped me with family and living matters, and Don Cruickshank for his willingness tohelp. Also, smiles and friendliness from Patti, Leslie, Sharon, Anne and lately Meegan, Tammie and Haruko have meant a lot to me. Dr. Younane Abousleiman, Dr. Dezhang Lin and Dr. Thurman Scott are also acknowledged for their technical support.

But the most important driving force has been my family. For their patience and understanding of the many hours taken away from them, I give them my tribute and share this accomplishment. Now I can address that one-million-times-asked question: Are you done with your thesis, Mom? Finally the answer is YES!!. Adolfo, my husband, supported my efforts every moment, helped me with his guidance, reviewed my derivations, checked my code, ...and loved me, too. My parents and relatives were always ready to help me in every manner.

Mainly, I thank God for giving me the opportunity of meeting all these wonderful people who have enriched my life so much.

Contents

Please Note

Page(s) not included with original material and unavailable from author or university. Filmed as received.

ix

UMI

x

List of Figures

xiii

Abstract

In the application of most of the reservoir rock models to specific real engineering problems, the role of reservoir rock is frequently limited to its storage and delivery capabilities; the interaction of fluid flow with rock deformation has been, for the most part, ignored. However, coupling of fluid flow and rock or soil matrix deformation has recently become more and more of interest in many problems in petroleum, civil, environmental, geological and mining engineering. Efforts are currently being addressed to the development of fully coupled thermal-fluid flow-mechanical models to more realistically represent natural geological systems. In the oil industry, problems such as ground subsidence, reservoir compaction, borehole stability, sanding and hydraulic fracturing need to be addressed with a coupled approach to make predictions more accurate than when each process is considered to be independent of the other.

In this frame of reference, here a two-dimensional explicit Lagrangian finite-difference code, fully-coupled with a two-fluid flow system in porous media, is developed. The solid deformation is considered using the dynamic

relaxation procedure which allows the model to go into post-peak behavior of the material without creating instability. This method is particularely powerful when deformation is by nonlinear/failure systems (i.e. work softening plasticity).

The code consists of two parts: one mechanical and one fluid flow. The mechanical calculations essentially solve motion equations with a damping factor by using several pseudo-time steps until equilibrium is reached. Strains are determined from displacements and the corresponding stress field calculated through a constitutive equation. The steps required to reach equilibrium are not real time steps but, rather, represent the path that the structure follows to obtain the equilibrium state.

Coupling the mechanical response with fluid flow is done through monitoring changes in pore pressure. The mechanical part considers undrained pore pressure and saturation changes occuring due to volumetric strain in the solid. Once mechanical equilibrium is reached fluid flow is allowed for a particular real time step. The fluid flow during any real time step puts the system out of equilibrium and a new set of mechanical steps is required to bring the system back to equilibrium which, in turn, produces new displacements and stresses within the body.

The fluid flow equations are written using mixing laws and the solid is treated as another phase. The system of nonlinear equations is numerically solved using Newton's iteration, or a staggered algorithm, to obtain the pri-

mary variables (pore pressure and water saturation). Newton's iteration is used for longer times when bigger time steps are required and the staggered algorithms are more economic for short times, with smaller time steps.

The code is tested against analytical solutions for single phase flow with consolidation. Examples of coupled fluid flow and rock deformation for a simple one-dimensional scenario, as well as for more compex cases such as a layered oil reservoir compaction are presented. The code is able to successfully handle nonlinearities in fluid flow properties and a work-softening constitutive equation for the solid matrix. The mutual relationship among variables such as saturation, pore pressure and displacements is shown. It is also demonstrated that coupling is an important issue to be considered in compaction problems. Actually, the commonly used staggered procedure of transfering information from a fluid flow code to a stress-strain module can never reproduce the essential physics involved in reservoir compaction.

Chapter 1

Introduction

1.1   Research motivation

Coupling of fluid flow and matrix deformation is of great interest in many problems related to petroleum, civil, environmental, geological and mining activities, in which interactions between single or multiphase flow and deformation of the rock or soil masses are to be considered. In the oil industry, the effects that production of oil, gas and/or water from subsurface reservoirs has on rock deformation and the in situ state of stress are important issues. Reservoir deformation is responsible for changes in rock porosity and permeability and, consequently, can have a marked influence on the fluid flow characteristics. The fluid flow and deformation effects are coupled, e.g. one process influences the other and the overall response can not be predicted with confidence by considering each process independently. Surface subsidence as a result of reservoir compaction during hydrocarbon production is one example of a common problem involving a coupled rock deformation-

1

fluid diffusion process. Other examples are: a) wellbore stability; b) sand production control; ; c) stability of perforations; d)hydraulic fracturing; e) clean-up of contaminants in the rock mass; and, f)waste disposal in deep deposits.

In reservoir models and/or simulations, the role of the reservoir rock is often limited to their storage and delivery capabilities [73]. Interaction between fluid flow and rock deformation has, for the most part, been ignored. Variation of pore volume is considered only through the conventional rock compressibility parameter, C_R [5]. This means that any nonlinear, time-dependent, mass behavior of the rock matrix has been disregarded thus reducing matrix deformation to a single parameter, C_R, which in most cases is considered to be constant. If non-linear behavior of the matrix is important, as it is in high porosity nearly consolidated reservoir rocks, assumptions of linear behavior uncoupled with fluid flow may considerably limit the value of model solutions. Hence, evaluating the relevance of coupled, nonlinear processes, determining the extent to which they are important in time and space, and when they may be safely ignored safely are key points of this investigation.

To gain insights into the importance of the deformation-diffusion phenomena for a particular application, several tools can be used:

1. field evidence of nonlinear rock deformation and failure (subsidence, borehole instabilities, sanding, changes in in-situ stresses over the life-

time of the reservoir);

2. laboratory tests of fluid saturated rock samples subjected to fluid flow that imply nonlinear deformation and/or coupling between fluid flow and matrix deformation; and,

3. mathematical models that do incorporate the coupling of multiple phase flow with the rock stress-strain behavior.

It is number 3, the mathematical modelling aspect, that is addressed in this dissertation. However, in order to identify relevant effects that ought to be incorporated in the mathematical models, the other two issues need to be studied. Certainly the dependency in some cases of permeability on pore pressure changes and on strain has been stablished [63]).

Recently there has been some effort to develope a fully-coupled thermal-hydraulic-mechanical model that realistically represents a geological system. One example of this is the DECOVALEX project which is an international multidisciplinary effort in this direction [54]. This project is oriented towards the design of underground repositories. In order to analyze such a disposal system, which is also safe, required the coupling of rock mass stability, groundwater flow, external stresses and thermal into the model.

Other existing coupled multiphase stress-flow models are based on either a fully-coupled approach or a modular structure [99]. Li and Zienkiewicz [66], Li et al. [65], Zienkiewicz and Shiomi [131], Lewis and Schrefler [61]

3

have developed fully-coupled, finite element models. These models, based on Biot's poroelasticity theory, together with 'mixture' theory, consider three-phase immiscible flow. Tortike and Ali [121], present a model that considers non-isothermal flow for cyclic steam injection applications. These models possess the accuracy and versatility offered by the finite element method, but the large computational and developmental efforts required limit their use in reservoir simulations [99].

In the modular approach, conventional stress analysis codes can be used in conjunction with a standard reservoir simulator. The compatibility between the modules is based on a modified and extended expression to account for the pore volume changes in the reservoir (Settari [99]). Variables are calculated independently in the stress and flow modules for each time step, and information is traded between them; coupling is performed incrementally by iterating between modules until convergence is achieved for each time step.

Examples of such a modular approach include thermal recovery of heavy oils (Settari [99], Tortike and Ali [120], Fung et al. [37]) and integrated fracture mechanics-consolidation (Settari [100]). Settari [99] uses a three-dimensional finite element code for a linearly elastic rock and a finite difference-based fluid flow simulator. In this application it was found that the solid mechanics calculation dominates in terms of computer time and memory. This is because of the finer discretization needed to achieve sufficient accuracy in the solid mechanics calculations and because direct solvers are typically used

4

in finite element codes as opposed to more efficient iterative solvers which are common in reservoir engineering codes. This is aggravated when nonlinear rock behavior is to be considered since, in such cases, additional iterative or incremental calculations are required to follow nonlinearities. Moreover, work-softening, post-peak behavior, characterized by a down-sloping segment in the stress-strain curve of the rock, is extremely difficult to use with finite elements.

From what has been discussed, it seemed that more research was needed concerning a methodoly that could be *practically* applied to model multi-phase flow coupled with consideration of non-linear behavior of the porous rock media. The fundamental reason for this is the intrinsic complexity in modelling a nonlinear, work-softening, plastic rock behavior. Under this set of circumstances, the explicit Lagrangian finite difference technique with dynamic relaxation was thought to be an alternative worth trying in the treatment of coupled nonlinear matrix deformation-fluid diffusion problems, because of its inherent efficiency when large strain problems, or situations in which physical instability of the solid (failure) may occur [25], [58], [105].

1.2   Proposed approach

To consider coupled deformation-diffusion processes for multiphase flow (the solid being one of the phases), an approach based on the explicit Lagrangian finite-difference technique for the stress-strain analysis is proposed. The main

5

features of the this technique are the following:

- Lagrangian formulation for the solid strain field;

- explicit integration of the motion equation (Newton's second law);

- use of the dynamic relaxation technique;

- use of a finite difference scheme based on contour integrals (using the Gauss divergence theorem) for both fluid flow and solid deformation.

Applying this procedure to multiphase flow implies: a) expressing solid deformation and fluid flow equations in terms of the finite difference scheme characteristic of this method, b) coupling solid deformation and fluid flow by including the momentum balance of the mixture (instead of the solid alone) in the motion equation , and by introducing the undrained pore pressure generation during the dynamic relaxation procedure, and c) solving the flow.

The code developed here is restricted to plane strain deformation of the rock, and two-dimensional two-phase flow equations for immiscible fluids. Darcy's flow is assumed to hold and relative permeability and capillary functions of saturations are used.

Even though the approach presented here resembles the idea of a modular approach, it actually accounts for the coupling of the processes using rigorous poroelasticity and mixture theory equations as is done in fully-coupled models.

6

One key feature of the numerical approach used here, is the concept of the dynamic relaxation as introduced by Day [28] and Otter et al. [81] for structural mechanics. The dynamic relaxation technique is a procedure that solves the dynamic equations of motion using a damping factor such that at the limit static, or steady-state, equilibrium is obtained. The time involved in the 'dynamic' calculation is artificial; it is only a time intended to let the system vibrate to achieve balance of forces. By the use of the dynamic relaxation procedure, the momentum equation is approximated in a global manner, rather that locally. Therefore, discontinuities in the stress field will not affect the stability of the numerical calculation. Constitutive models with the complete stress-strain behavior can be considered even if the stress-strain curve has a negative slope following some peak stress difference (work-softening). The inclusion of the inertial terms allows the generation and dissipation of kinetic energy to be directly considered as they are in a physical system. Hence, rupture propagation, which can give rise to the generation of slip surfaces, can be modelled without loss of stability. It has been found that many finite element methods, at best, are difficult to use and, at worst, inaccurate when applied to problems in which deformation is localized, i.e. when shear bands occur.

The explicit integration of the motion equation implies that calculations are done with known information from the immediately surrounding elements or nodes. If the time step is small enough, only the surrounding nodes

7

will have an influence. Therefore, there is an optimum speed at which the information can propagate into a particular mesh, and this speed should be maintained ahead of the physical wave speed for stability. Actually, the Courant condition [4] expresses this fact and if the time step exceeds this condition, the scheme will be unstable.

The explicit scheme for invoking the stress-strain behavior of the rock has the advantage of not requiring large matrices to be stored and inverted. Therefore, memory requirements are small. However, the price paid is that small time steps are required and, consequently, a large number of iterations are demanded. This is why explicit methods are best for nonlinear, large strain problems that may undergo physical instability. Explicit methods, however, are not efficient for modelling

linear, small strain systems. The explicit scheme is only used for the solid mechanics portion; for the fluid flow part of the code, Newton's iteration is used, which is a fully-implicit method.

The spatial differentiation characteristic of this approach is based on Gauss's divergence theorem or, viewed in a different way, on the integral definition of a partial derivative (Wilkins [128]). This involves approximating the value of any vector gradient, or function, over a discrete portion of the medium by a contour integral over a closed-boundary surrounding the area of interest. This method has an advantage over conventional finite difference schemes based on Taylor series expansions in that it is not restricted

to rectangular grids. Elements of any shape (or number of sides) can be considered and any material property can be assigned to them.

Both, element-centered and node-centered derivatives can be represented through a contour integral along the boundary of the element, or along a prescribed path crossing different elements. This differencing scheme is not the same as the finite volume method [15], or the integral method because the *derivatives* in the differential equations are approximated inside each element or path, not the differential equation itself.

From the point of view of calculating fluid velocities (specific discharge vector) using Darcy's equation, there is no need to approximate the interblock transmissibilities, as in finite volume or conventional finite differences schemes. This is considered naturally by the contour operator which approximates the gradients (see Chapter 2).

This simple differencing method, together with the use of explicit integration in time, was the base of the early Lagrangian 'hydrocodes' developed for computing large deformation dynamic responses of inelastic continua. The development of the 'hydrocodes' started in the 50's and some examples are the codes by Wilkins [128], Maenchen and Sack [68] and Hancock [47], among others.

The scheme of coupling the diffusion and the deformation processes is performed sequentially for each time step: the solid deformation together with the undrained response of the system (changes in pore pressure and

9

saturation due to the solid volumetric strain) are considered during what has been called the 'mechanical' portion of the code. Equilibrium is achieved under these conditions for which a series of pseudo time steps are required. Then the 'fluid' portion of the code is called and the diffusion process takes place in real time. The changes in saturation and pressure that occur will put the system out-of-balance again. Therefore, a new set of mechanical pseudo time steps are needed to equilibrate this new condition, and so on, and so on. This procedure simulates the time scale in which mechanical and diffusion processes take place: though mechanical deformation can be practically instantaneous (order of milliseconds), fluid flow can take days, weeks or even years. Time-dependency in the rock behavior can also be included [25], although this is out of the scope of this dissertation.

Any of the techniques for time discretization commonly used in reservoir engineering, such as IMPES, sequential and implicit methods [5], can be utilized in combination with the spatial approximations particular to this method. In this work, a fully-implicit (unconditionally stable) scheme for the transient flow is implemented.

1.3   Objectives of the research

The goals of this dissertation are the following:

1. Develop a code to model coupled two-phase flow of immiscible fluids in a deformable porous media using the explicit Lagrangian finite-difference

technique with dynamic relaxation.

2. Include a stress-strain rock behavior in which linearly elastic behavior is followed by a linear work-softening branch and by Tresca plasticity.[1]

3. Determine flow, saturation and pore pressure and stress patterns.

4. Use the code to study applied problems such as compaction of a reservoir.

5. Perform parametric studies to test the ability of the model to determine the relevance of the deformation-diffusion (poroelastic) effects.

---

[1]To save repeated complex verbalization, for the rest of the dissertation, this rheology (constitutive condition) will be referred to as "trilinear elasto-plastic" or more simply trilinear behavior. It should be urderstood that this use is only for convenience and in a strict sense, many other rheologies could also be trilinear.

Chapter 2

Literature Review

The literature review primarily describes the characteristics of models that consider coupled multiphase flow in deforming porous media. Finally, some previous codes, based on the Lagrangian finite-diference method with dynamic relaxation, are briefly described.

2.1 Coupled models for multiphase flow in deforming porous media

The first consistent theory formulating the coupled diffusion-deformation processes in fluid filled porous materials, the theory of poroelasticity, was presented by Biot [8], [9], [11], [10]. This theory is an improvement over the early work of Terzaghi [117] who only considered the one-dimensional consolidation of fluid filled soil masses. Over the years, the poroelastic theory has been enriched by several fundamental solutions and reformulations (Rice and Cleary [92], Rudnicki [95],[96], Cheng and Ligget [27], Detournay and Cheng

12

[30], Cleary [21]) that have facilitated a way to sole complex problems.

Another approach to derive a theory for a fluid saturated solid is provided by the so-called *mixture theory*. This theory was introduced in 1960 by Truesdell and Toupin [120]. They use the concepts of superimposed continua and volume fractions, and derive mechanical and thermal field equations for each constituent by allowing mass, momentum and energy interactions. Based on Truesdell's work, Green and Nahgdi [41], Green [42], and Bowen [12] formulate theories for non-linear diffusion of fluid-fluid and fluid-solid mixtures. Prévost [90] provides an extension by considering non-linear anelastic fluid permeated porous media. Zienkiewicz and Shiomi [129] and Meroi et al. [75] present theoretical and computational aspects of large strain static and dynamic saturated and semi-saturated porous media, from the mixture theory point of view, using Biot poroelasticity concepts.

In the opinion of several authors (Derski [29], Ehler and Kubik [35], Zienkiewicz and Shiomi [129], Detournay and Cheng [30]), both lines of derivations lead to essentially equivalent equations. However, the mixture theory is been considered a more systematic approach to the derivation of balance equations of multiphase media models [35]; and, in a way, confirms the correctness of Biot's formulation. Overall, the framework of n-component mixtures, the solid being one of these components, is particularly suitable in applications related to hydrocarbon recovery.

13

2.1.1 Fully-coupled analytical and semi-analytical models

Several authors have analytically studied coupled flow and deformation of the porous medium around boreholes for stability assessment purposes. Most of these studies were single-phase, isothermal, incompressible and steady-state flow developments, limited to hydrostatic in-situ stress field conditions. Paslay and Cheatman [86] study the state of stress around the borehole when inflow exists. Radial changes in permeability are considered, but not plasticity. Rudnicky et al.[95] develope an analytical solution for elasto-plasticity around a borehole considering steady-state flow conditions; permeability is allowed to vary with the radius but symmetry of stresses around the well axis is assumed. These authors show how increasing flow rates increases the extent of the plastic or yield zone around the borehole. They also determine critical flow rates and a stability criterion for an axial-symmetric geometry. Wang and Dusseault [127] present a poro-elastoplastic model considering steady fluid flow for a Mohr-Coulomb strain-weakening material. McLellan and Wang [76] extend this model and study borehole instability problems considering a poro-elastoplastic material (with a Mohr-Coulomb yield criteria) accounting for the effects of changes in steady-state pore pressure near the wellbore in the elastic and plastic zones, internal filtercake and oil-based mud capillary threshold pressure. The effect of the filtercake permeability and its ratio to the formation permability (in the elastic and plastic zones)

14

are assesed. The influence of filtercake thickness and its ability to reduce inflow on plastic yield radius are studied by these authors as well.

The transient in the coupled problem around a borehole is studied by Detournay and Cheng [32] by using the poroelasticity theory for a borehole in a non-hydrostatic stress field. Results show that failure is initiated inside of the medium and not at the borehole wall, and also, that delayed instabilies can occur due to poroelastic effects.

2.1.2 Fully-coupled numerical models

One set of models with a common theoretical basis and formulation is exemplified by the works of Li and Zienkiewicz [66], Li et al. [65], Zienkiewicz and Shiomi [131], Schrefler et al. [97]. The formulation of these models is developed within the framework of continuum theory of mixtures [7], [6], [48], [49], using a spatially-averaged approach. These models take into account rock matrix and fluid compressibility based on Biot's poroelasticity theory. Capillary forces between fluids are considered and Darcy's law for multiphase flow is assumed. Pore pressure is treated either by taking an average over the pore space and weighting it by the saturation of each component; or by considering 'perfect' wettability of the rock so that only one fluid, usually water, is in contact with the rock, so the pore pressure equals the water pressure. The finite element method is used in all these models. Several time integration procedures are used to deal with the transient calculations. These models consider saturated or unsaturated porous media [97], and the

15

dynamics of the porous media [131].

Within this context, Li [67] and Li et al. [65] develope a model for immiscible two-phase flow in a porous medium, which was later generalized to multiphase flow by Li and Zienkiewicz [66]. A generalized Galerkin procedure is followed to discretize the governing equations. For the case of two-phase flow plus deformation of the porous medium, the governing equations are combined such that two nonlinear mass balance equations for the two fluids, and one momentum balance equation (dynamic equation of motion) for the whole mixture are obtained. These equations, together with Darcy's flow equations for each fluid, and the constraint given by the capillary pressure between the fluids complete the system of coupled equations. In this work, two types of solution in the time-domain are presented: an unconditionally stable staggered solution [66], and an unconditionally stable direct integration scheme [132], [133]. The staggered solution is possible only with linear displacement (four node) elements for the fluid and the solid and is more economic computationally. However, with the direct integration solution, diverse solid-fluid element meshes are used successfully. Applications of the codes developed by these authors are limited to very simple examples, so these codes have not been tested in reservoir simulation modelling. Most of the formalism presented in Li et al. [65] for two-phase flow in deforming porous media is followed in this dissertation and is presented in more detail in Chapter 4.

16

Another formalism is that presented by Lewis and Schrefler [61] and followed by others [62], [112]. The main difference from Li et al. [65] stems from the way in which the governing equations are established. In the former case (Li et al.), the theory of mixtures directly led to the expressions of mass balance and momentum for the phases and for the mixture. On the other hand, in the formulation by Lewis and Schrefler [61] the terms contributing to the rate of fluid accumulation were postulated; the inertial terms of the momentum equation are ignored. Also, Darcy's law was assumed valid, but in terms of *absolute* fluid velocity. Contrary to this, Li et al. [65] consider relative fluid velocities with respect to the solid velocity. For subsidence and reservoir production problems, where small rock matrix deformations are expected, the absolute fluid velocity is considered reliable enough [61]. However, whenever the solid grain velocity is expected to be significant in relation to the fluid velocity, the relative velocity of the fluid and the solid matrix should be considered [9]. Such cases could be, for example, dynamic problems, or when plastic or finite deformation is present.

Lewis and Sukirman [62] present a numerical simulation for three-dimensional three-phase flow in a deforming saturated oil reservoir, following Lewis and Schrefler's formulation [61]. Again the finite element method is used, but in this case for an elastic-plastic porous medium, with a Mohr-Coulomb yield surface. The solution of the semi-discretized equations is obtained with a direct solver by assuming small strains. The model by Lewis and Sukirman

[62] is able to capture most of the essence of a conventional black-oil reservoir simulator [5]: it uses typical variables in reservoir engineering, namely, formation volume factors, solution factor for the gas, capillary pressure curves and relative permeabilities and, in addition, the deformation of the porous medium is rigorously taken into account following Biot's poroelasticity theory.

As an application problem, these authors studied a three-phase coning case. Their results indicate a reduction in both GOR (gas-oil ratio) and water cut, for the particular case of the unconsolidated material studied, in comparison with results which do not consider compaction. They also point out that for rocks with higher Young's moduli, the values of reservoir compaction at the top of the reservoir can be assumed to be zero. These results match the expected reservoir engineering performance. This paper, unfortunately, does not address the idea that some areas of the reservoir rock may be subjected to plastic flow. They did not model the situation near the borehole where the most critical conditions in term of stresses and flow are present.

It can be expected that the reservoir rock will present altered patterns of permeability in a plastic zone. Neither was consideration of the variation of permeability due to stress changes included. The authors did not mention the computational requirements nor the CPU time. This is a very important issue if these kinds of models are going to compete with other available

18

reservoir simulators.

Both approaches, Li et al. [66] and Lewis and Schrefler [61], wind up containing similar terms. In fact, comparing results for the problem of a column of soil with two-phase flow indicate excellent agreement between the two approaches [62].

A third group of models is presented by Tortike and Ali [121], [120] for three-dimensional modelling of the flow of water, oil and gas, including steam, with heat flow and simultaneous reservoir deformation. These models were developed to address the problem of thermal recovery (cyclic steaming) of heavy oil in Canadian tar sands. They are based on balance equations for heat and mass transfer and equations for solid mechanical equilibrium. The fluid flow, energy and constitutive equations are coupled through the bulk velocities (relative velocity between solid and fluids). The sand was modelled as an elastic-perfectly plastic material. The assumption of incompressible solid grains (Biot's parameter $\alpha = 1$) was considered, which seems to be justified for the type of unconsolidated sand reservoirs being modelled. As a result, the solid density is considered to be a function of temperature only. Pore pressure was set equal to the water pressure.

The discretization in space was done by the finite element method using Galerkin's weighting techniques. The resulting system of equations is solved in time using the Newton-Raphson iterative technique for the model presented in reference [121]. The authors outline the substantial computational

19

resources required to solve this problem. Several other papers published in the same line of research, trying different numerical approaches, are presented by Aktan and Ali [2], Ali and Blunschi [3].

2.2 Codes based on the explicit finite difference technique with dynamic relaxation

The solid mechanics portion of the explicit finite difference code presented in this dissertation is based on codes presented by Silling [105], and Cundall [25]. The same type of spatial differencing scheme based on the Gauss divergence theorem and explicit integration of the motion equation with dynamic relaxation used in these codes is followed here.

Silling [105] studied large deformations of both compressible and incompressible elastic bodies, using the general theory of finite elasticity [43]. His code (CHIMP) is a purely solid mechanics code, oriented to study localization and phase changes in the governing equations of elastic solids. This code is set up with a total Lagrangian formulation, in terms of the Piola, or nominal stress tensor field [70]. Deformation gradients are used as measures of the solid strain. Elements used are quadrilaterals. The type of damping used in the motion equation is velocity proportional. There is an additional velocity term introduced in the motion equation together with a factor β, used to provide critical damping for the system. The critical damping is obtained by estimating the fundamental frequency of the grid, considering the

20

approximate transit time for infinitesimal waves through the entire width of the mesh, e.g. $\beta = \pi \bar{c}/2L$, where $\bar{c}$ is the area-average wave speed in the mesh and L is a characteristic length. In cases in which damping in the system does not respond to this approximation, a refined estimate of the dynamic relaxation parameters is used, based on an algorithm presented by Papadrakakis [83], which can automatically adjust the damping. Hourglassing is controlled by using small resistive forces from an algorithm similar to the one presented by Hancock [47], although in CHIMP the algorithm is based on displacements rather than velocity.

Silling [105] adapts the explicit finite difference method with the inclusion of finite deformations in a theoretical study of the conditions prevailing around a fracture, or crack, in a plastically deforming material [105]. The equations describing this problem are elliptic if material behavior is linear elastic and change to parabolic or hyperbolic when yielding occurs. Other applications include the propagation of shear bands in a soil block under compression, and necking in elastic bars [102].

A very interesting application of Silling's plane strain code is the one provided by Burridge [14] for slope stability analyses of soils in small scale centrifuge experiments. Burridge is able to track slip surfaces in the slopes without inducing any artificially weak element in the mesh. A trilinear material behavior was considered, including the increase of the stiffness of the soil with confining pressure, and, hence, depth for a slope under gravitational

21

loading.

In the two-dimensional version of Cundall's [25] code (FLAC), elements used are quadrilaterals but they are internally subdivided into triangles in order to avoid hourglass problems [1]. The mixed discretization procedure [69] permits accurate modeling of plastic behavior without the typical 'mesh-locking' problem [77]. The damping procedure is not velocity proportional but, rather, proportional to the magnitude of the *out-of-balance force* at each node. The damping force direction is such that energy is always dissipated. This is an enhancement over the velocity proportional damping used in Silling's codes which introduces body forces that can overshadow the failure process.

---

[1]This topic will be addressed further in chapter 3

22

Chapter 3

Explicit Lagrangian Finite Difference Technique

3.1 Introduction

The solution of an initial/boundary value problem, under continuum mechanics hypotheses, includes the formulation of conservation equations. In addition, constitutive equations are needed to define a particular material behavior that is being considered. To complete the set of equations, it is also necessary to define the geometry of the problem, as well as the boundary conditions. This set of laws and conditions together, referred to as governing equations, might be very difficult to solve analytically. Therefore, numerical techniques are usually used to obtain approximate answers to problems with complicated initial and boundary conditions.

One of the oldest, and more widely used, numerical tecniques to solve initial/boundary value problems is the finite difference technique [52]. The governing equations include derivatives which are approximated by algebraic

23

expressions involving field variables, like displacements or stresses, defined at the grid points or at the blocks, in which the medium is discretized.

Several types of finite-difference representations can be used to solve a partial differential equation in a given domain. Taylor series, polynomial fitting and finite volume methods are commonly used. In this dissertation, the derivation of the finite difference scheme is based on an integral approach using the Gauss divergence theorem. This scheme was introduced by Wilkins [128] for solid mechanics problems and has been given the name of *contour finite-difference operator* [58]. It is described in Section 3.3.

The purpose of this chapter is to provide a background to the explicit finite-difference technique combined with the dynamic relaxation procedure. Only the solid mechanics aspects are included in this chapter; the fluid flow part is addressed in Chapter 5.

3.2 Formulation of the initial/boundary value problem

Continuum mechanics theory is followed when formulating the problem of two-phase flow in a deforming porous medium. The concept of a representative elementary volume is considered to be valid together with mixture theory of superimposed continua; the influence of pre-existing discontinuities in the rock mass is neglected.

24

3.2.1 Equations of motion and equilibrium

One fundamental law that must be satisfied is the principle of linear momentum. The equations of motion, which result from this principle, can be expressed in global form as:

$$\int_S \sigma \mathbf{n} dS + \int_V \rho \mathbf{b} dV = \int_V \rho \mathbf{a} dV, \qquad (3.1)$$

where S is an arbitrary closed surface in the body, V its volume, $\rho \mathbf{b}$ is the body-force density field, $\mathbf{n}$ is an outward-directed unit vector normal to S, ρ is the mass density field, $\mathbf{a}$ is the acceleration, and σ represents the stress tensor. If σ_{ij} is differentiable at any point x, the equation of motion holds locally, resulting in:

$$\nabla \cdot \sigma(\mathbf{x}, t) + \rho \mathbf{b}(\mathbf{x}, t) = \rho \mathbf{a}(\mathbf{x}, t) \qquad (3.2)$$

For the equilibrium of the body, all involved forces will balance. This condition is expressed as:

$$\sigma_{ji,j} + \rho b_i = 0, \qquad (3.3)$$

which is the equilibrium equation for the body.

3.2.2 Constitutive equations

Response of a rock to applied boundary conditions depends upon its rheological properties. In continuous models, these rheological properties are represented by constitutive equations which relate strains and stresses. A

25

constitutive equation is established through experimental testing under particular assumptions [1]. In general, it can be formulated as:

$$\dot{\bar{\sigma}}_{ij} = F(\dot{\sigma}_{ij}, \dot{e}_{ij}, \cdots) \tag{3.4}$$

where F is the functional form of the constitutive equation, $\dot{e}_{ij}$ is the strain rate tensor, and $\dot{\bar{\sigma}}_{ij}$ is the co-rotational stress rate tensor (both defined below).

3.2.3 Strain rate and co-rotational stress rate tensors

The deformation of the region is traced by following the motion of the grid points through a sequence of small time steps, Δt. The coordinates at the initial (fixed) reference configuration are described by the coordinate vector $\mathbf{X}$. The configuration at time t (current) is described by $\mathbf{x}(\mathbf{X}, t)$.

The kinematic relationship between velocities, $\dot{u}_i$, and strains, e_{ij}, is established through the definition of the strain rate tensor, which is:

$$\dot{e}_{ij} = \frac{1}{2}(\dot{u}_{i,j} + \dot{u}_{j,i}) \tag{3.5}$$

where strains are infinitesimal.

The differentiation is performed with respect to the reference configuration, i.e., the underlying spatial coordinates in Equation 3.5 are those of the reference configuration.

---

[1] For linear isotropic elasticity, only E and ν are required; these are determined through a triaxial test under appropriate conditions. More complicated constitutive laws require more parameters and a number of different tests.

The co-rotational stress rate tensor is defined as:

$$\overset{\circ}{\sigma}_{ij} = \frac{D\sigma_{ij}}{Dt} - w_{ik}\sigma_{kj} + \sigma_{ik}w_{kj} \qquad (3.6)$$

where $\frac{D}{Dt}$ is the material derivative, and w_{ij} is the rotation tensor, which is defined as:

$$w_{ij} = \frac{1}{2}(\dot{u}_{i,j} - \dot{u}_{j,i}) \qquad (3.7)$$

For a Lagrangian formulation, the frame of reference is attached to the solid particles; therefore, the convective terms of the material derivates disappear.

3.2.4   Small and large deformation calculations

For a small strain assumption, the initial (fixed) configuration is taken as the reference configuration. Neither the correction for rotations of the body nor the update of the coordinates are needed. For large strain calculations, however, the reference state is replaced by the instantaneous current position x at each time step (updated Lagrangian version) [70]. The coordinates are also up-dated to the new position after each time step. In this manner, large strains and geometrical non-linearities can be included with very little computational effort.

When large deformation calculations are made, the grid will actually deform following the displacements of the corresponding physical material, as opposed to the Eulerian formulation in which the change of the quantities is measured with reference to a fixed mesh.

27

3.2.5 Initial and boundary conditions

An initial state of stress has to be prescribed prior to initiation of the disturbance at the domain. The boundary conditions may be in the form of tractions or velocity restrictions. The traction vector, t_i, on a surface with unit normal, n, is given by Cauchy's theorem [71] as:

$$t_i = \sigma_{ij} n_j \tag{3.8}$$

The velocity at a boundary may be zero in any of the coordinate directions, or it may have a definite non-zero value, i.e. compression at a given rate of a side of a block. Mixed boundary conditions, such as velocity constraints in one direction and traction in another direction may be assigned. Contact or frictional boundary conditions are not considered for the particular applications in this dissertation, but can be incorporated [51].

3.3 Numerical representation of spatial derivatives

Wilkins [128] developed a differencing scheme based on the integral definition of a partial derivative:

$$\frac{\partial F}{\partial x_i} = \lim_{A \to 0} \left(\frac{1}{A} \int_S F n_i dS \right) \tag{3.9}$$

where F is a scalar, vector or tensorial quantity, x_i is a component of the position vector, A is the area of integration, dS is the incremental arc, and

28
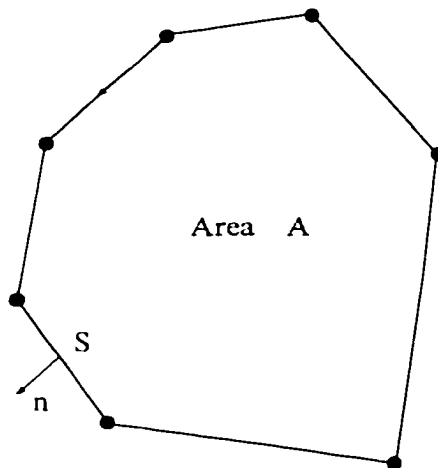
Figure 3.1: Integration path for the contour differencing scheme

n_i is the component of the unit outward normal to dS. If the integration is done over a path defined by a polygon of a given number of sides M (Figure 3.1), an approximate expression can replace Equation 3.9,

$$\frac{\partial F}{\partial x_i} \simeq \frac{1}{A} \sum_{N=1}^{M} F^{(N)} n_i S \qquad (3.10)$$

where $F^{(N)}$ is the average value of F on the side, S is the side length, and n_i is the outward pointing component of the normal unit vector to S.

The same result can be obtained using the Gauss divergence theorem to express the derivative of a function, vector or tensor in a discrete area of the body in terms of an integral around the boundary limiting this area. Consider for example, a vector field $\mathbf{f}$, in two dimensions, with continuous

29

first-order derivatives in a region of area A, bounded by a curve L. By Gauss divergence theorem:

$$\int_A \nabla \mathbf{f} dA = \int_L \mathbf{f} \cdot \mathbf{n} dL \tag{3.11}$$

in which $\mathbf{n}$ is the outward normal to the curve, and dA and dL are elements of area and arc of length, respectively.

If the derivative is assumed to be constant over the area, or by taking the average value of the derivative as $< f_{i,j} >$, then:

$$< f_{i,j} > = \frac{1}{A} \int_A f_{i,j} dA. \tag{3.12}$$

Dividing Equation 3.11 by A and comparing with Equation 3.12 gives:

$$< f_{i,j} > = \frac{1}{A} \int_L < f_i > n_j dL \tag{3.13}$$

The finite difference form of Equation 3.13 is obtained by replacing the integral by a sum over the M sides of the zone,

$$< f_{i,j} > = \frac{1}{A} \sum_{N=1}^{M} < f_i >^N n_j^N L^N, \tag{3.14}$$

where L is the length of the Nth side of the triangle, n_j is the component in the jth-direction of the outward normal vector to the side, and $< f_i >$ is the average value of f_i over the side. Hereafter, this operator will be called the *contour difference operator* [58]. If the function varies linearly between the nodes, this expression is exact. Note that by using this approximation, it is assumed that the gradient of the vector f is constant (equal to the average value of the gradient) within the area of integration.

30

For a quadrilateral element, Equation 3.14 can also be obtained by expanding into Taylor series about the center of a zone from the corner points, as was shown by Herrmann and Bertholf [51].

The code developed for this dissertation was built considering the region of interest to be portioned into quadrilateral elements as represented in Figure 3.2(a). Each of these elements is subdivided internally into two sets of overlapping triangular sub-elements, Figure 3.2(b). The gridpoints at the corners of the quadrilaterals connect the elements to each other   Certain quantities are associated with nodes while others are associated with elements (or sub-elements). Node-centered variables are position, velocity, acceleration, stress gradient (forces), body force and damping force. Zone-centered variables include stress tensor components, strain rate tensor components and mass density. Note that, in general, vectors are associated with nodes and tensors with elements. Quantities such as pressure and saturation, to be used in the two-phase flow calculations, are assigned to elements because flow equations are solved for the elements.

For a generic quadrilateral, consider one of the overlapping triangles, (Figure 3.3). The value of the function at the nodes is known and is denoted by f_i^l; where $l = 1, 2, 3, 4$ corresponds to the local numbering of the nodes forming a quadrilateral. Also, the geometrical parameters such as length of each side segment (ΔS) are known quantities. By Equation 3.14 the x-

31
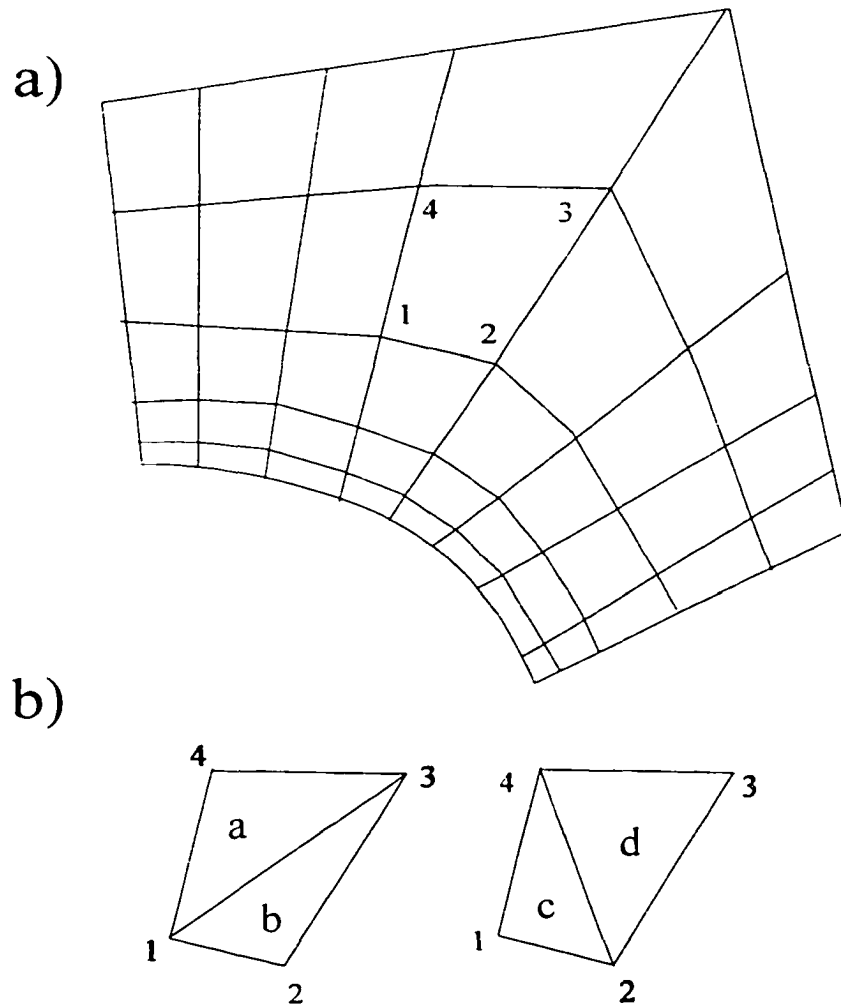
Figure 3.2: Discretization of the medium: a) typical mesh with quadrilateral elements; b) internal sub-discretization in overlaying triangles
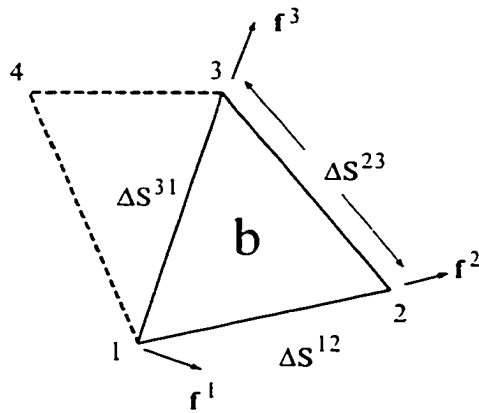
Figure 3.3: Generic quadrilateral with the triangle subdivision showing values of the function f at the nodes

component of the gradient is:

$$f_{i,x} = \frac{1}{A}\left[< f_i^{\overline{12}} > (n_x\Delta S)^{\overline{12}} + < f^{\overline{23}} > (n_x\Delta S)^{\overline{23}} + < f^{\overline{31}} > (n_x\Delta S)^{\overline{31}} \right]$$

(3.15)

where $< f_i^{\overline{12}} >$ is the average value of f_i over the side segment $\overline{12}$ of the triangle, which by assuming a linear variation of f_i over the side can be taken as:

$$< f_i^{\overline{12}} > = \frac{f_i^1 + f_i^2}{2}.$$

(3.16)

The same applies to all segments. Similarly, the y-component is given by:

$$f_{i,y} = \frac{1}{A}\left[<f_i^{\overline{12}}> (n_y\Delta S)^{\overline{12}} + <f_i^{\overline{23}}> (n_y\Delta S)^{\overline{23}} + <f_i^{\overline{31}}> (n_y\Delta S)^{\overline{31}} \right].$$

$$(3.17)$$

The components n_x and n_y of the normal unit vector to the sides of the triangle are:

$$n_x^{\overline{12}} = \frac{y^{(2)} - y^{(1)}}{\Delta S^{\overline{12}}}; \quad n_y^{\overline{12}} = \frac{x^{(1)} - x^{(2)}}{\Delta S^{\overline{12}}}$$

$$n_x^{\overline{23}} = \frac{y^{(3)} - y^{(2)}}{\Delta S^{\overline{23}}}; \quad n_y^{\overline{23}} = \frac{x^{(2)} - x^{(3)}}{\Delta S^{\overline{23}}}$$

$$n_x^{\overline{31}} = \frac{y^{(1)} - y^{(3)}}{\Delta S^{\overline{31}}}; \quad n_y^{\overline{31}} = \frac{x^{(3)} - x^{(1)}}{\Delta S^{\overline{31}}} \qquad (3.18)$$

Substituting Equations 3.16 and 3.18 into Equation 3.15 gives:

$$f_{i,x} = \frac{1}{A}\left[\frac{(f_i^{(1)} + f_i^{(2)})}{2}(y^{(2)} - y^{(1)}) + \frac{(f_i^{(2)} + f_i^{(3)})}{2}(y^{(3)} - y^{(2)}) + \frac{(f_i^{(1)} + f_i^{(3)})}{2}(y^{(3)} - y^{(1)}) \right].$$

$$(3.19)$$

Expanding and cancelling terms gives the gradient of f_i in x-direction as:

$$f_{i,x} = \frac{1}{2A}\left[f_i^{(1)}(y^{(2)} - y^{(3)}) + f_i^{(2)}(y^{(3)} - y^{(1)}) + f_i^{(3)}(y^{(1)} - y^{(2)}) \right]. \qquad (3.20)$$

The corresponding equation in $y-$direction is:

$$f_{i,y} = -\frac{1}{2A}\left[f_i^{(1)}(x^{(2)} - x^{(3)}) + f_i^{(2)}(x^{(3)} - x^{(1)}) + f_i^{(3)}(x^{(1)} - x^{(2)}) \right]. \qquad (3.21)$$

The contour difference operator can also be used to approximate gradients at the nodes. For an integration path, such as the one shown in Figure 3.4, the contour differencing operator, given by Equation 3.14, is applied to the quadrilateral $ABCD$ to give the following expressions:

$$\left(\frac{\partial f_i}{\partial x}\right)_O = \frac{1}{2A}\left[f_i^{(1)}(y^{(A)} - y^{(D)}) + f_i^{(2)}(y^{(B)} - y^{(A)}) \right.$$

34
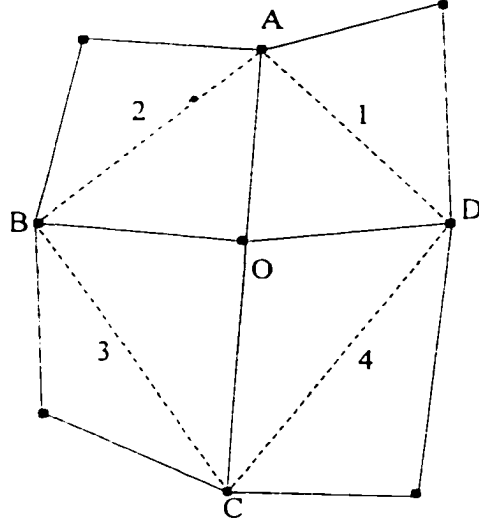
Figure 3.4: Gradient of f_i evaluated at the gridpoint O

$$+ f_i^{(3)}(y^{(C)} - y^{(B)}) + f_i^{(4)}(y^{(D)} - y^{(C)}) \right] \tag{3.22}$$

$$\left(\frac{\partial f_i}{\partial y} \right)_O = -\frac{1}{2A} \left[f_i^{(1)}(x^{(A)} - x^{(D)}) + f_i^{(2)}(x^{(B)} - x^{(A)}) \right.$$

$$\left. + f_i^{(3)}(x^{(C)} - x^{(B)}) + f_i^{(4)}(x^{(D)} - x^{(C)}) \right] \tag{3.23}$$

where A is one-half the area of the quadrilateral $ABCD$:

$$A = \frac{1}{4} \left[(y^{(B)} - y^{(D)})(x^{(A)} - x^{(C)}) - (x^{(B)} - x^{(D)})(y^{(A)} - y^{(C)}) \right] \tag{3.24}$$

The integration path now crosses through different elements. Therefore, the conditions of continuity of the first-order derivative required by the Gauss divergence theorem may not be met because different quadrilaterals with different properties are enclosed in the integration path.

The contour difference operator, given by Equation 3.14, is used to determine stress gradients and velocity gradients in the mechanical portion of the code. It is also used in the fluid flow portion to determine pressure, saturation and velocity gradients, respectively.

Unlike traditional finite difference schemes, the contour difference operator is not restricted to rectangular grids. Indeed, the enclosed region may have any number of sides, and/or material properties. Therefore, complex geometries and boundary conditions can be handled. The extrapolation to three-dimensional schemes is straightforward by using Gauss theorem, Equation 3.11 for a volume enclosed by a two-dimensional surface area [58], [25].

3.4 Hourglassing modes

The drawback of using simple, constant strain quadrilaterals is the presence of mesh instabilities commonly referred to as *hourglassing, zero-energy* or *kinematic* modes [59]. For polygons with more than three nodes, there are combinations of nodal displacements which do not produce any strain and, therefore, no opposing forces are created. The resulting effects are displacements in alternating directions (Figure 3.5).

These effects are result from over-determining the difference equations [59]. In other words, there are eight independent components of velocity per zone (two at each gridpoint) while only six modes are used to define the deformation per zone (three components of uniform strain plus three rigid

36
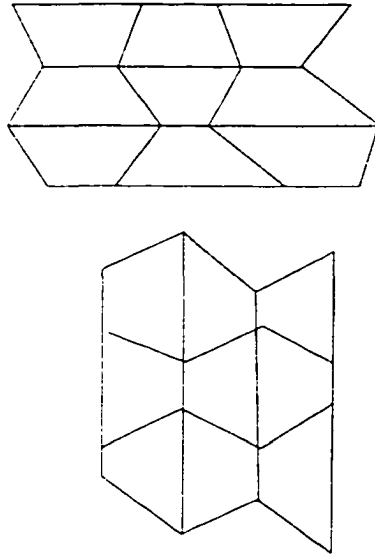
Figure 3.5: Typical hourglass mode of deformation in a quadrilateral mesh.

body motions). Hence, there are two undefined modes of deformation which compose the hourglass. Several procedures have been used to overcome the hourglass modes (Hancock [47], Silling [104], Herrmann and Bertholf [51]). One viable, and simple, solution is the use of constant strain triangles, which do not result in over-determinaning the difference equations [69]. However, this can lead to an unreallistically stiff response of the model, referred to as *mesh-locking* (Nagtegaal et al. [77]). To solve this problem, a mixed discretization procedure [69] was is (see Section 3.7).

3.5   Basic calculation cycle

The basic calculation cycle is summarized in what follows. At each time step, and for each grid point in the mesh, the net nodal forces are computed as the stress gradients at the zones, plus the gravity and boundary forces. These forces are not in balance (equilibrium has not been addressed yet). Therefore, accelerations are produced according to the equation of motion , Equation 3.2.

Integration of this equation in time allows the corresponding velocities, $\dot{u}_i$, and displacements, u_i, to be determined for the grid points. Velocities are measured in length over each time step. This equation also includes a damping term which will be introduced in Section 3.12.

Boundary conditions are now placed on the velocities. The strain rates, $\dot{e}_{ij}$, are computed for each zone from the velocity gradients. Thereafter, the stress increments are determined by invoking the constitutive equation for each zone.

Continuing with the calculation cycle, stress boundary conditions are applied. Again the forces are calculated and if the body is not in equilibrium, it will accelerate. The corresponding velocities and displacements are once again calculated. The cycle is repeated until the out-of-balance forces are very small and tend to zero, indicating that equilibrium or steady-state conditions have been reached.

Since this is an explicit method, the unknowns are determined using

38

known values from the previous pseudo time steps at the local point or at immediate neighboring points. These known variables remain fixed within each computation step. It is assumed that the newly-obtained velocities do not affect the stress rates during a particular time step. This is justified only if a sufficiently small time step is chosen such that, in fact, the information does not propagate beyond the element. This critical time step is associated with the speed at which the information is able to propagate in the medium. If the time step is smaller than this speed, the explicit procedure will be correct because no information beyond the immediate surroundings of a node can affect its behavior. As computation progresses, disturbances will propagate over several elements to achieve balance of forces throughout the body (the actual determination of the critical time step is discussed in Section 3.13).

3.6 Strain rates

The strain rate for each sub-element, defined by Equation 3.5, is determined through the velocity gradients which in turn are calculated using the contour difference operator, Equation 3.14. For a triangular sub-element, the velocity gradient components in the x-direction are, from Equations 3.20 and 3.21:

$$\dot{u}_{i,x} = \frac{1}{2A}\left[(\dot{u}_i^{(1)}(y^{(2)} - y^{(3)}) + \dot{u}_i^{(2)}(y^{(3)} - y^{(1)}) + +\dot{u}_i^{(3)}(y^{(1)} - y^{(2)})\right]; \quad (3.25)$$

39

where $(1), (2)$ and (3) are referred to nodes defining the particular triangle. The equivalent expression for the $y-$component of the velocity gradient is:

$$\dot{u}_{i,y} = -\frac{1}{2A}\left[(\dot{u}_i^{(1)}(x^{(2)} - x^{(3)}) + \dot{u}_i^{(2)}(x^{(3)} - x^{(1)}) + +\dot{u}_i^{(3)}(x^{(1)} - x^{(2)})\right]. \quad (3.26)$$

3.7   Mixed discretization

As previously stated, in finite element and finite difference codes for solid mechanics, the use of constant strain triangles leads to an over-stiff response or *mesh-locking* (Nagtegaal et al. [77]). The excessive stiffness of these elements has been attributed to over-constraining the volumetric response. Marti and Cundall [69] propose the mixed discretization procedure to remove mesh-locking while maintaining the use of very simple elements, such as constant strain triangles. In this technique, each quadrilateral is subdivided into two superposed sets of triangles by two diagonals (Figure 3.2). The volumetric (mean or isotropic) stress and strain rate components are taken to be constant over the whole quadrilateral element, while the deviatoric components are treated separately for each triangular sub-element. Hence, the volumetric strain rate is averaged over each set of triangles while the deviatoric part remains unchanged.

The volumetric strain rate, $\dot{e}_m$, for the first set of triangles (a, b) in Figure 3.2 is:

$$\dot{e}_m = \frac{\dot{e}_{11}^a + \dot{e}_{22}^a + \dot{e}_{11}^b + \dot{e}_{22}^b}{2}, \quad (3.27)$$

40

while the deviatoric strain for each triangle is:

$$\dot{e}_d^a = \dot{e}_{11}^a - \dot{e}_{22}^a$$

$$\dot{e}_d^b = \dot{e}_{11}^a - \dot{e}_{22}^b. \tag{3.28}$$

The normal strains for each triangle are, therefore:

$$\dot{e}_{11}^a = \frac{\dot{e}_m + \dot{e}_d^a}{2}$$

$$\dot{e}_{11}^b = \frac{\dot{e}_m + \dot{e}_d^b}{2} \tag{3.29}$$

$$\dot{e}_{22}^a = \frac{\dot{e}_m - \dot{e}_d^a}{2}$$

$$\dot{e}_{22}^b = \frac{\dot{e}_m - \dot{e}_d^b}{2}$$

A similar procedure is followed for the second set of triangles.

3.8 Constitutive equations

Because of the sequence of calculations, the constitutive relationship is set in a strain-space model in which stresses are computed from strains. Contrary to this, in the stress-space model of a constitutive equation, strains are computed from stresses (usually an incremental approach is required to consider nonlinearities [78]). In the program developed for this dissertation, once the strain rate tensor has been calculated for each triangular subzone, any constitutive equation can be invoked to determine the stress changes within this subzone. Actually, several subroutines containing different constitutive equations can be prepared and assigned to different regions of the

41

domain when modelling heterogeneous materials. Linear elastic and trilinear constitutive equations have been included in the present code.

3.8.1 Linear elastic and trilinear stress-strain relation

The stress-strain constitutive relation, in incremental form, for a linear elastic material is given by:

$$\Delta \sigma_{ij} = \left[\delta_{ij} \left(K - \frac{2}{3} G \right) \dot{e}_{kk} + 2G \dot{e}_{ij} \right] \Delta t \tag{3.30}$$

where δ_{ij} is the Kronecker delta, Δt is the time step, and G and K are the shear and bulk moduli, respectively.

The trilinear constitutive equation is a very simple stress-strain relationship given by three linear segments [102],A,B, and C, as shown in Figure 3.6(a). This constitutive equation is presented in terms of the radius of Mohr's strain circle, ϵ_m, and the radius of the Mohr's stress circle, τ_m, Figure 3.6b. The parameters ϵ_{m1}, ϵ_{m2} and τ_r are specified rock values which determine the peak and the residual strength of the rock. The first segment A of the trilinear is the same as the linear elastic stress-strain relation. The parameter ϵ_m is defined as:

$$\epsilon_m = \sqrt{e_{12}^2 + (e_{11} - \frac{e}{2})^2} \tag{3.31}$$

where e is volumetric strain ($e = \theta = e_{11} + e_{22}$) and e_{11}, e_{12}, e_{22} are components of the strain tensor.

The use of the constitutive equation is shown in Figure 3.6a with dotted lines. The known strain is given as an input and the corresponding shear

42
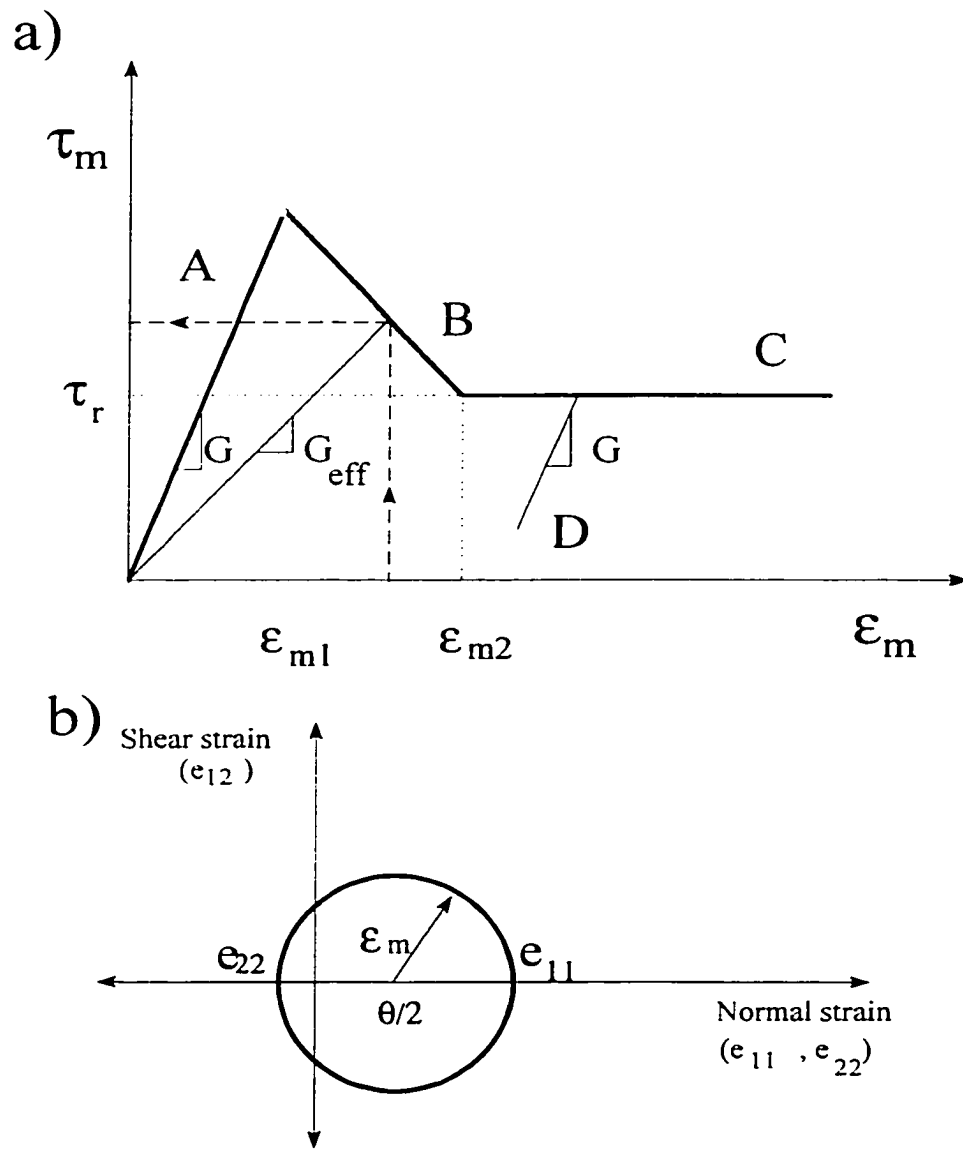
Figure 3.6: a) Trilinear constitutive relation; b) Mohr's circle of strain

stress is defined by the curve from which is possible to determine the effective parameter G_{eff} as:

$$G_{eff} = \frac{\tau_m}{\epsilon_m}. \tag{3.32}$$

In other words, ϵ_m is computed from strains, entering the curve will determine G_{eff} and then the stress increments are thus computed using Equation 3.30 applying the effectuve parameter. Note that for the first segment (A), G is constant, but after the level of strain exceeds ϵ_{m1}, the effective shear modulus decreases continuously. When ϵ_{m2} is exceeded, the shear modulus is further degraded at a higher rate to maintain the stress at a constant residual strength.

The unloading behavior is considered through segment D (Figure 3.6a) using the slope of segment A. Unloading is applied when the ϵ_m is lower than the maximum experienced by a particular element in its loading history. Reloading follows the same path until this maximum is reached, and the corresponding segment of the constitutive curve is resumed.

3.9 Stress and displacement boundary conditions

Boundary conditions involve the application of external tractions and/or velocities. To apply velocity boundary conditions, velocities specified at the boundary are used directly, instead of calculating them through the momentum equation. When velocities other than zero are prescribed, care must be

44

taken to apply such boundary conditions in an incremental way. The rate
at which the velocity boundary condition is applied depends on information
propagation speed through the mesh. [2] Silling [104] and Herrmann and
Bertholf [51] present a thorough explanation on the application of this type
of boundary conditions, as well as contact boundary conditions, and others.

This code is designed to accept stresses at the boundaries from which
the corresponding traction forces at the boundary nodes are calculated, as
explained in Section 3.10.1.

3.10   Nodal forces

If the mass distributed over the area of a zone is lumped at the corner nodes,
the motion equations can be written in terms of nodal masses, accelerations
and forces at the nodes as:

$$F_i^{internal} + F_i^{body} + F_i^{bdry} = ma_i \qquad (3.33)$$

where $F_i^{internal}$ is the force on the ith node due to the internal stress gradients,
F_i^{body} is the body force lumped at the node, and the force at a boundary node
is F_i^{bdry}; a_i is the acceleration and m is the mass lumped at the nodes (see
Section 3.13).

Therefore, the total nodal force is the sum of the boundary forces, the
gravitational and the internal forces.

---

[2]This will not be discussed further since no such boundary condition will be considered
in this dissertation.

3.10.1 Boundary forces

The nodal forces acting on the boundaries are calculated from the stresses prescribed at the boundaries by:

$$F_i^{bdry} = \sigma_{ij}^{bdry} n_j \Delta s \qquad (3.34)$$

where n_j is the outward normal unit vector of the boundary segment, and Δs is the length of the segment over which the stress σ_{ij}^{bdry} is applied. Half of this force is assigned to each node of the corresponding boundary segment.

3.10.2 Gravity forces

The gravity forces F_i^g are computed from:

$$F_i^g = g_i m_g \qquad (3.35)$$

where m_g is the lumped gravitational mass at the node. This is defined as one third of the mass of any triangle connected to a node. Since a double set of overlapped triangles is considered, the resulting quantity must be divided by two. Therefore,

$$m_g = \frac{1}{2} \sum \frac{\rho A}{3} \qquad (3.36)$$

3.10.3 Internal forces

The equivalent forces applied to grid points are determined from the stresses prevailing in the surrounding zones. For a particular subzone, the gradient of stress times the area $(A\sigma_{ij,j})$ may be interpreted as the force on a node due

46
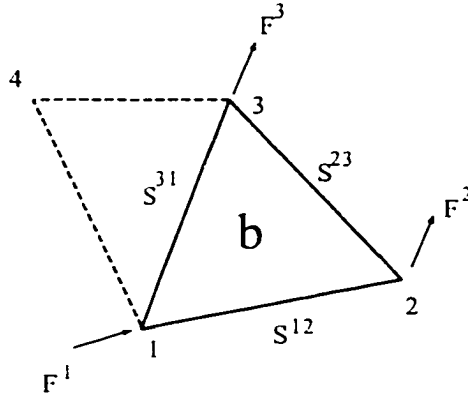
Figure 3.7: Generic triangle showing nodal forces

to *internal* stresses. Actually, the stresses at each subzone act as tractions on its sides. Then, the traction acting over each segment of the triangle is substituted for by two equal forces (distributed half-and-half) located at its extremes. Each triangle corner receives forces from two adjoining segments (Figure 3.7). For a generic grid point 1, belonging to a triangle in the mesh , the following expression is obtained:

$$F_i^{(1)} = A(\sigma_{ij,j}^{\overline{12}} + \sigma_{ji,j}^{\overline{31}})$$

or, in terms of the contour operator:

$$F_i^1 = \frac{1}{2}\sigma_{ij}(n_j^{\overline{12}}S^{\overline{12}} + n_j^{\overline{31}}S^{\overline{31}}) \tag{3.37}$$

47

The components of the unit normal vector are given by Equations 3.18. After simplification, the following expressions result for node 1 in the triangle sketched in Figure 3.7 (nodes 1, 2 and 3 are any consecutive nodes in a counterclockwise sense).

$$
\begin{aligned}
F_x^{(1)} &= \frac{1}{2}\left[\sigma_{xx}\left(y^{(3)} - y^{(2)}\right) - \sigma_{xy}\left(x^{(3)} - x^{(2)}\right)\right] \\
F_y^{(1)} &= \frac{1}{2}\left[\sigma_{xy}\left(y^{(3)} - y^{(2)}\right) - \sigma_{yy}\left(x^{(3)} - x^{(2)}\right)\right]
\end{aligned}
\tag{3.38}
$$

Similar expressions can be written for the rest of the nodes of the sub-element.

The nodal forces are calculated for the grid points corresponding to the four triangles (two sets) forming the quadrilateral. Within each set, the forces from triangles meeting at each node are summed. For example, in the set of triangles $a - b$ (Figure 3.2b), the forces at node 1 from triangles a and b are summed. The same holds for node 3. However, for node 2, only the corresponding force for triangle b is considered; similarly, for node 4, only triangle a contributes. The same procedure is followed for triangles $c - d$. Next, at each grid point, the nodal forces resulting from both sets are averaged, to give four nodal force vectors which are the contribution of a particular quadrilateral in the mesh.

The net internal nodal force vector associated with a grid point, $\sum f_i$, is then obtained by summing the corresponding nodal forces from all quadrilaterals meeting at the grid point.

Applied boundary loads, where pertinent, and gravitational forces are added to the net internal nodal force vector at this stage, to obtain the total

48

nodal force vector, defined in Equation 3.33, for each grid point of the mesh.

3.11   Integration of the motion equation

By using the contour operators in the calculation of stress gradients, the integration of the motion equation is done in its global (integral) form, Equation 3.1, rather than in a local form, Equation 3.2. Therefore, discontinuities in the stress field are allowed without convergence problems.

While the forces are not in equilibrium in the body, the nodes will accelerate following the equation of motion. The velocities can be calculated by integrating this equation in time. If centered finite difference equations are used for the velocity, the scheme will be second-order accurate in time [4]. Hence,

$$\dot{u}_i^{(n+\Delta n/2)} = \dot{u}_i^{(n-\Delta n/2)} + \left(\sum f_i^{(n)} + \beta \right) \frac{\Delta t}{m} \tag{3.39}$$

where β is a damping term (discussed further in the next section). For the first time step, the velocities at the time $(n - \Delta n/2)$ are equal to those at time n.

Displacements are calculated for the time n as:

$$u_i^n = \frac{(\dot{u}_i^{n+\frac{\Delta n}{2}} + \dot{u}_i^{n-\frac{\Delta n}{2}})}{2} \Delta t, \tag{3.40}$$

so there is a half time step shift between velocities and displacements.

49

3.12 Dynamic relaxation and damping

The code developed here uses the dynamic relaxation procedure introduced by Day [28] and Otter and Cassell [81]. Dynamic relaxation consists of the modelling of an equilibrium boundary-value problem by using the dynamic equations of motion and by using an artificial damping to reduce the large-time limit of the dynamic problem. The dynamic equations of motion are used even though static solutions are pursued. However, an artificial damping term is included such that, for long terms, a steady-state condition or a static equilibrium is obtained. A complete discussion of this method is presented by Underwood [123].

The dynamic relaxation method, together with an explicit finite difference formulation, are especially well-suited for problems involving complex systems, e.g. nonlinear, finite strain, physical instability. On the other hand, it is not efficient for modeling linear, small-strain problems [25].

The artificial damping used in most dynamic relaxation methods is velocity proportional. That is, the magnitude of the damping force is proportional to the velocity of the nodes. Cundall [25] points out that a velocity proportional damping introduces body forces, which can overshadow the failure process. Also, it is difficult to determine the optimum or critical parameter to provide damping of the system. An adaptive damping is needed according to differences in behavior in different regions of the medium. In this dissertation, the damping scheme proposed by Cundall [25] is used where

50

the damping scheme is proportional to the magnitude of the out-of-balance force at each node. The direction of the damping force is such that energy is always dissipated. The expression for the integrated motion equation with the adaptive damping is given by:

$$\dot{u}_i^{(t+\Delta t)} = \dot{u}_i^{(t-\Delta t)} + \left[\sum F_i^{(t)} - \alpha | \sum F_i^{(t)} | \text{ sgn}(\dot{u}_i^{(t-\Delta t)}) \right] \frac{\Delta t}{m_n} \qquad (3.41)$$

where α is a safety factor, set to 0.8 in the program, and m_n is a ficticious nodal mass which is derived in Section 3.13.

The time (or pseudo-time) involved in the procedure is a fictitiuos quantity and is intended to let the system achieve static equilibrium.

3.13   Critical time step and density scaling

The explicit time integration scheme is conditionally stable. The stable time step is limited by the spatial mesh size, and also depends upon the constitutive equations. The stability condition for an elastic solid, discretized into elements of size Δx, is given by the Courant condition [4]; i.e.,

$$\Delta t < \frac{\Delta x}{C} \qquad (3.42)$$

where C is the maximum speed at which information can propagate. Typically, the P-wave or dilatational wave speed, C_p, is the fastest wave. The speed for dilatational waves in the x_1-direction is:

$$C_p^2 = \frac{1}{\rho} \frac{\partial \sigma_{11}}{\partial e_{11}} \qquad (3.43)$$

51

For a linear elastic material, the constitutive relation is given by Equation 3.30, so σ_{11} is:

$$\sigma_{11} = (K - \frac{2}{3}G)(e_{11} + e_{22}) + 2Ge_{11}$$

Therefore, the dilatational wave speed in the x_1-direction becomes:

$$C'_p = \sqrt{\frac{K + \frac{4}{3}G}{\rho}} \tag{3.44}$$

In a rigorous sense, the determination of the critical time step includes an analysis of the smallest natural period of vibration of the system. Such calculation is impractical because it takes a computational effort similar to the dynamic relaxation procedure. However, some codes are based on estimates of this natural period. In CHIMP [104], the numerical stability condition is estimated to be that of the undamped explicit central differencing method (damping used in CHIMP is velocity proportional), such that:

$$t^{n+\frac{1}{2}} \leq \frac{2}{\omega_{max}}$$

where t is the time step, and ω_{max} is the highest natural angular frequency of the undamped mesh, which can be conservatively estimated using the local speed of infinitesimal waves. This leads to:

$$t^{n+\frac{1}{2}} \leq \min\left(\frac{\epsilon}{C}\right)$$

where ϵ is the minimum of the lengths of the zone edges and diagonals, and C is the local speed in the reference configuration. This approach will

52

determine the time step for the smallest zone size; since ϵ can vary over orders of magnitude through the mesh, it would severely limit the efficiency of the code.

It is possible to manipulate the local wave speed by changing the mass density ρ. Since $C \propto \frac{1}{\sqrt{\rho}}$ for a given constitutive relation, it can be set to any desired value by adjusting the local density (Underwood [123]). The point is to find a density distribution which provides a uniform stable time step for all zones (density scaling). This will not affect the end results since the problems dealt with are static and, in the static equilibrium equations, the mass density term does not appear. Therefore, these manipulations can be made arbitrarily without influencing the asymptotic solution to the dynamic equation for balance of linear momentum. The gravitational forces are not affected by this scaling.

3.13.1 Density scaling for a linear elastic material

Following the procedure outlined by Underwood [123], the time step is set equal to unity, and the nodal masses are adjusted to provide this value. For a triangle, the minimum propagation distance can be estimated as $A/\Delta x_{max}$, where A is the area of the triangle and Δx_{max} is the largest side of the triangle (which is the diagonal of the corresponding quadrilateral). Using equation 3.42, the following relationship is obtained:

$$\Delta t = \frac{A}{C_p \Delta x_{max}} \tag{3.45}$$

53

Substituting $\Delta t = 1$, and Equation 3.44 into Equation 3.45, gives:

$$\rho = \frac{(K + \frac{4}{3}G)\Delta x_{max}}{A^2} \tag{3.46}$$

The mass associated with the triangle is $m_t = \rho A$; therefore,

$$m_t = \frac{(K + \frac{4}{3}G)\Delta x_{max}}{A}. \tag{3.47}$$

However, it is necessary to lump masses to gridpoints, so the motion equation can be solved at this level. Last and Harkness [58] present a procedure to lump masses to gridpoints in which the center of gravity of the triangle is not modified. His results point out that lumping one third of the subzone mass into each node will preserve the location of the center of mass of the quadrilateral. Hence, the mass for each gridpoint in the triangle is:

$$m_{gp} = \frac{1}{3}m_t. \tag{3.48}$$

The net gridpoint mass for each node in the mesh is given by the sum of the masses of all triangles connected to that gridpoint, including the two sets of overlapping triangles; therefore, the summation needs to be divided by two. This summation includes all quadrilaterals sharing a particular gridpoint (maximum of four). The expresion for the net gridpoint mass becomes:

$$m_n = \sum \frac{m_{gp}}{2}. \tag{3.49}$$

Since this procedure yields an estimation of the critical time step, a safety factor can be applied. The safety factor adopted here was 0.8, i.e., the critical time step is set to 0.8 instead of 1.

54

3.13.2 Density scaling for a trilinear material

The nodal masses associated with the gridpoints are determined with the same expressions as presented in Equations 3.45, 3.46, 3.47. However, depending on the strain level, the effective moduli are degraded and some areas of the body will have different properties than others. Therefore, nodal masses have to be recalculated for each mechanical time step, as strain increases in order to speed up the convergence of the dynamic relaxation process. If the dependence of the effective moduli upon confining pressure, for example, is to be included, the equations for the nodal masses are not the same and turn out to be complicated expressions [14].

3.14 Mechanical portion verification test

The problem that has been chosen in order to verify the accuracy of the code is the determination of stresses and displacements induced by a cylindrical hole in an infinite, isotropic, linear elastic medium, subjected to a uniform in-situ stress field. Plane strain conditions, perpendicular to the borehole axis, are assumed. The analytical solution for this problem was formulated by Kirsch (see Jaeger and Cook, [53]).

A point located at a polar coordinate (r, θ), near an opening of radius a (Figure 3.8) will experience stresses and displacements given by:

$$\sigma_r = \frac{P_1 + P_2}{2}\left(1 - \frac{a^2}{r^2}\right) + \frac{P_1 - P_2}{2}\left(1 - \frac{4a^2}{r^2} + \frac{3a^4}{r^4}\right)\cos(2\theta) \quad (3.50)$$

$$\sigma_\theta = \frac{P_1 + P_2}{2}\left(1 + \frac{a^2}{r^2}\right) - \frac{P_1 - P_2}{2}\left(1 + \frac{3a^4}{r^4}\right)\cos(2\theta) \qquad (3.51)$$

$$\tau_{r\theta} = \frac{P_1 + P_2}{2}\left(1 + \frac{2a^2}{r^2} - \frac{3a^4}{r^4}\right)\sin(2\theta) \qquad (3.52)$$

The analytical solution for the displacements (Jaeger and Cook [53]) is :

$$u_r = \frac{P_1 + P_2}{4G}\frac{a^2}{r^2} + \frac{P_1 - P_2}{4G}\frac{a^2}{r^2}\left[4(1 - \nu) - \frac{a^2}{r^2}\right]\cos(2\theta) \qquad (3.53)$$

$$v_\theta = -\frac{P_1 - P_2}{4G}\frac{a^2}{r^2}\left[2(1 - 2\nu) + \frac{a^2}{r^2}\right]\sin(2\theta) \qquad (3.54)$$

In these equations, G is the shear modulus of the rock, ν is the Poisson's ratio, u_r is the radial displacement, and v_θ is the tangential displacement.

The finite difference mesh and boundary conditions used for this problem are shown in Figure 3.9. Symmetry of the problem permits modeling only a quarter of the medium. The mesh is composed of 900 quadrilateral elements. The mesh has been refined near the borehole where the stress gradients and displacements are greater in magnitude then further away from the borehole. The element size is increased as the radial distance increases. The hydrostatic far-field stresses are set at -30 MPa (compressive field), which are input as initial stresses in the elements. The material properties used are:$E = 6.7GPa$,$\nu = 0.21$, $\rho = 2500Kg/m^3$.

The process of dynamic relaxation of the system is illustraded in Figure 3.10, in which the out-of-balance forces are plotted against pseudo time steps at the borehole wall. A total of 2350 time steps were needed to lower the out-of-balance forces four orders of magnitude. At this point, the system is considered to be in equilibrium. The numerical results for stresses and

56
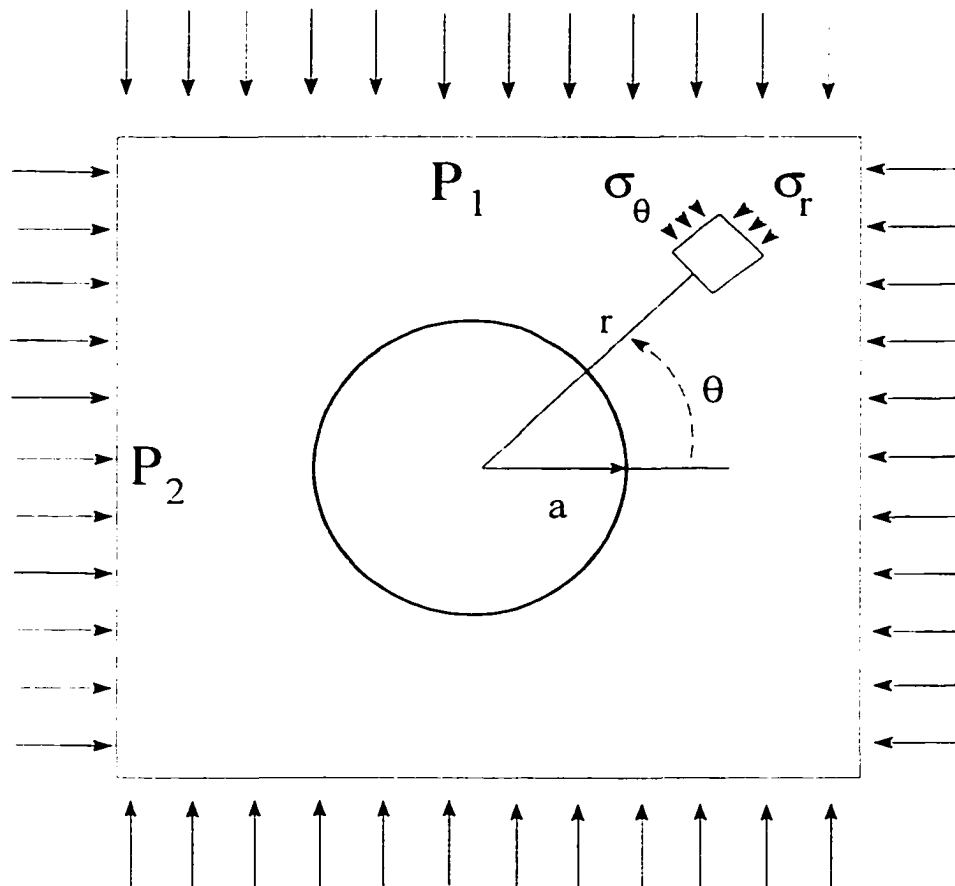
Figure 3.8: Schematic representation of a borehole subjected to an in-situ stress field

57

PLEASE NOTE

**Page(s) not included with original material
and unavailable from author or university.
Filmed as received.**

UMI
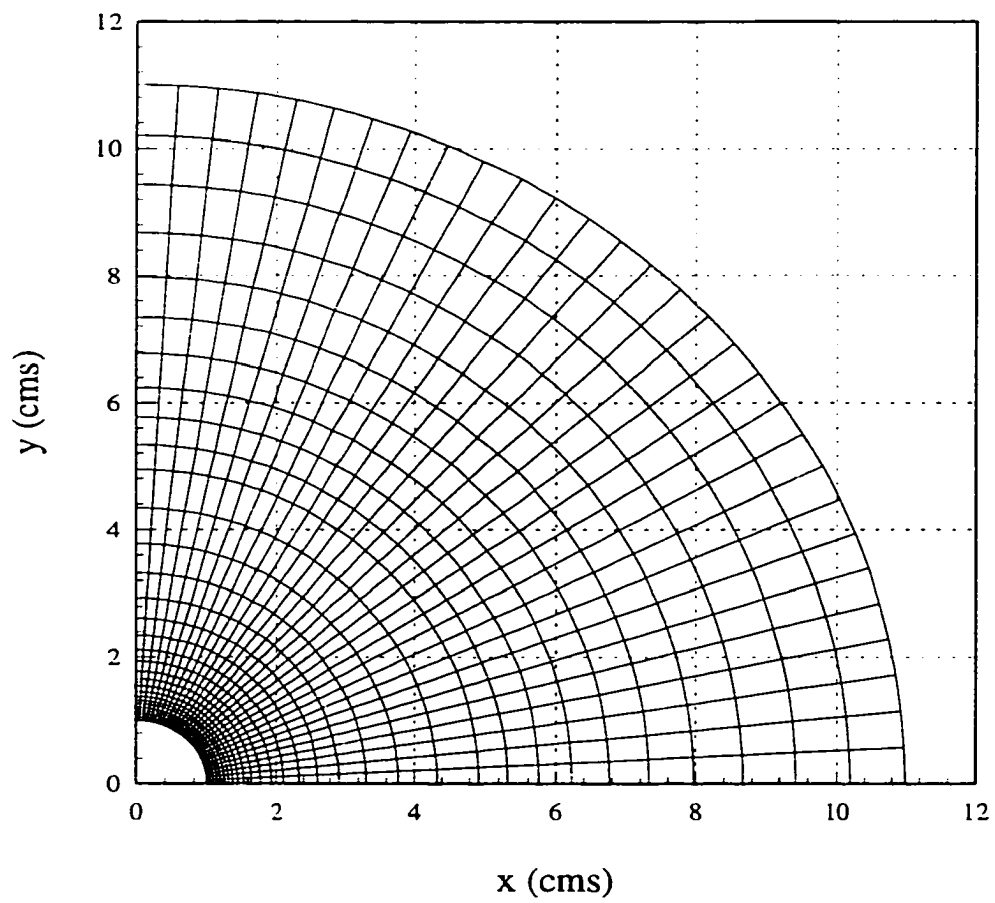
Figure 3.9: Finite difference mesh used for the borehole problem
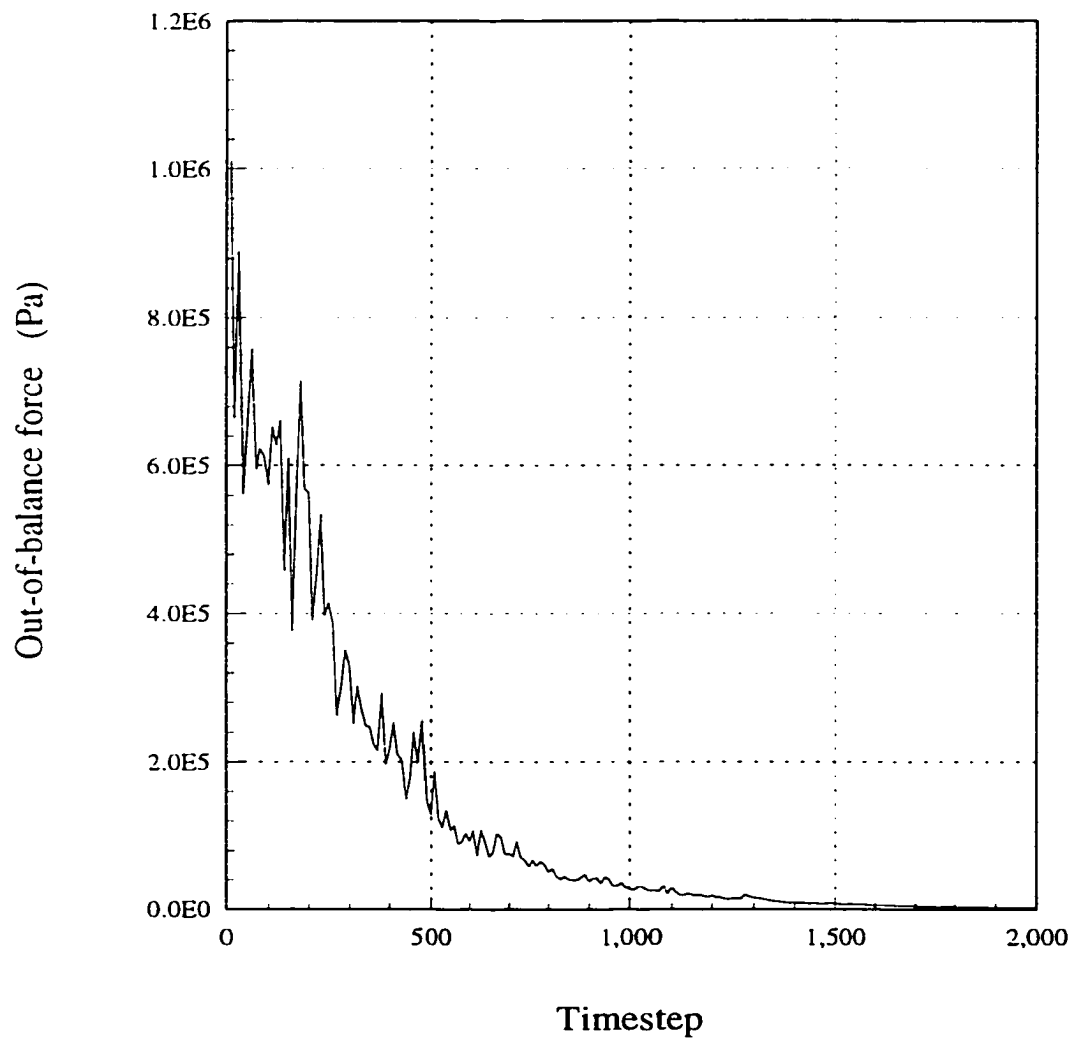
Figure 3.10: Evolution in time of the maximum out-of-balance force in the system

60
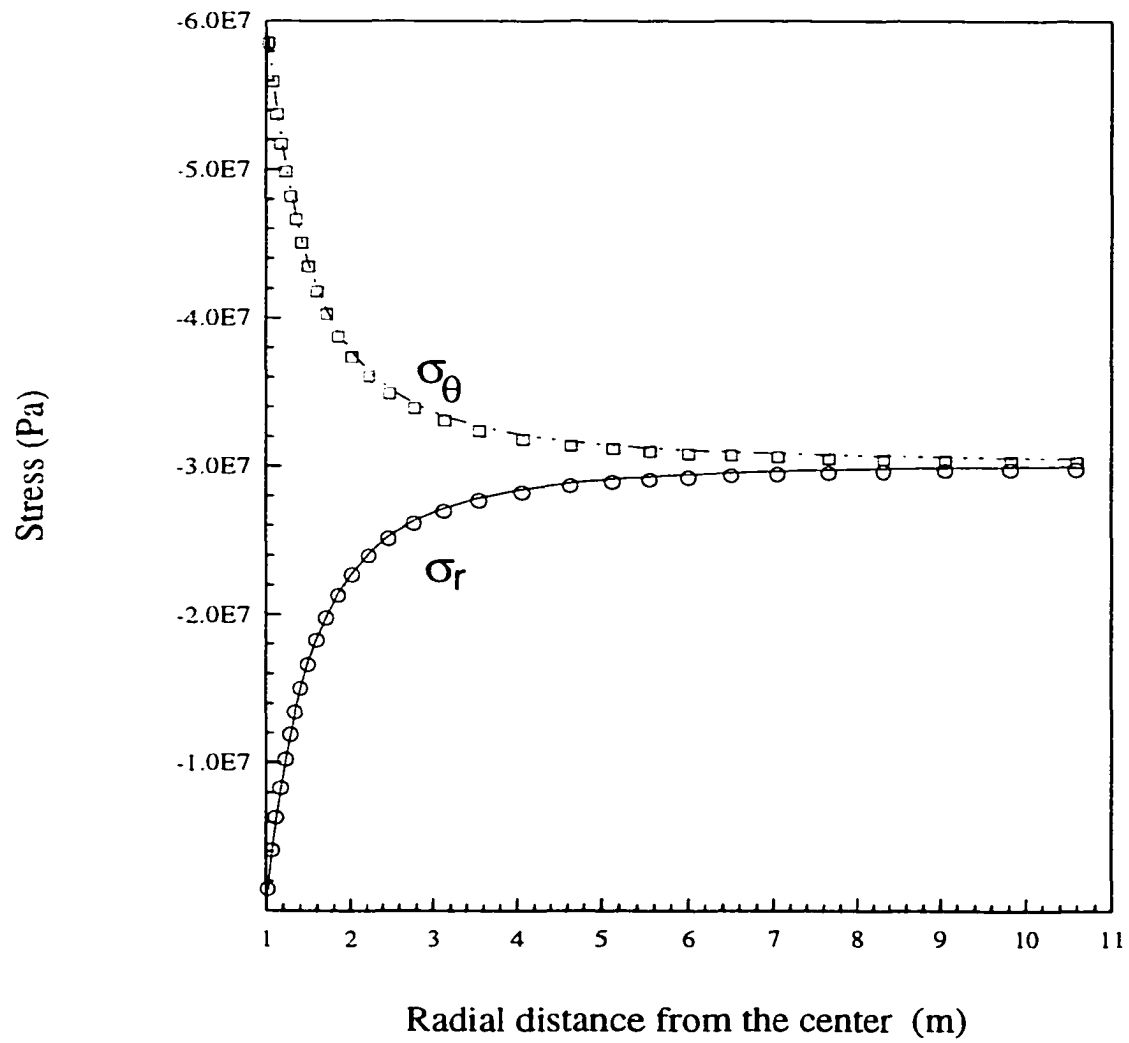
Figure 3.11: Comparison between analytical (lines) and numerical (symbols) results for tangential and radial stresses

61
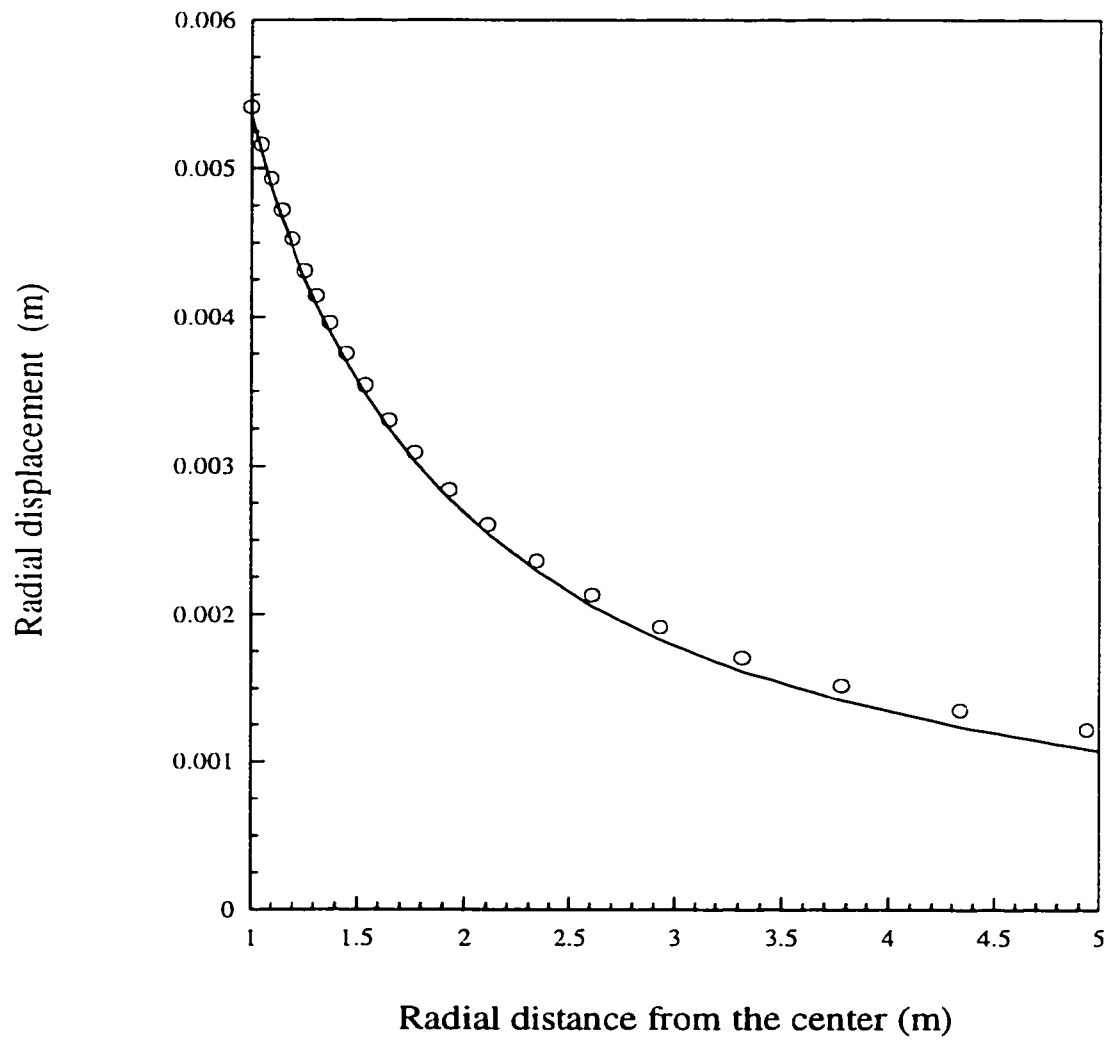
Figure 3.12: Comparison between analytical (line) and numerical (symbol) results for radial displacements

62

Chapter 4

Governing Equations for Multiphase Flow in a Deforming Porous Medium

4.1 Introduction

An oil reservoir can be envisioned as a multiphase mixture, gas, water and the rock. The basic formulation for multiphase flow in a deforming porous medium is presented by Li and Zienkiewicz [66], Lewis and Schrefler [61] and others [99]. The most pertinent derivations presented in this chapter follow the formalism in references [66] and [64] for the case of two-phase flow in deforming porous media. Constants are regrouped and redefined here to facilitate the subsequent numerical solution by the explicit Lagrangian finite difference technique.

63

4.2 Immiscible two-phase fluid flow in a deforming porous media

Consider a representative elementary volume in a domain containing the mixture of the following α-constituents: solid, a wetting fluid phase and a non-wetting phase ($\alpha = s, w, n$, respectively). Pore space is represented by porosity, ϕ. The volume fraction that is rock is, therefore, $1 - \phi$ (the volume fraction of the fluis is ϕ). The fraction of pore space occupied by each fluid is referred to as the saturation (S_w for the wetting phase, and S_n for the non-wetting phase). These quantities obey the constraint:

$$S_w + S_n = 1. \tag{4.1}$$

4.2.1 Fluid pressure in a multiphase flow regime

The distribution of fluids in the rock depends on the interfacial tension, pore geometry (capillary radii), wettability (contact angle with the rock), stresses, and, in general, is a strong function of the saturation history [98], [61]. Since these parameters change in time and space, defining pore pressure is a difficult task.

Several assumptions can be made concerning the definition of pore pressure. It can be considered that both fluids are in contact with the solid, so the pore pressure is expressed as:

$$P = S_w P_w + S_n P_n, \tag{4.2}$$

64

or alternatively, it can be assumed that:

$$P = P_w \tag{4.3}$$

if only the wetting fluid is considered to be in contact with the solid. This last assumption is made for the derivation that follows.

4.2.2 Effective Stress Concept

Effective stress ia by definition:

$$\sigma_{ij} = \sigma'_{ij} - \alpha\delta_{ij}p, \tag{4.4}$$

where σ'_{ij} is the effective stress and p is the pore pressure. Biot's poroelastic coefficient can be expressed by [92]:

$$\alpha = 1 - \frac{K_t}{K_s} \tag{4.5}$$

where K_s and K_t are the bulk moduli of solid grains and framework, respectively. The parameter α can also be expressed in terms of other parameters such as the Skempton coefficient, B and drained and undrained Poisson's ratio, ν and ν_u, respectively [31]. For simplicity, the expression given by Equation 4.5 is used in this derivation.

4.2.3 Governing equations

The continuum isothermal approach for solid and fluid mechanics includes the following laws and relationships for each component:

1. mass conservation

2. momentum conservation

3. constitutive or state equations

4. effective stress law for the fluid-permeated solid.

Mass Conservation

The solid mass volume, M_s, can be expressed as the volume fraction of the-porous solid, $(V_s = (1 - \phi)V)$, times the density of the solid (ρ_s). Therefore, mass conservation for the solid requires that:

$$\frac{DM_s}{Dt} = \frac{D}{Dt} \int_V (1 - \phi)\rho_s dv = 0$$

or

$$\frac{\partial(1 - \phi)\rho_s}{\partial t} + \frac{\partial(1 - \phi)\rho_s u_i}{\partial x_i} = 0 \tag{4.6}$$

where u_i is the solid velocity. Similarly, the mass conservation equations for the wetting and non-wetting phases are:

$$\frac{\partial \phi S_w \rho_w}{\partial t} + \frac{\partial \phi S_w \rho_w U_{wi}}{\partial x_i} = 0 \tag{4.7}$$

$$\frac{\partial \phi S_n \rho_n}{\partial t} + \frac{\partial \phi S_n \rho_n U_{ni}}{\partial x_i} = 0 \tag{4.8}$$

where U_{wi} and U_{ni} are the intrinsic velocities for each fluid. The volume fraction of the corresponding fluid is ϕS_l $(l = w, n)$.

66

The superficial, or Darcy velocities, are defined as:

$$w_i = \phi S_w (U_{wi} - u_i) \tag{4.9}$$

$$v_i = \phi S_n (U_{ni} - u_i) \tag{4.10}$$

where w_i and v_i denote the wetting and non-wetting fluid velocities, respectively.

Substituting the definitions given by Eqs. 4.9 and 4.10 into Eqs. 4.6- 4.8, and expanding derivatives gives:

$$(1 - \phi)\frac{\partial \rho_s}{\partial t} - \rho_s \frac{\partial \phi}{\partial t} + (1 - \phi)\rho_s u_{i,i} + \frac{\partial(1 - \phi)\rho_s}{\partial x_i} u_i \quad = 0 \tag{4.11}$$

$$\frac{\partial \phi S_w \rho_w}{\partial t} + \frac{\partial(\phi S_w \rho_w u_i)}{\partial x_i} + \frac{\partial \rho_w w_i}{\partial x_i} \quad = 0 \tag{4.12}$$

$$\frac{\partial \phi S_n \rho_n}{\partial t} + \frac{\partial(\phi S_n \rho_n u_i)}{\partial x_i} + \frac{\partial \rho_n v_i}{\partial x_i} \quad = 0. \tag{4.13}$$

or

$$(1 - \phi)\left(\frac{\partial \rho_s}{\partial t} + u_i \frac{\partial \rho_s}{\partial x_i}\right) - \rho_s \left(\frac{\partial \phi}{\partial t} + \frac{\partial \phi}{\partial x_i} u_i\right)$$
$$+ (1 - \phi)\rho_s u_{i,i} = 0 \tag{4.14}$$

$$S_w \rho_w \left(\frac{\partial \phi}{\partial t} + u_i \frac{\partial \phi}{\partial x_i}\right) + \phi\left(\frac{\partial \rho_w S_w}{\partial t} + u_i \frac{\partial \rho_w S_w}{\partial x_i}\right)$$
$$+ \frac{\partial \rho_w w_i}{\partial x_i} + \phi \rho_w S_w u_{i,i} = 0 \tag{4.15}$$

$$S_n \rho_n \left(\frac{\partial \phi}{\partial t} + u_i \frac{\partial \phi}{\partial x_i}\right) + \phi\left(\frac{\partial \rho_n S_n}{\partial t} + u_i \frac{\partial \rho_n S_n}{\partial x_i}\right)$$
$$+ \frac{\partial \rho_n v_i}{\partial x_i} + \phi \rho_n S_n u_{i,i} = 0 \tag{4.16}$$

$$\tag{4.17}$$

67

Using the definition of material derivative, i.e. $\frac{D}{Dt} = \frac{\partial}{\partial t} + u_i \frac{\partial}{\partial x_i}$, with respect to the *solid velocity*, the previous equations result in:

$$\frac{(1-\phi)}{\rho_s}\frac{D\rho_s}{Dt} - \frac{D\phi}{Dt} + (1-\phi)u_{i,i} \quad = 0 \qquad (4.18)$$

$$\frac{\phi}{S_w\rho_w}\frac{D(S_w\rho_w)}{Dt} + \frac{D\phi}{Dt} + \phi u_{i,i} + \frac{1}{S_w}w_{i,i} + \frac{w_i}{S_w\rho_w}\frac{\partial\rho_w}{\partial x_i} \quad = 0 \qquad (4.19)$$

$$\frac{\phi}{S_n\rho_n}\frac{D(S_n\rho_n)}{Dt} + \frac{D\phi}{Dt} + \phi u_{i,i} + \frac{1}{S_n}v_{i,i} + \frac{v_i}{S_n\rho_n}\frac{\partial\rho_n}{\partial x_i} \quad = 0, \qquad (4.20)$$

after dividing Eq. 4.18 by ρ_s, dividing Eq. 4.19 by $S_w\rho_w$ and dividing Eq. 4.20 by $S_n\rho_n$. Adding Eq. 4.18 to Eqs. 4.19 and 4.20 allows the elimination of the term $\frac{D\phi}{Dt}$, yielding two equations:

$$\frac{(1-\phi)}{\rho_s}\frac{D\rho_s}{Dt} + \frac{\phi}{S_w}\frac{DS_w}{Dt} + \frac{\phi}{\rho_w}\frac{D\rho_w}{Dt} + u_{i,i} + \frac{1}{S_w}w_{i,i}$$
$$+ \frac{w_i}{S_w\rho_w}\frac{\partial\rho_w}{\partial x_i} \quad = 0 \qquad (4.21)$$

$$\frac{(1-\phi)}{\rho_s}\frac{D\rho_s}{Dt} + \frac{\phi}{S_n}\frac{DS_n}{Dt} + \frac{\phi}{\rho_n}\frac{D\rho_n}{Dt} + u_{i,i} + \frac{1}{S_n}v_{i,i}$$
$$+ \frac{v_i}{S_n\rho_n}\frac{\partial\rho_n}{\partial x_i} \quad = 0 \qquad (4.22)$$

The relationship between change in pressure and change in volume is given through the concept of compressibility, $C = -\frac{1}{V}(dV/dp)$, or alternatively, by the stiffness, $K = 1/C$. Using the stiffness definition and the mass balance equations for each component in the mixture, namely,

$$\frac{D(\rho_s V_s)}{Dt} = 0,$$
$$\frac{D(\rho_w V_w)}{Dt} = 0, \qquad (4.23)$$
$$\frac{D(\rho_n V_n)}{Dt} = 0,$$

68

the following expressions are obtained:

1. for the wetting fluid:

$$\frac{1}{\rho_w}\frac{D\rho_w}{Dt} = -\frac{1}{V_w}\frac{DV_w}{Dt} = \frac{1}{K_w}\frac{DP_w}{Dt}; \qquad (4.24)$$

2. for the non-wetting fluid:

$$\frac{1}{\rho_n}\frac{D\rho_n}{Dt} = -\frac{1}{V_n}\frac{DV_n}{Dt} = \frac{1}{K_n}\frac{DP_n}{Dt}; \qquad (4.25)$$

3. for the solid,

$$\frac{1}{\rho_s}\frac{D\rho_s}{Dt} = -\frac{1}{V_s}\frac{DV_s}{Dt} = \frac{1}{K_s}\frac{DP_w}{Dt} - \frac{\sigma'_{ii}}{3(1-\phi)K_s} \qquad (4.26)$$

Since the *hydrostatic pressure* is:

$$\sigma_{ii} = 3K_t\left(u_{i,i} + \frac{1}{K_s}\frac{DP_w}{Dt}\right) \qquad (4.27)$$

and with $K_t = K_s(1 - \alpha)$, from Equation 4.5, then:

$$\frac{1}{\rho_s}\frac{D\rho_s}{Dt} = \left[(\alpha - \phi)\frac{1}{K_s}\frac{DP_w}{Dt} - (1-\alpha)u_{i,i}\right]\frac{1}{(1-\phi)}. \qquad (4.28)$$

69

Next, Equations. 4.24, 4.25 and 4.28 are substituted into Equations 4.21 and 4.22, and together with the restriction of Equation 4.1, the results are:

$$\frac{(\alpha - \phi)}{K_s}\frac{DP_w}{Dt} + \alpha u_{i,i} + \frac{\phi}{K_w}\frac{DP_w}{Dt} + \frac{\phi}{S_w}\frac{DS_w}{Dt} + \frac{1}{S_w}w_{i,i} +$$
$$\frac{w_i}{S_w\rho_w}\rho_{w,i} = 0 \quad (4.29)$$

$$\frac{(\alpha - \phi)}{K_s}\frac{DP_w}{Dt} + \alpha u_{i,i} + \frac{\phi}{K_n}\frac{DP_n}{Dt} + \frac{\phi}{S_n}\frac{DS_n}{Dt} + \frac{1}{S_n}v_{i,i} +$$
$$\frac{v_i}{S_n\rho_n}\rho_{n,i} = 0 \quad (4.30)$$

Making use of the relationship for the capillary pressure as a function of the pressure difference in the fluids, it is known that:

$$\frac{DP_n}{Dt} = \frac{DP_c}{Dt} + \frac{DP_w}{Dt} \quad (4.31)$$

and from Equation 4.1:

$$\frac{DS_n}{Dt} = -\frac{DS_w}{Dt}. \quad (4.32)$$

Also, it can be shown that:

$$\frac{DP_c}{Dt} = \frac{dP_c}{dS_w}\frac{DS_w}{Dt}, \quad (4.33)$$

since it has been assumed that $P_c = P_c(S_w)$.

Substituting these expressions into Equation 4.30 gives:

$$\frac{\alpha - \phi}{K_s}\frac{DP_w}{Dt} + \alpha u_{i,i} + \frac{\phi}{K_n}\left(P_c'\frac{DS_w}{Dt} + \frac{DP_w}{Dt}\right) - \frac{\phi}{S_n}\frac{DS_w}{Dt} +$$
$$\frac{v_{i,i}}{S_n} + \frac{v_i}{S_n\rho_n}\rho_{n,i} = 0 \quad (4.34)$$

70

Grouping terms in Eq. 4.29 and 4.34 gives:

$$S_w \frac{D P_w}{Dt}\left(\frac{\alpha - \phi}{K_s} + \frac{\phi}{K_w}\right) + \phi\frac{DS_w}{Dt}$$
$$+ \alpha S_w u_{i,i} + w_{i,i} + \frac{w_i}{\rho_w}\rho_{w,i} = 0 \qquad (4.35)$$

$$S_n \frac{D P_w}{Dt}\left(\frac{\alpha - \phi}{K_s} + \frac{\phi}{K_n}\right) + \phi\frac{DS_w}{Dt}\left(\frac{1}{K_n}P_c'S_n - 1\right)$$
$$+ \alpha S_n u_{i,i} + v_{i,i} + \frac{v_i}{\rho_n}\rho_{n,i} = 0 \qquad (4.36)$$

These can be written as:

$$S_w C_{w1}\frac{D P_w}{Dt} + C_{w2}\frac{DS_w}{Dt} + \alpha S_w u_{i,i} + w_{i,i} + \frac{w_i}{\rho_w}\rho_{w,i} = 0 \qquad (4.37)$$

$$S_n C_{n1}\frac{D P_w}{Dt} + C_{n2}\frac{DS_w}{Dt} + \alpha S_n u_{i,i} + v_{i,i} + \frac{v_i}{\rho_n}\rho_{n,i} = 0 \qquad (4.38)$$

where,

$$C_{w1} = \left[\frac{(\alpha - \phi)}{K_s} + \frac{\phi}{K_w}\right] \qquad (4.39)$$

$$C_{w2} = \phi \qquad (4.40)$$

$$C_{n1} = \left[\frac{(\alpha - \phi)}{K_s} + \frac{\phi}{K_n}\right] \qquad (4.41)$$

$$C_{n2} = \phi\left[\frac{dP_c}{dS_w}\frac{S_n}{K_n} - 1\right] \qquad (4.42)$$

Expanding the material derivatives, and grouping the terms in Eqs. 4.37 and 4.38, a set of equations $AX = B$ for the unknowns $\dot{P}_w$ and $\dot{S}_w$ is obtained:

$$\begin{pmatrix} a_{11} & a_{12} \\ a_{21} & a_{22} \end{pmatrix}\begin{pmatrix} \dot{P}_w \\ \dot{S}_w \end{pmatrix} = \begin{pmatrix} b_1 \\ b_2 \end{pmatrix} \qquad (4.43)$$

where $\dot{P}_w$ and $\dot{S}_w$ stand for partial derivatives with respect to time of water pressure and water saturation, respectively. The terms in matrix A are

71

defined as:

$$a_{11} = S_w C_{w1}; \quad a_{12} = C_{w2}$$

$$a_{21} = S_n C_{n1}; \quad a_{22} = C_{n2} \tag{4.44}$$

and the matrix B is:

$$b_1 = -S_w C_{w1} u_i P_{w,i} - C_{w2} u_i S_{w,i} - \alpha S_w u_{i,i} - w_{i,i} - \frac{w_i}{\rho_w} \rho_{w,i} \tag{4.45}$$

$$b_2 = -S_n C_{n1} u_i P_{w,i} - C_{n2} u_i S_{w,i} - \alpha S_n u_{i,i} - v_{i,i} - \frac{v_i}{\rho_n} \rho_{n,i} \tag{4.46}$$

This set of equations can be solved as $X = A^{-1} B$, which gives:

$$
\begin{aligned}
\dot{P}_w &= \frac{S_n C_{w2} - S_w C_{n2}}{D_p} \alpha u_{i,i} - u_i P_{w,i} \\
&+ \frac{1}{D_p}\left(v_{i,i} C_{w2} - w_{i,i} C_{n2} + \frac{v_i}{\rho_n} \rho_{n,i} C_{w2} - \frac{w_i}{\rho_w} \rho_{w,i} C_{n2} \right) \tag{4.47}
\end{aligned}
$$

$$
\begin{aligned}
\dot{S}_w &= \frac{S_n S_w (C_{n1} - C_{w1})}{D_p} \alpha u_{i,i} - u_i S_{w,i} + \frac{1}{D_p}\left(w_{i,i} S_n C_{n1} - v_{i,i} S_w C_{w1} \right) \\
&+ \frac{1}{D_p}\left(\frac{w_i}{\rho_w} \rho_{w,i} S_n C_{n1} - \frac{v_i}{\rho_n} \rho_{n,i} S_w C_{w1} \right) \tag{4.48}
\end{aligned}
$$

where $D_p = S_w C_{w1} C_{n2} - S_n C_{n1} C_{w2}$.

The density gradient appearing in these equations can be written in terms of pressure by using state equations for the fluids. These relationships are of the form:

$$\rho = \rho_o \exp\left[C(P - P_o)\right] \tag{4.49}$$

where C is the compressibility of the fluid, P_o is a datum, or initial pressure, and P is any pressure at which the density is to be evaluated. For slightly

72

compressible fluids, this equation can be approximated as:

$$\rho = \rho_o + \frac{\rho_o}{K}(\Delta P) \tag{4.50}$$

The relationship for the wetting fluid is:

$$\rho_w = \rho_{wo} + \rho_{wo}(p_w - p_{wo})\frac{1}{K_w}.$$

and, consequently,

$$\frac{w_i}{\rho_w}\rho_{w,i} = \left(\frac{w_i}{K_w + p_w - p_{wo}}\right)p_{w,i}$$

Similarly, for the non-wetting phase it results in:

$$\frac{v_i}{\rho_n}\rho_{n,i} = \left(\frac{v_i}{K_n + p_n - p_{no}}\right)p_{n,i}.$$

Substituting these expressions into Equations 4.47 and 4.48 will explicitly eliminate the densities . The resulting equations are written in short form as:

$$\dot{P}_w = f_p u_{i,i} + P_{wf} \tag{4.51}$$

$$\dot{S}_w = f_s u_{i,i} + S_{wf} \tag{4.52}$$

in which the first term in both equations represents the contribution of the solid volumetric deformation, $u_{i,i}$, and the second terms, P_{wf} and S_{wf}, correspond to the fluid flow processes. These terms are:

$$f_p = \alpha\frac{S_n C_{w2} - S_w C_{n2}}{D_p} \tag{4.53}$$

$$f_s = \alpha\frac{S_n S_w(C_{n1} - C_{w1})}{D_p} \tag{4.54}$$

73

and.

$$P_{wf} = \frac{1}{D_p}\left(v_{i,i}C_{w2} - w_{i,i}C_{n2}\right) - u_i P_{w,i}$$
$$+ \quad \frac{1}{D_p}\left(P_{n,i}v_i\frac{C_{w2}}{K_n + P_n - P_{no}} - P_{w,i}w_i\frac{C_{n2}}{K_w + P_w - P_{wo}}\right) \quad (4.55)$$

and.

$$S_{wf} = \frac{1}{D_p}\left(w_{i,i}S_n C_{n1} - v_{i,i}S_w C_{w1}\right) - u_i S_{w,i}$$
$$+ \quad \frac{1}{D_p}\left(P_{w,i}w_i\frac{S_n C_{n1}}{K_w + P_w - P_{wo}} - P_{n,i}v_i\frac{S_w C_{w1}}{K_n + P_n - P_{no}}\right) \quad (4.56)$$

The equation for the evolution of the porosity is obtained combining Eq. 4.18 together with Eq. 4.28 to give:

$$\frac{D\phi}{Dt} = (\alpha - \phi)\left(\frac{1}{K_s}\frac{DP_w}{Dt} + u_{i,i}\right) \quad (4.57)$$

Momentum conservation

For a unit element of the porous medium mixture, the momentum balance equation can be written as:

$$\sigma_{ij,j} + \rho b_i - \rho\frac{Du_i}{Dt} - \phi S_w \rho_w \frac{D}{Dt}\left(\frac{w_i}{\phi S_w}\right) - \phi S_n \rho_n \frac{D}{Dt}\left(\frac{v_i}{\phi S_n}\right) = 0. \quad (4.58)$$

In this equation, ρ is the density of the mixture, which is defined as:

$$\rho = \rho_s(1 - \phi) + \rho_w \phi S_w + \rho_n \phi S_n. \quad (4.59)$$

The terms expressing the relative acceleration of the fluids are neglected. This is reasonable for quasi-static processes, which is the case here. Using the effective stress concept, Equation 4.4, and knowing that $\frac{Du_i}{Dt}$ is the

74

acceleration of the solid, a_i, the motion equation for the mixture is:

$$\sigma'_{ji,j} - \alpha(P_w)_{,i} + \rho b_i - \rho a_i = 0 \qquad (4.60)$$

The equation of motion can alsobe written for each component individually. Hence, the equation of motion for the wetting phase is:

$$-\phi S_w \frac{\partial p_w}{\partial x_i} + \phi S_w \rho_w b_i - \phi S_w \rho_w \frac{Du_i}{Dt} - \phi S_w \rho_w \frac{\partial(w_i/\phi S_w)}{\partial t} = R_{wi} \qquad (4.61)$$

where R_{wi} is the momentum exchange (coupling force acting on the wetting phase). This force is assumed to take the form of Darcy's law, i.e.

$$\frac{R_{wi}}{\phi S_w} = \frac{w_j}{\Lambda_{w_{ij}}} \qquad (4.62)$$

where $\Lambda_{w_{ij}}$ is the fluid mobility, which can be evaluated as:

$$\Lambda_{w_{ij}} = k_{w_{ij}} \frac{k_{rw}(S_w)}{\mu_w(P_w)}. \qquad (4.63)$$

Here, $k_{w_{ij}}$ is the absolute permeability of the wetting fluid and k_{rw} is the relative permeability. Substituting Equations 4.62 and 4.63 into Equation 4.61, the wetting fluid velocity gives:

$$w_i = \Lambda_{w_{ij}}(-p_{w,j} + \rho_w b_j - \rho_w a_j) \qquad (4.64)$$

The relationship for the non-wetting fluid is obtained in a similar manner, giving:

$$v_i = \Lambda_{n_{ij}}(-P_{n,j} + \rho_n b_j - \rho_n a_j) \qquad (4.65)$$

75

where $\Lambda_{n_{ij}}$ is defined as:

$$\Lambda_{n_{ij}} = k_{n_{ij}} \frac{k_{rn}(S_n)}{\mu_n(P_n)}. \tag{4.66}$$

In this equation, $k_{n_{ij}}$ and k_{rn} are the absolute and relative permeabilities with respect to the non-wetting phase, respectively.

Summarizing, the equations to be solved numerically are:

- motion equation for the mixture in terms of effective stresses, Eq. 4.60,

$$\left(\sigma'_{ij} - \alpha p_w\right)_{,j} + \rho b_i - \rho a_i = 0,$$

- mass conservation, Eq. 4.51, Eq. 4.52, Eq. 4.55, Eq. 4.56,

$$\dot{P}_w = u_{i,i} f_p + P_{wf},$$

$$\dot{S}_w = u_{i,i} f_s + S_{wf},$$

- fluid velocities (modified Darcy's law for the two fluids):

$$w_i = \Lambda_{w_{ij}}(-p_{w,j} + \rho_w b_j - \rho_w a_j),$$

and,

$$v_i = \Lambda_{n_{ij}}(-p_{n,j} + \rho_n b_j - \rho_n a_j).$$

76

Chapter 5

Numerical Solution of the Coupled Equations of Two-Phase Flow in a Deforming Porous Medium

5.1 Introduction

The procedure used to solve the system of coupled equations describing two-phase flow in a deforming porous medium is based on the following premise: because the pore pressure and saturation changes have one component related to the volumetric strain of the solid and the other related to the fluid flow parameters (mobilities, pressure gradients, divergencies) these components can be separated at each time step, while maintaining coupling. This is done by including undrained pore pressure and saturation changes due to volumetric solid strain in what is called the 'mechanical portion' of the calculation and the drained pore pressure and saturation changes in the 'fluid

77

flow calculation portion'.

For each real time step, the mechanical portion evolves instantaneously; no real time elapses. Due to the volumetric deformation of the solid and fluid compressibility contrast, there are undrained pore pressure and saturation changes during the mechanical portion. There is a change in effective stress, and strains are produced according to the constitutive equation. Equilibrium for the *mixture*, solid plus fluids, is achieved through dynamic relaxation at each time step (see Chapter 3). The solid is permeated by fluids that will move (deform) according to the motion equation (which has been written in terms of the mixture of solid plus two fluids). The out of balance forces are determined and the resulting velocity of the solid and corresponding strain rate are calculated. Following, flow and dissipation of pore pressure take place. The fluid flow portion consists on marching in real time by integrating the mass balance equations and generalized Darcy's law (Equations 4.51, 4.52, 4.64 and 4.65 in Chapter 4). The calculation steps are represented schematically in Figure 5.1.

In a fluid permeated porous solid, the system is brought out of balance by the following factors: a) external loading; b) gravity; c) velocity constraints; d) pore pressure and/or saturation changes, both undrained (from the mechanical portion) and drained (from the fluid flow portion) and, consequently, e) changes in *effective and total stresses*. The dynamic relaxation procedure during the mechanical calculation ensures that the entire mixture is put back
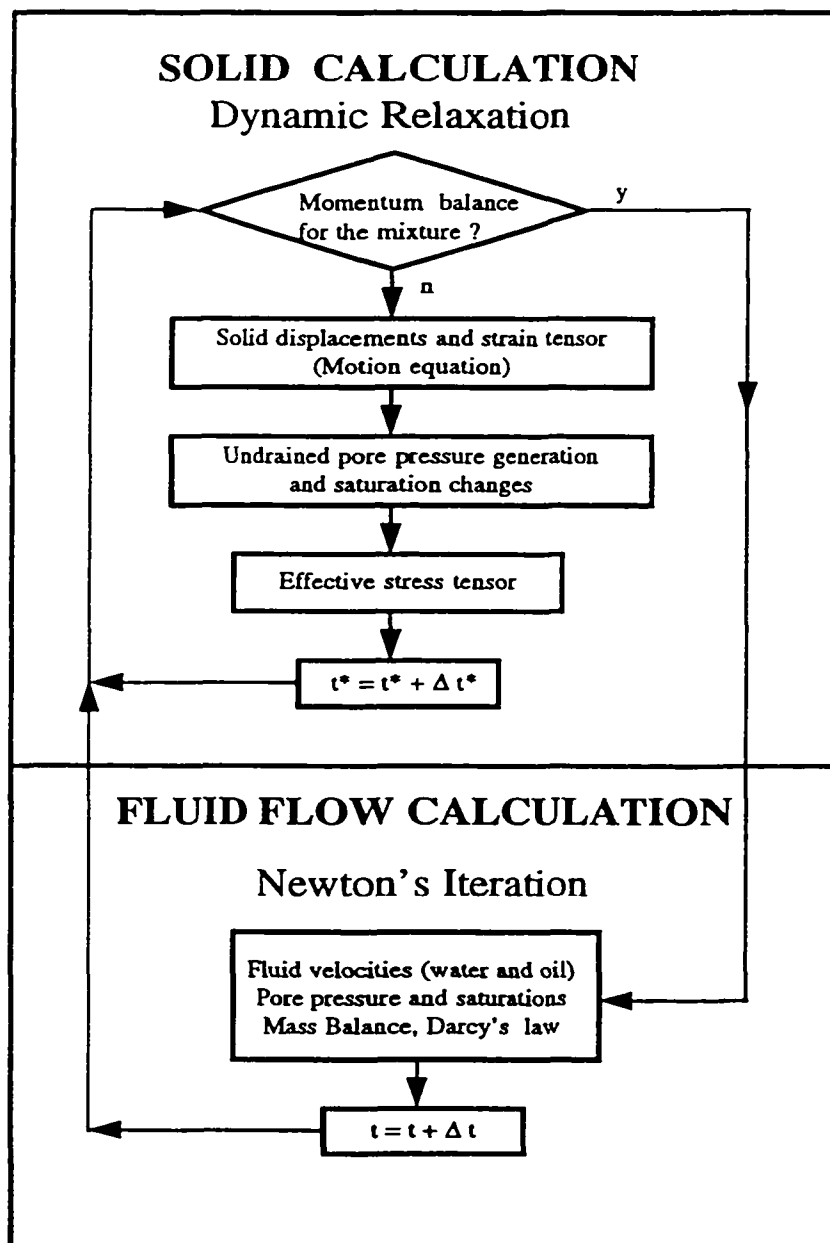
78

Figure 5.1: Schematic representation of the overall calculation process.

into equilibrium during each real time step.

This procedure accomodates the fact that mechanical effects occur almost instantaneosly (order of milliseconds), while fluid flow and dissipation of pore pressure are long term processes that can last minutes, days, weeks, or even years. Though rocks exhibiting creep or viscous (time-dependent) behavior are not considered here, the explicit finite difference technique can be used to account for these effects [25].

5.2 Mechanical calculation for the two-phase flow-deforming system

For the mechanical portion, the equation of motion for the *mixture* (Equation 4.60) is solved, using the dynamic relaxation procedure.

Several changes from the purely solid formulation are introduced in the mechanical calculation when the presence of pore fluids is considered. The constitutive equation is applied to yield the change in effective stresses because the strain rate controls the effective stress rate. However, the motion equation is applied to balance the total stresses.

Secondly, it is necessary to assume that the fluid saturated solid exhibits a more stiff response under a given loading condition that would the dry porous solid (in some codes, an apparent bulk modulus is used in order to consider this enhanced stiffness [25]). This effect is included directly in the program developed here by considering the effective stress changes and

80

the incremental pore pressure generation during the mechanical pseudo time step, thus eliminating the need for an apparent bulk modulus.

5.2.1 Undrained pore pressure generation during the mechanical portion

From Equation 4.51, it can be seen that pore pressure changes have a component related to the volumetric strain rate of the *solid* (first term) and another component related to the *flow of fluids* (second term). In fact, the second term in Equation 4.51 contains all factors associated with fluid flow: divergence of the fluids' velocities and gradients of pressure and saturation. This allows the pore pressure effects to be separated accordingly. The numerical procedure used to solve the equations takes advantage of this situation by including the component related to the volumetric strain of the solid as part the mechanical calculation, and the fluid flow component as part of the flow calculations.

Pore pressure generation under undrained conditions is controlled only by the first term in Equation 4.51, since the quantity P_{wf} equals zero during the mechanical portion (because of undrained conditions). The first term in Equation 4.51 in incremental form is:

$$\Delta P_{wu} = f_p u_{i,i} \Delta t^*. \tag{5.1}$$

The mechanical, pseudo time step is denoted here by using an asterisk.

Pore pressure accumulates during the sequence of mechanical pseudo time

81

steps needed to ahieve equilibrium at a particular real time step such that at the end there is a value of total pore pressure, P_{wu}, given by:

$$P_{wu} = P_w^n + \sum_{\Delta t^*} \Delta P_{wu} \qquad (5.2)$$

where P_w^n is the pore pressure from the previous *real* time step.

Note that, in this formulation, pore pressure generation is incremental (dependent on strain rate) as opposed to the classical poroelasticity formulation (Cleary [21], Detournay and Cheng [31]) in which pore pressure is dependent on strain.

The total stresses are calculated using Equation 4.4, which in incremental form reads:

$$\Delta \sigma_{ij} = (\Delta \sigma_{ij}' - \Delta P_{wu} \delta_{ij}) \Delta t^* \qquad (5.3)$$

The motion equation is invoked again and some of the energy of the system is damped away (dynamic relaxation procedure). Further strains are produced and higher pore pressure as well, until the system reaches equilibrium. This is the end of the first set of mechanical pseudo time steps and the program proceeds with the fluid portion of the corresponding time step.

5.2.2   Modified density scaling

Damping here is the same as in the pure solid calculations. However, the density scaling (see Section 3.13) has been changed to reflect the presence of pore fluid. The density scaling also will need to be adjusted when different constitutive equations are used.

82

The normal stress component in the x-direction, σ_{11}, is calculated as:

$$\sigma_{11} = (K - \frac{2}{3}G)(e_{11} + e_{22}) + 2Ge_{11} - \alpha P_{wu} \quad , \tag{5.4}$$

where $P_{wu} = f_p(e_{11} + e_{22})$. The factor f_p has already been defined in Equation 4.55. Recall that $u_{i,i} = u_{1,1} + u_{2,2} = e_{11} + e_{22}$. Therefore.

$$\sigma_{11} = (K - \frac{2}{3}G)(e_{11} + e_{22}) + 2Ge_{11} - \alpha f_p(e_{11} + e_{22}) \tag{5.5}$$

The speed of the dilatational wave in the x-direction is again estimated as:

$$C_p^2 = \frac{1}{\rho}\frac{\partial \sigma_{11}}{\partial e_{11}} \tag{5.6}$$

and, hence,

$$C_p = \sqrt{\frac{K + \frac{4}{3}G}{\rho} - \alpha f_p} \tag{5.7}$$

5.2.3 Undrained change of saturation

As with pore pressure calculations, changes in saturation have been separated into those related to the solid volumetric strain under undrained conditions and those associated with fluid flow.

The deformation of the solid can cause a change in saturation because of the eventual difference in the compressibilities of the fluids (wetting and non-wetting). The following expression (first term in Equation 4.52) is used to determine the change in saturation during the mechanical portion of the calculation:

$$\Delta S_{wu} = \alpha \dot{u}_{i,i}\frac{S_n S_w(C_{n1} - C_{w1})}{D_s}\Delta t^*. \tag{5.8}$$

83

Recall that the constants C_{n1} and C_{w1} are given by:

$$C_{w1} = \left[\frac{(\alpha - \phi)}{K_s} + \frac{\phi}{K_w} \right] \text{ and } C_{n1} = \left[\frac{(\alpha - \phi)}{K_s} + \frac{\phi}{K_n} \right],$$

and note that if the compressibilities of the fluids ($1/K_w$ and $1/K_n$) are equal, then C_{n1} equals C_{w1} and there will be no change in saturation induced by the solid volumetric strain during the undrained calculation.

As with the undrained pore pressure change, S_{wu} is the cumulative value of saturation obtained during the mechanical portion, considering the saturation from the previous real time step, S_w^n, i.e.

$$S_{wu} = S_w^n + \sum_{t^*} \Delta S_{wu}, \tag{5.9}$$

where ΔS_{wu} has been defined in Equation 5.8.

5.2.4   Convergence of mechanical calculations

The criterion to stop the sequence of mechanical steps is based on the relative value of the out-of-balance forces in the system. A value of maximum out-of-balance force is prescribed such that when a given value is achieved, the mechanical calculation is stopped, eventhough the fluid flow portion of calculation continues for the time step. This permissible out-of-balance force can be about three orders of magnitude smaller than the out-of-balance force obtained for the first real time step, or it can be changed to be less restrictive in order to speed up convergence and reduce the number of pseudo time steps needed for equilibrium. The accuracy of the calculation sought will ultimately dictate the tolerance.

The stoping criterion can be changed as real time progresses. If the external forces, or boundary conditions, are constant in time, the most critical situation, in terms of balance of forces, will be at the first timestep, at which the boundary conditions are applied. Once this initial situation is balanced, then the system will be put out of balance by the fluid flow and a different value of permissible out-of-balance force may be used.

This is the last step in the sequence of calculations for the mechanical portion of the code (Figure 5.2).

5.3   Numerical solution for the fluid flow

The flow equations were formulated to yield two fundamental unknowns: the water saturation and the water pressure. All other quantities are calculated from these. The flow equations are solved at the element level (quadrilaterals). Pore pressure and saturations are considered element centered variables (Figure 5.3). The fluid velocity divergence is element-centered, as well. However, fluid velocities, w_i and v_i, together with pressure and saturation gradients are node-centered quantities. To convert node-centered quantities to element-centered values, an average of the values over the four nodes belonging to the element is taken and assigned to the element. Recall that the pore pressure calculated during the mechanical portion of the code is associated with triangles. However, for the fluid flow portion, pore pressure is associated with quadrilaterals elements. Therefore, an average value of the pore
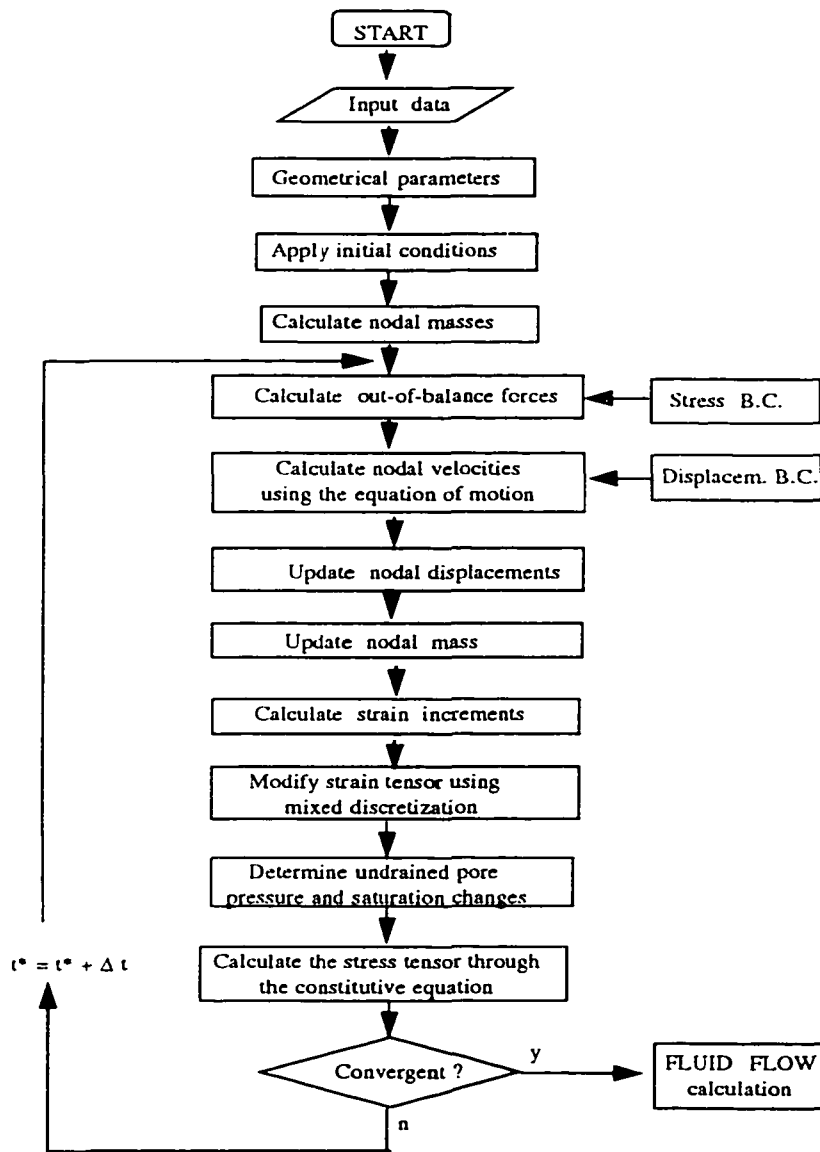
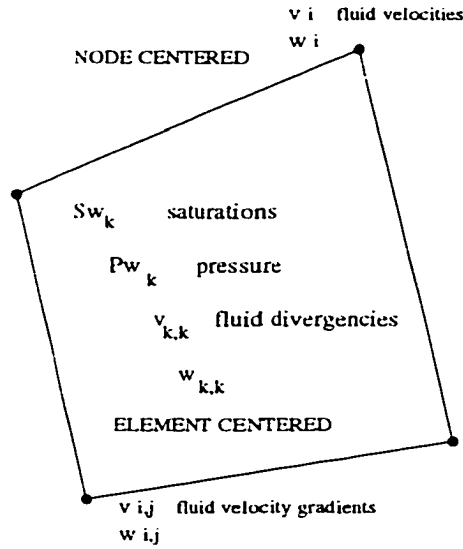85

Figure 5.2: Steps for the mechanical calculation.

Figure 5.3: Definition of variables for the fluid flow calculation.

pressure corresponding to the two sets of overlapping triangles included in a quadrilateral is assigned to the element. The same holds for the saturation.

5.3.1 Solution variables and summary of flow equations

To solve for water pressures and saturations, the fluid flow equations, Eqs. 4.51 and (refeq:mcsw, are restated as:

$$P_w = P_{wu} + P_{wf}\Delta t \tag{5.10}$$

$$S_w = S_{wu} + S_{wf}\Delta t \tag{5.11}$$

The terms P_{wu} and S_{wu} are known at the end of the mechanical calculation and represent the cumulative values given by Equations 5.2 and 5.9,

87

respectively. The terms P_{wf} and S_{wf} are obtained from Equations 4.51 and 4.52.

The Darcy equations for the fluids are rewritten as:

$$w_i = \Lambda_{w_{ij}}(-p_{w,j} + \rho_w b_j) \tag{5.12}$$

$$v_i = \Lambda_{n_{ij}}(-p_{n,j} + \rho_n b_j). \tag{5.13}$$

Note that the difference with respect to Equations 4.64 and 4.65 is that the terms depending on accelerations of the solid have been eliminated. This is due to the fact that the body is brought to equilibrium through the dynamic relaxation procedure after each real time step, so that accelerations of the solid are practically zero after the mechanical portion for each real time step has been completed.

Before explaining in detail the procedure of calculating the variables involved, the boundary conditions for different flow situations must be explained. Stresses and velocity (or displacement) restrictions for the solid at the boundaries are set in the same manner as was discussed in Chapter 3.

5.3.2   Boundary conditions

Pore pressure boundary conditions.

Two conditions at the boundaries can generally be found: a) no flow or b) flow boundary conditions with specified pore pressure values. A no-flow boundary condition is imposed by setting the pressure gradient in the direction normal to the boundary equal to zero and also the velocity of the

88

fluids take a zero value in a direction normal to the boundary. In the case of no-flow boundary conditions, pore pressure at boundary points is unknown and needs to be solved for.

To set a free flow boundary condition with a prescribed value of pore pressure a *phantom mesh* is built outside the boundary (Figure 5.4). Values of pore pressure corresponding to the phantom elements are set to zero or are equal to a prescribed quantity. The pressure gradients at the boundaries are calculated using these phantom elements by the same procedure used for internal elements [51]. Where pore pressure in the boundary is specified, saturation is free to change since flow is permited.

Saturation boundary conditions

The only circumstance under which a boundary condition is forced for saturation is when fluids are injected with a particular volumetric concentration at the boundary. In this case the corresponding saturation is applied to the boundary nodes. Saturations are zone-centered variables, but for a grid-point an average from the surrounding elements is assigned. This does not introduce additional errors since the system of coupled equations is solved for the center point of the zones and the dependent variables P_w and S_w are considered piecewise constants (constants inside the element).

For the calculation of the saturation gradients in case of a no-flow boundary, the saturations of the *phantom* elements at the boundary are set to the same saturations of the equivalent elements in the mesh.
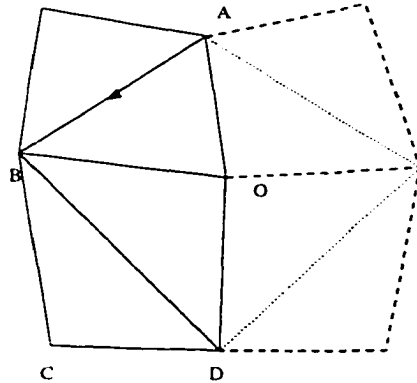
89

Figure 5.4: Phantom mesh to apply boundary conditions

5.3.3 Nonlinearities and time approximations

The set of equations to be solved is nonlinear, since the coefficients and mobilities are functions of the unknowns (P_w and S_w). If the simple method of linearization based on *lagging coefficients* is used, all variables will be evaluated at the previous time step and the solution will be explicit. However, the time step needed for stability of the scheme is usually too small to be used practical calculations. Implicit time approximations are preferred. This means that coefficients and mobilities are evaluated at an advanced time (same time step as used for the fundamental unknowns).

There are many solution methods and formulation options to solve the

flow equations (see Mattax and Dalton [72] for an extensive review). Actually, there are recommended methods for particular modelling situations. However, since the emphasis of this dissertation is not on numerical solutions of fluid flow, but rather in the coupling with the porous solid deformation, a simple method which can provide reasonable accuracy and reliability was chosen.

The simplest implicit procedure to solve this set of nonlinear equations is simple iteration. For this purpose, Equations 5.10 and 5.11 are discretized in time as:

$$
\begin{aligned}
P_w^{(\nu)} &= P_{wu}^{(n)} + \left(P_{wf}\right)^{(\nu-1)} \Delta t \\
S_w^{(\nu)} &= S_{wu}^{(n)} + \left(S_{wf}\right)^{(\nu-1)} \Delta t
\end{aligned}
\tag{5.14}
$$

The superscript n indicates the real time step level and ν the iteration step. The iterations are done in a staggered manner starting with saturation, then continuing with pressure, and finally passing to the next iteration. A convergence tolerance is set, and iterations are peformed until the desired tolerance is achieved. At this point, the calculation is advanced in time. It has been found that generally, this staggered solution scheme for coupled equations is conditionally stable [64]. The small stable time step is a limiting condition in terms of computation time.

A more powerful implicit iterative technique, also tried in this dissertation, is the Newton-Raphson method. This method is suitable to solve strongly nonlinear equations. To apply Newton's iterations, the nonlinear

91

set of equations is written as:

$$P_w^{(n+1)} = P_{wu}^{(n)} + \left(P_{wf}\right)^{(n+1)} \Delta t \tag{5.15}$$

$$S_w^{(n+1)} = S_{wu}^{(n)} + \left(S_{wf}\right)^{(n+1)} \Delta t \tag{5.16}$$

or, in residual form:

$$P_w^{(n+1)} - P_{wu}^{(n)} - \left(P_{wf}\right)^{(n+1)} \Delta t = 0 \tag{5.17}$$

$$S_w^{(n+1)} - S_{wu}^{(n)} - \left(S_{wf}\right)^{(n+1)} \Delta t = 0 \tag{5.18}$$

Denoting the left-hand side of the above equations as functions f and g, this can be rewritten as:

$$f(P_w^{(n+1)}, S_w^{(n+1)}) = f^{(n+1)} = 0$$
$$g(P_w^{(n+1)}, S_w^{(n+1)}) = g^{(n+1)} = 0, \tag{5.19}$$

which can be combined to yield a function F containing both variables, now identified with a vector $\mathbf{x}$, as:

$$\mathbf{F(x)} = 0 \tag{5.20}$$

That is, half of the elements of vector $\mathbf{x}$ are the unknown values of P_w and the other half correspond to the unknown saturations. The Newton iteration step for the set of equations is:

$$\mathbf{x}_{new} = \mathbf{x}_{old} + \delta \mathbf{x} \tag{5.21}$$

92

where

$$\delta \mathbf{x} = -\mathbf{J}^{-1} \cdot \mathbf{F} \tag{5.22}$$

The matrix $\mathbf{J}$ is the Jacobian of the system. The routine used for solving the system of nonlinear equations comes from Press et al. [89] and is based on a globally convergent method for nonlinear equations.

5.3.4 Mobilities and calculation of fluid velocities

The fluid velocities are given by Equations 5.12 and 5.13, which are the generalized Darcy equations. The fluid velocities are calculated at the grid-points, so the finite difference contour operator, given by Equations 3.22 and 3.23, is applied to the Darcy equations. For the wetting fluid velocity (ignoring gravity) the expression is:

$$w_i = \frac{1}{2A} \sum_N (-\lambda_{w_{ij}} P_w)^N n_j^N L^N \tag{5.23}$$

where N is again the side of the summation path depicted in Figure 3.4. The components of the wetting fluid velocity are (taking indices i, j to be 1, 2 instead of x, y):

$$w_1 = -\frac{1}{2A} \sum_N [(\lambda_{w_{11}} P_w)^N n_1 L^N + (\lambda_{w_{12}} P_w)^N n_2^N L^N] \tag{5.24}$$

$$w_2 = -\frac{1}{2A} \sum_N [(\lambda_{w_{21}} P_w)^N n_1 L^N + (\lambda_{w_{22}} P_w)^N n_2^N L^N] \tag{5.25}$$

For instance, the contribution to the velocity of the wetting fluid for the gridpoint O, in the x-direction, supplied by the element labeled by $N = 1$ in

93

Figure 3.4 is:

$$w_1^{(N=1)} = -\frac{1}{2A}[-\lambda_{w_{11}}P_w^{(N=1)}(y_A - y_D) + \lambda_{w_{12}}P_w^{(N=1)}(x_A - x_D)]. \qquad (5.26)$$

In the y-direction the approximation is given by:

$$w_2^{(N=1)} = -\frac{1}{2A}[-\lambda_{w_{21}}P_w^{(N=1)}(y_A - y_D) + \lambda_{w_{22}}P_w^{(N=1)}(x_A - x_D)] \qquad (5.27)$$

Similar expressions can also be written for the remaining surrounding elements. The total velocity components are obtained by adding the corresponding terms from Equations 5.24 and 5.25. The non-wetting fluid velocity components are obtained in the same manner.

The mobilities $\lambda_{w_{ij}}$ or $\lambda_{n_{ij}}$ are given by Equations 4.63 and 4.66, i.e. for $\lambda_{w_{11}}$ the expression is:

$$\lambda_{w_{11}} = k_{w_{11}}\frac{k_{rw}(S_w)}{\nu_w(P_w)}. \qquad (5.28)$$

The relative permeability values (k_{rn} and k_{rw}) are determined from the relative permeability vs. saturation curves that are experimentally obtained. Either a function or a table of data points can be the input to the program. When relative permeability is given explicitly as a function of saturation, the former is simply evaluated for the particular value of saturation. When a set of data points is provided, a cubic spline is used to interpolate and determine values for the particular saturation required. Note that for values of saturation smaller than $S_{w(irr)}$ or greater than $(1 - S_{or})$, the relative permeability is taken to be $S_{w(irr)}$ and $(1 - S_{or})$, respectively. The absolute

94

permeability tensor and viscosity ratio (hydraulic conductivity) are given as input parameters for each zone.

The averaging, or weighting, of mobilities is a complex problem in reservoir simulation when finite difference methods are used. Five- or nine-point difference operators are commonly used to calculate the mobility coefficients [72]. Assumptions such as taking the upstream value of mobility are used because mobility at the interface of two different *elements* is required. In the approach used here, there is no need for mobility weighting since the contour operator considers directly the contribution of surrounding elements to the velocity of the fluid (mobility times pressure gradient), as expressed by Equations 5.24 and 5.25 and Figure 3.4.

If desired, heterogeneous values can be assigned to permeability parameters for different zones, simulating layers, lenses or random properties. Moreover, permeability anisotropy can be handled by substituting in the corresponding anisotropic permeability tensor.

Since the mass conservation equations are solved for the elements, the fluid velocities are converted from node-centered to zone-centered quantities by taking the arithmetic average over the gridpoint values that define an element.
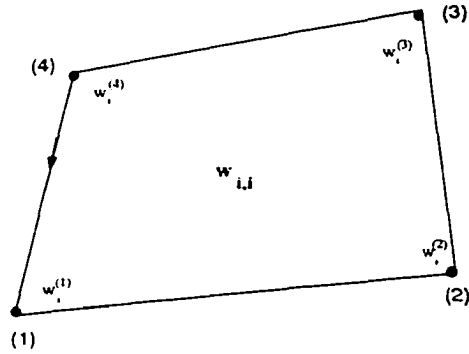
Figure 5.5: Integration path for a quadrilateral.

5.3.5 Divergence of fluid velocities

The divergence of fluid velocities, $w_{i,i}$ and $v_{i,i}$,

$$w_{i,i} = w_{1,1} + w_{2,2} \text{ and } v_{i,i} = v_{1,1} + v_{2,2} \tag{5.29}$$

are approximated by applying the countour operator given by Equation 3.14 to each quadrilateral element (refering to Figure 3.1, M=4). The summation path is shown in Figure 5.5. The velocities are known at the gridpoints, and a linear interpolation is assumed along the edges so, for example, the x-component, $w_{1,1}$, is given by:

$$w_{1,1} = \frac{1}{2A}\left[(y^{(2)} - y^{(4)})(w_1^{(1)} - w_1^{(3)}) - (y^{(1)} - y^{(3)})(w_1^{(2)} - w_1^{(4)})\right]. \tag{5.30}$$

The gridpoints are denoted by the corresponding number between parentheses, and A is the area of quadrilateral 1234, which is:

$$A = \frac{1}{2}\left[(y^{(2)} - y^{(4)})(x^{(1)} - x^{(3)}) - (y^{(1)} - y^{(3)})(x^{(2)} - x^{(4)})\right] \qquad (5.31)$$

For the y-component the approximation results in:

$$w_{2,2} = \frac{1}{2A}\left[(x^{(2)} - x^{(4)})(w_2^{(3)} - w_2^{(1)}) + (x^{(1)} - x^{(3)})(w_2^{(2)} - w_2^{(4)})\right] \qquad (5.32)$$

Similar expressions can be written for the divergence of the non-wetting fluid velocity. Note that the fluid divergences are obtained as element centered quantities, and can be entered directly into the fluid flow equations.

The sequence of steps followed in the fluid flow portion of the program is depicted in Figure 5.6.

5.4 Automatic time stepping for the fully-implicit calculation

Even though the fully-implicit formulation for the flow equations is unconditionally stable, accuracy could be in question if the time step is chosen too large. This is particularly important at early times when fluid velocity gradients are large. If time steps are too small at the beggining instabilities will develop. This consequence is also present in finite element codes [130] and has to do with the error introduced in time derivatives when time steps are very small.

97
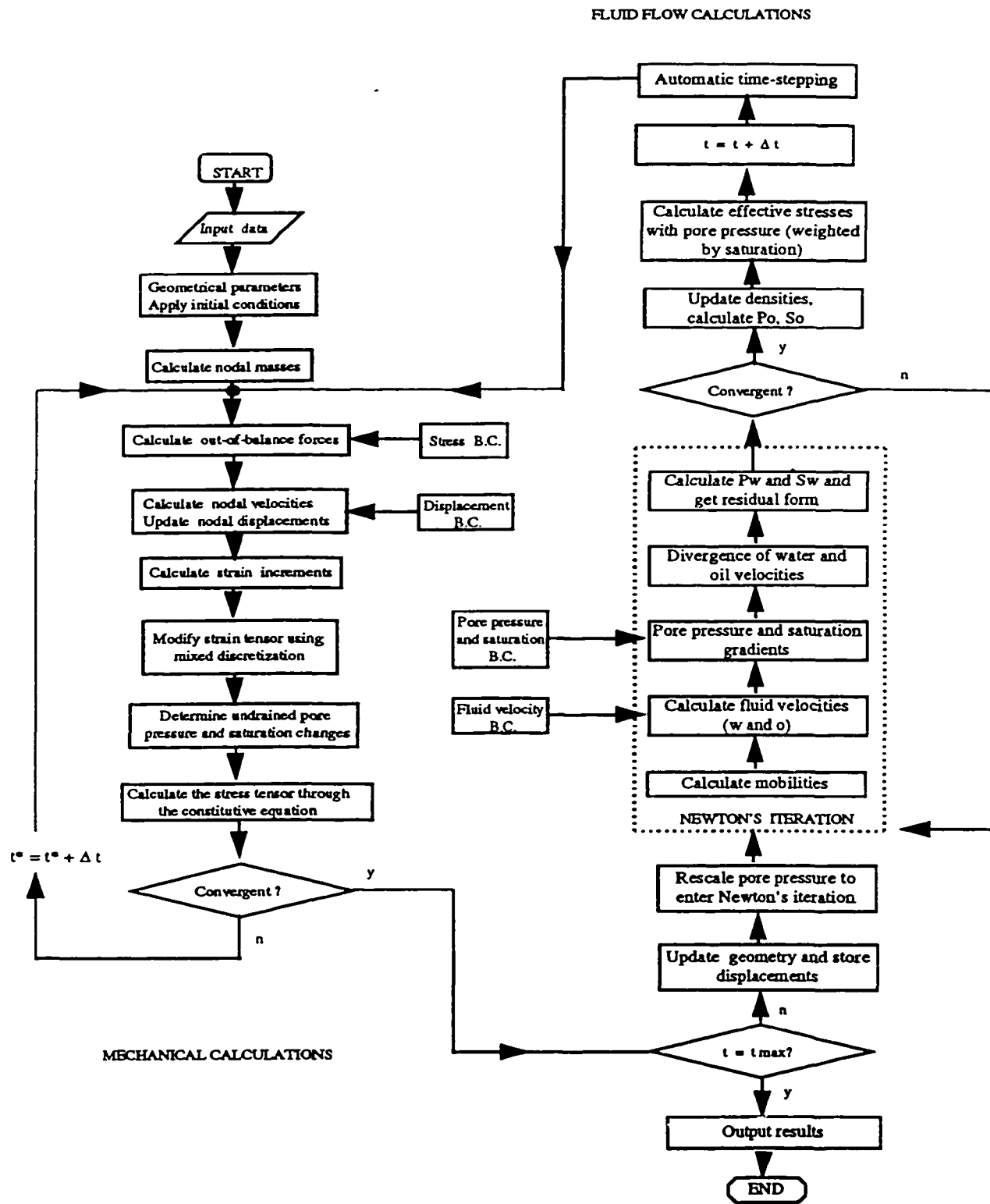
Figure 5.6: Flow chart for the fluid flow portion.

An automatic time-stepping routine for the fully-implicit calculation has been implemented. This consists of changing the time step to maintain a prescribed pressure drop estimated to be about $5 - 10\%$ of the initial (first real time step) pore pressure increment. The prescribed pressure drop parameter can affect the accuracy of the calculation because it controls the size of the time step. This pressure drop can be changed during the real time process, such that it can be smaller in early times and larger as time progresses.

Also a time step limit has been established for which there is a switch between fully implicit and simple staggered iteration type of calculations. If the time step is small, staggered iteration results are more efficient than are fully implicit calculaitons. However, fully implicit methods are preferred for larger time steps. This switching procedure is automatic but the limit time step needs to be set by the user. A trial run can be made to adjust this parameter by comparing the time needed per time step for a fully implicit vs. a simple iteration calculation. Adjusting this parameter will greatly affect the total run time for a given problem.

5.5   Verification tests

5.5.1   One-dimensional consolidation problem, single-phase flow

A one-dimensional consolidation problem (Terzaghi's) has been chosen to check the code. The analytical solution for this problem is presented below.

99

Analytical solution.

One-dimensional consolidation problems are characterized by only one non-zero normal strain and field quantities varying only in that direction (uniaxial strain conditions). If e_{xx} is a non-zero strain, then the poroelasticity governing equations are given by (Detournay and Cheng [31]):

$$\sigma_{xx} = \frac{2G(1-\nu)}{1-2\nu}e_{xx} - \alpha p \qquad (5.33)$$

$$\sigma_{yy} = \sigma_{zz} = \frac{\nu}{(1-\nu)}\sigma_{xx} \qquad (5.34)$$

with p being the coupling parameters in the poroelasticity equations.

Under undrained conditions, pore pressure is proportional to σ_{xx}, i.e.,

$$p_u = -\frac{B(1+\nu_u)}{3(1-2\nu_u)}\sigma_{xx}. \qquad (5.35)$$

This equation gives the initial pore pressure increment under undrained conditions [31]. By expressing e_{xx} in terms of p and σ_{xx}, and using Equation 5.33, the diffusion equation for the pore pressure is obtained as:

$$\frac{\partial p}{\partial t} - c\frac{\partial^2 p}{\partial x^2} = \frac{\partial \sigma_{xx}}{\partial t}. \qquad (5.36)$$

This differential equation must be solved together with the following boundary conditions:

$$
\begin{aligned}
p &= 0 \text{ at H=0} \\
\frac{\partial p}{\partial x} &= 0 \text{ at H=L and also at y=0, y=W.}
\end{aligned} \qquad (5.37)
$$

100

The initial condition is that the pore pressure equals the undrained pore pressure increment at the time $t = 0^+$, which corresponds to the time at which the load is first applied, and is given by Equation 5.35.

The equation is restated in terms of the following dimensionless variables:

$$X = \frac{x}{L}$$
$$T = \frac{ct}{4L^2}.$$
(5.38)

Hence, it becomes, for a constant axial load σ_{xx}:

$$\frac{\partial p}{\partial T} - \frac{\partial^2 p}{\partial X^2} = 0$$
(5.39)

The analytical solution for this equation is:

$$P(x, t) = P_u[1 - F(X, T)]$$
(5.40)

where

$$F(X, T) = 1 - \sum_{m=1,3,\dots}^{\infty} \frac{4}{m\pi} \sin(\frac{m\pi X}{2}) \exp(-m^2\pi^2 T).$$
(5.41)

Numerical solution

A water-saturated column with dimensions of 80x40 cm (Figure 5.7 is loaded axially. The column is free to drain only from the top surface, all other surfaces are no-flow (impermeable) boundaries. The axial stress σ_p is a step function applied instantaneously. There is no need for incremental loading to preserve stability of the code; full load is applied at the beginning. For this problem, σ_p has been set to $10 kPa$. Comparison with the analytical

101

$$\sigma_p = 10000 \ \text{N/m}^2$$

Free flow

E = 3.0e5 Pa

ν = 0.2

K_s = 1.e11 Pa

K_w = 1.e 6 Pa

ϕ = 0.32

K = 1.e-9
    m^4/N-sec
  = 1 D

No flow

Mechanical B.C.

Fluid flow B.C.
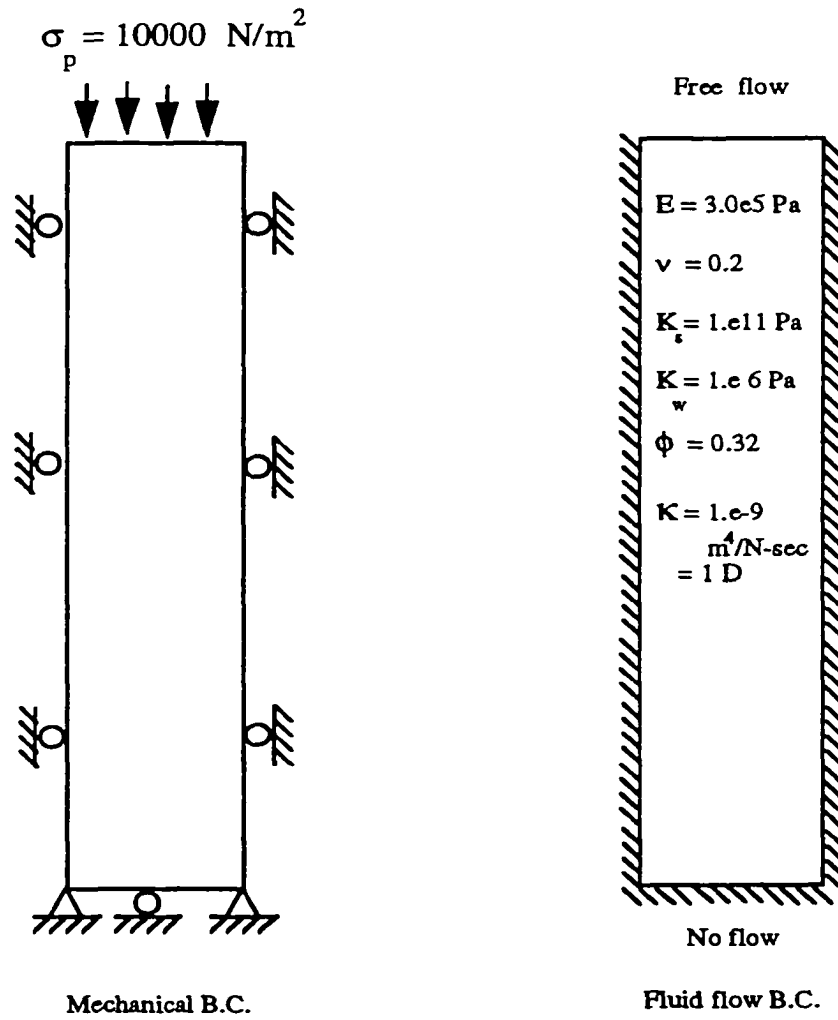
Figure 5.7: Soil column showing boundary conditions.

102

solution for excess pore pressure along the column height at different times is favorable (Figures 5.8 and 5.9). The evolution of excess pore pressure with time, considering three different points in the column, can be determined and excellent agreement is obtained (Figure 5.10). The evolution in time of the relative error for the pore pressure indicates an average relative error of about 2.5% (Figure 5.11). The peaks and discontinuities in the error are a consequence of the change in time step to conform to the tolerance prescribed in order to have a specified change in pore pressure(as described in Section 5.4). If smaller time steps (smaller pressure change tolerances) are taken, the results are enhanced but total time for the run is thereby increased. Errors increase with time because the time steps increase as well.

The settlements obtained from the numerical and analytical solutions are in good agreement (Figure 5.12).

Work softening, using a trilinear constitutive equation, has also been studied for the column problem geometry. The parameters used are indicated in Figure 5.13. Also a more rigid material is considered since a one order of magnitude higher Young's modulus is used. Note how the initial (undrained) increment of pore pressure is much less for the rigid material than for a softer, more deformable material, presented in the previous example. A comparison of the dissipation of excess pore pressure in time for a linear elastic constitutive equation vs. a trilinear constitutive equation fixing the rest of the parameters is plotted (Figure 5.14). In a material with work

103
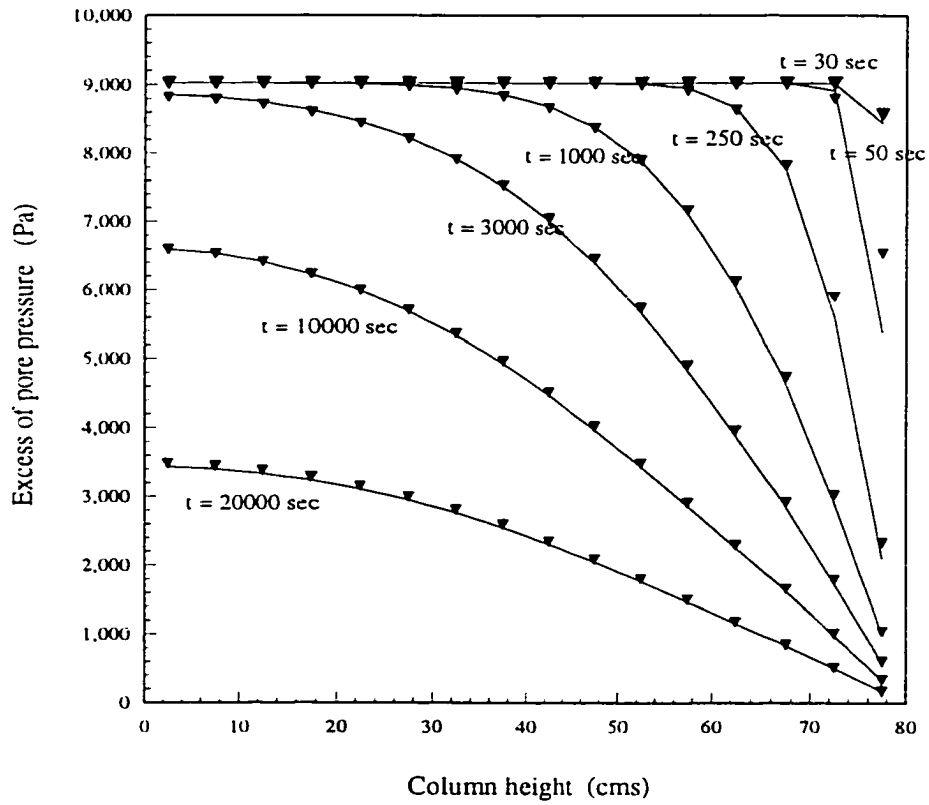
Figure 5.8: Analytical (lines) vs. numerical (dots) results for pore pressure dissipation in time along the height (y-coordinate) of the column (each curve belongs to the time indicated).
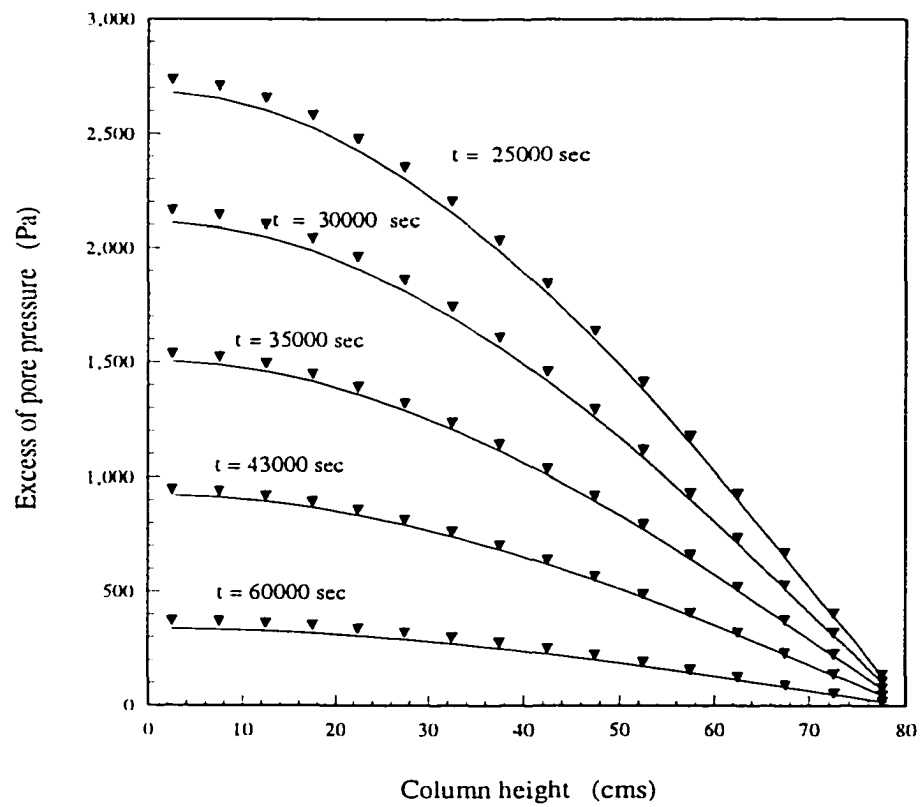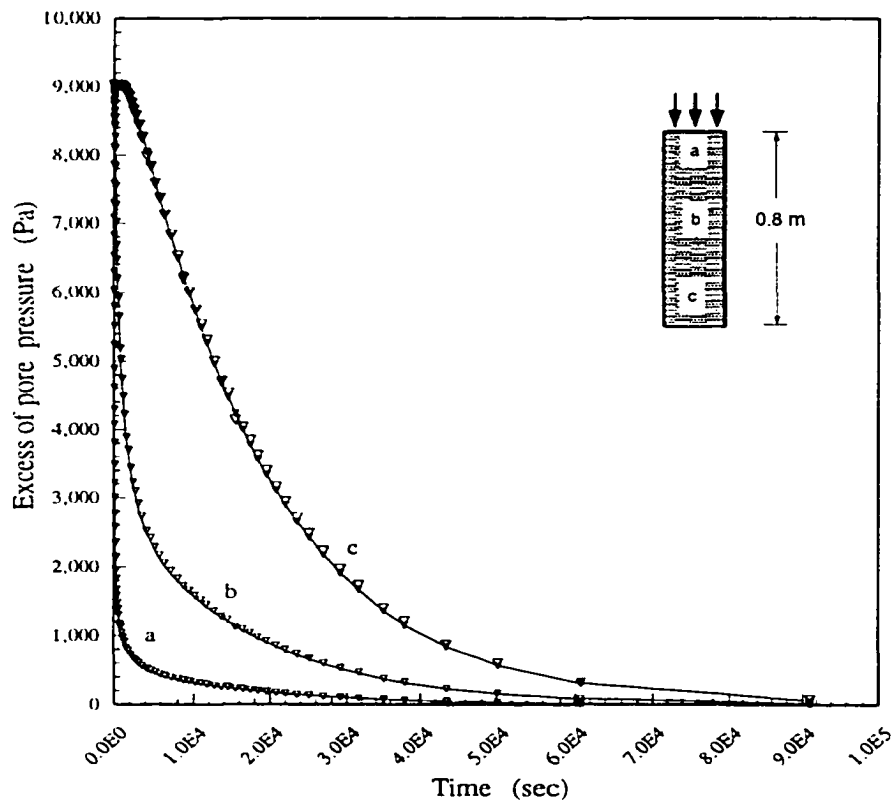
104

Figure 5.9: Analytical (lines) vs. numerical (dots) results for pore pressure dissipation in time along the height (y-coordinate) of the column (each curve belongs to the time indicated).

105

Figure 5.10: Dissipation of excess pore pressure in the column (one-phase) as a function of time. Comparison between analytical (full lines) and numerical (symbol) solution (each curve belongs to the point indicated at the column).

106
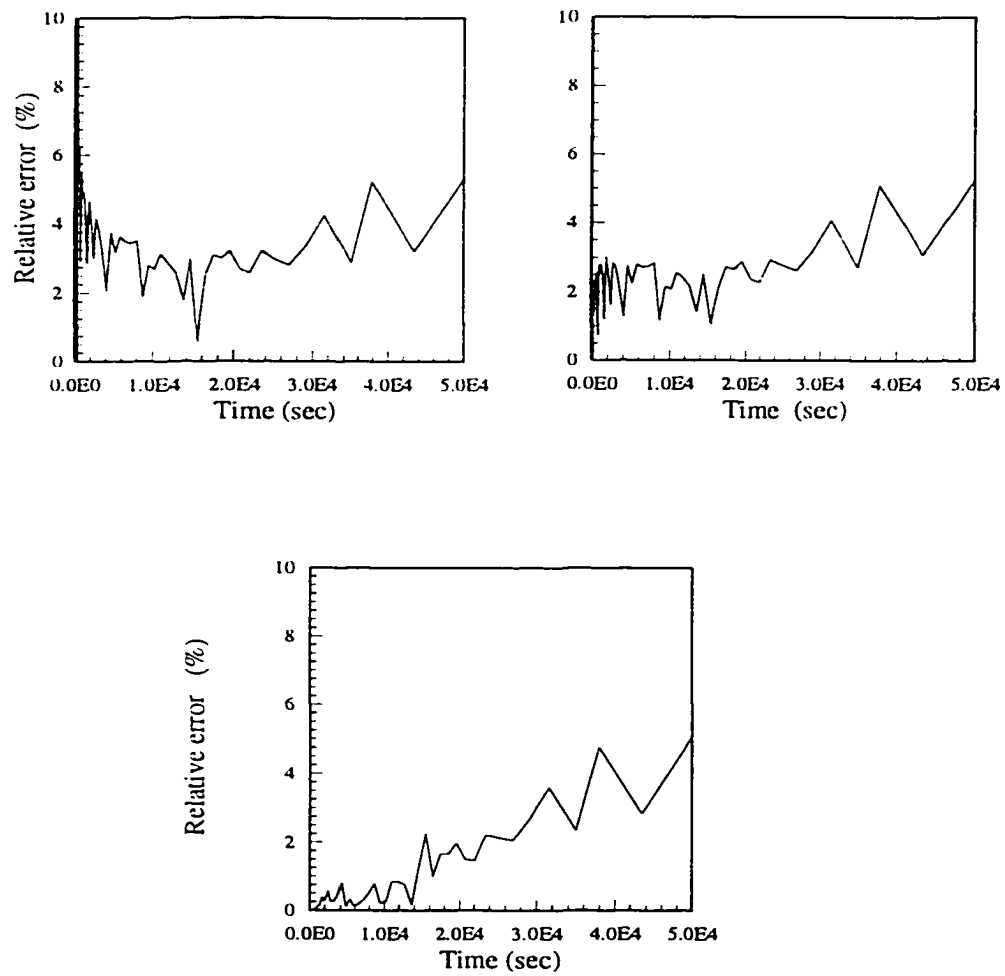
Figure 5.11: Evolution of pore pressure relative error with time for the one-dimensional (one-phase) consolidation problem.

107
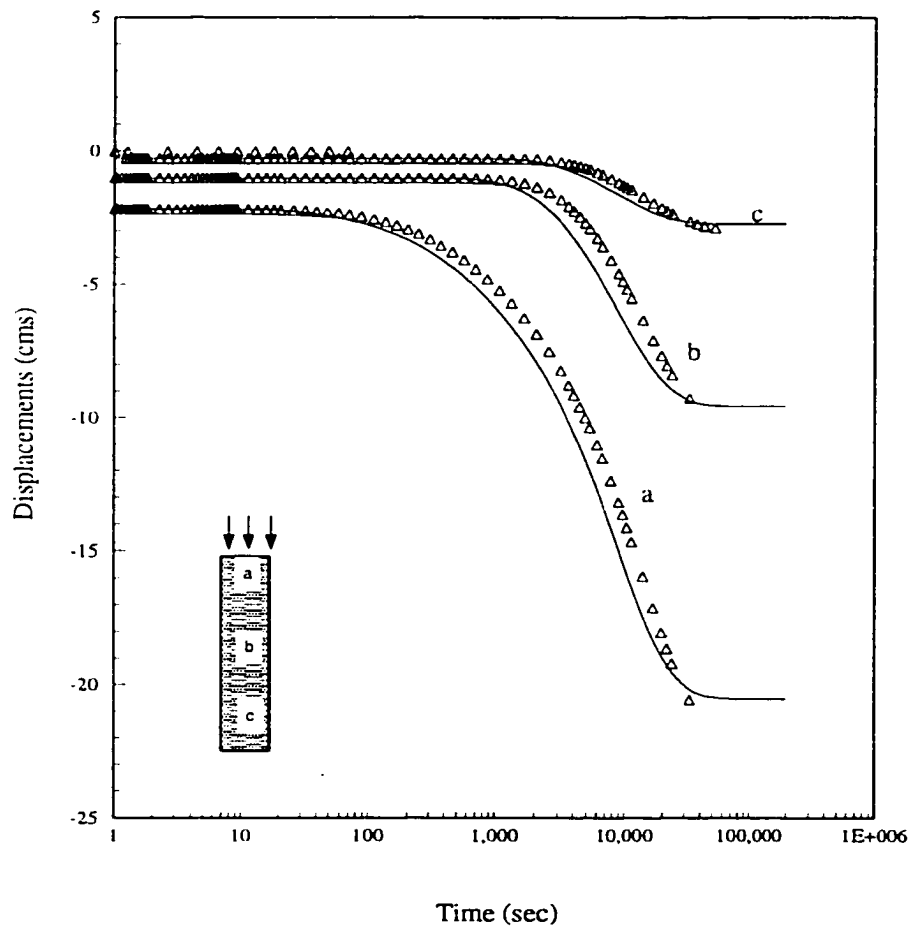
Figure 5.12: Analytical (lines) vs. numerical results (dots) for settlements in the column for the one-dimensional (one-phase) consolidation problem.

108

softening (trilinear constitutive equation), pore pressure is maintained longer because of compaction. That is, for a given time pore pressure is higher in the solid portion that is deforming more because it has entered the post-peak phase of the curve and as a consequence has lower deformation parameters (E and G). The dissipation of pore pressure in the linear material is much faster because the deformation of the solid, which is much less in this case, does not contribute as much to pore pressure maintenance.

Shear modulus changes with time in the column (Figure 5.15). The change in shear modulus for three particular points in the column as a function of time is also determined (Figure 5.16).

5.5.2 Porosity changes during coupled deformation and fluid flow

The porosity update during the coupled strain and flow through the porous medium has been determined at each real time step by solving Equation 4.57 in an explicit manner.

Expanding the material derivatives and regrouping in Equation 4.57 gives:

$$\frac{\partial \phi}{\partial t} + u + i \frac{\partial \phi}{\partial x_i} - \alpha A + \phi A = 0 \tag{5.42}$$

where

$$A = u_{i,i} + \frac{1}{K_s} \frac{\partial P_w}{\partial t} + u_i \frac{\partial P_w}{\partial x_i} \tag{5.43}$$

This equation is discretized in time as:

$$\frac{\phi^{n+1} - \phi^n}{\Delta t} = -\phi^n A^{n+1} - u_i^{n+1} \left(\frac{\partial \phi}{\partial x_i}\right)^n - u_i^{n+1} A^{n+1} \tag{5.44}$$
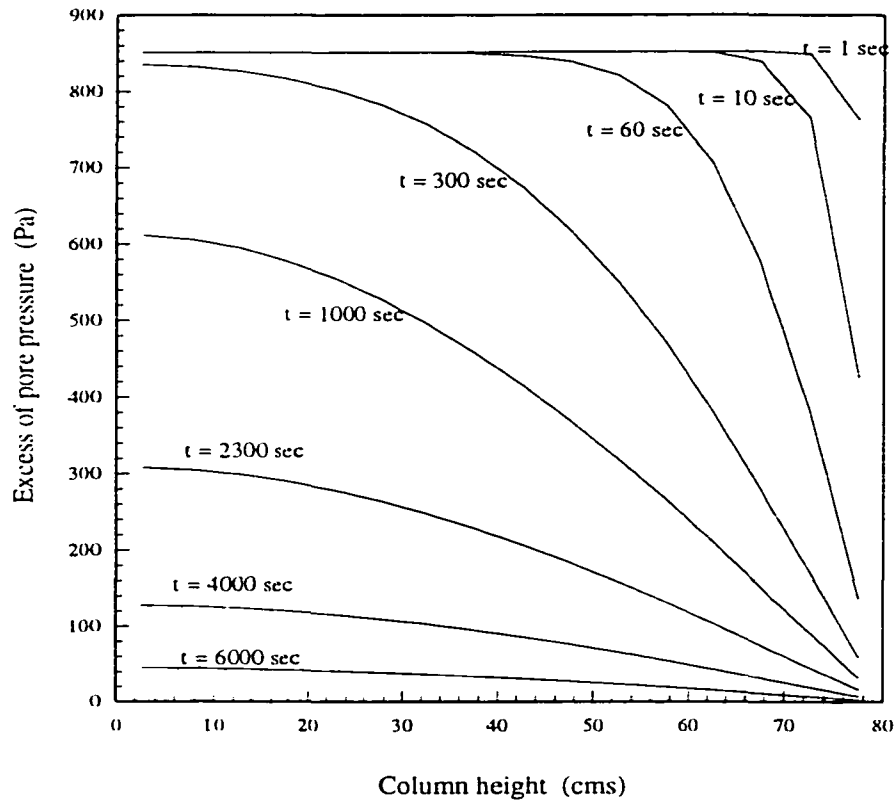
109

Figure 5.13: Excess of pore pressure in the column considering a trilinear constitutive equation (with softening behavior, time is indicated for each curve).
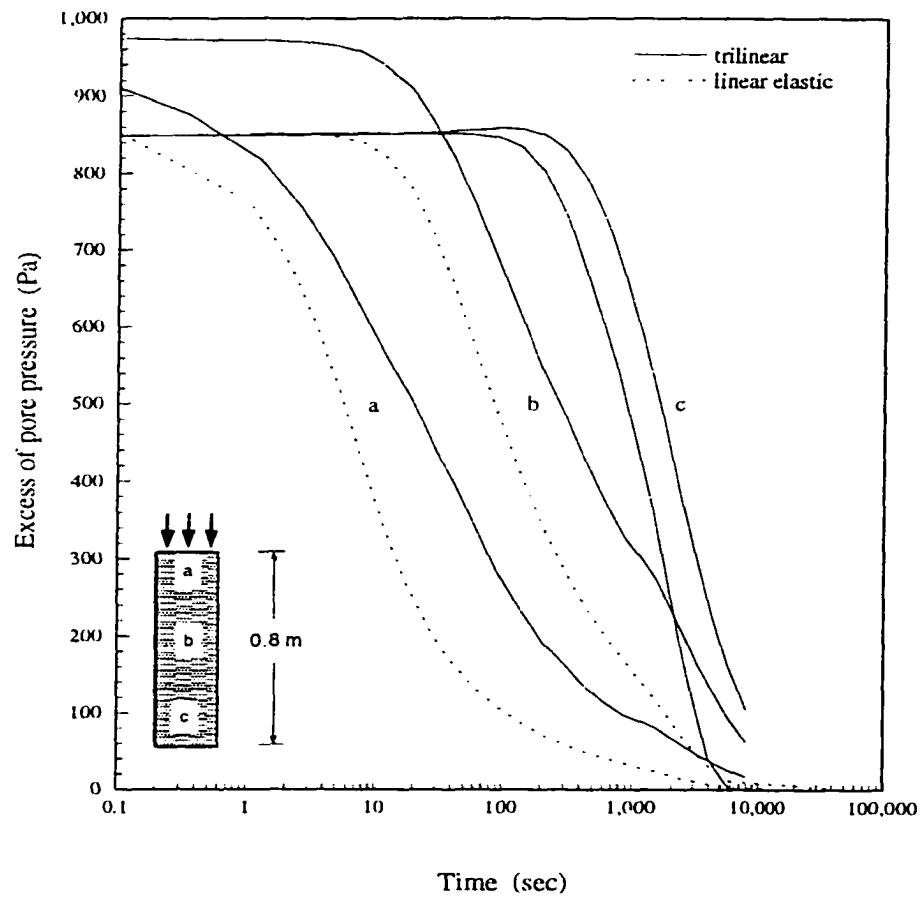
110

Figure 5.14: Comparison of excess pore pressure as a function of time for three points in the column (linear elastic vs. trilinear constitutive equation).
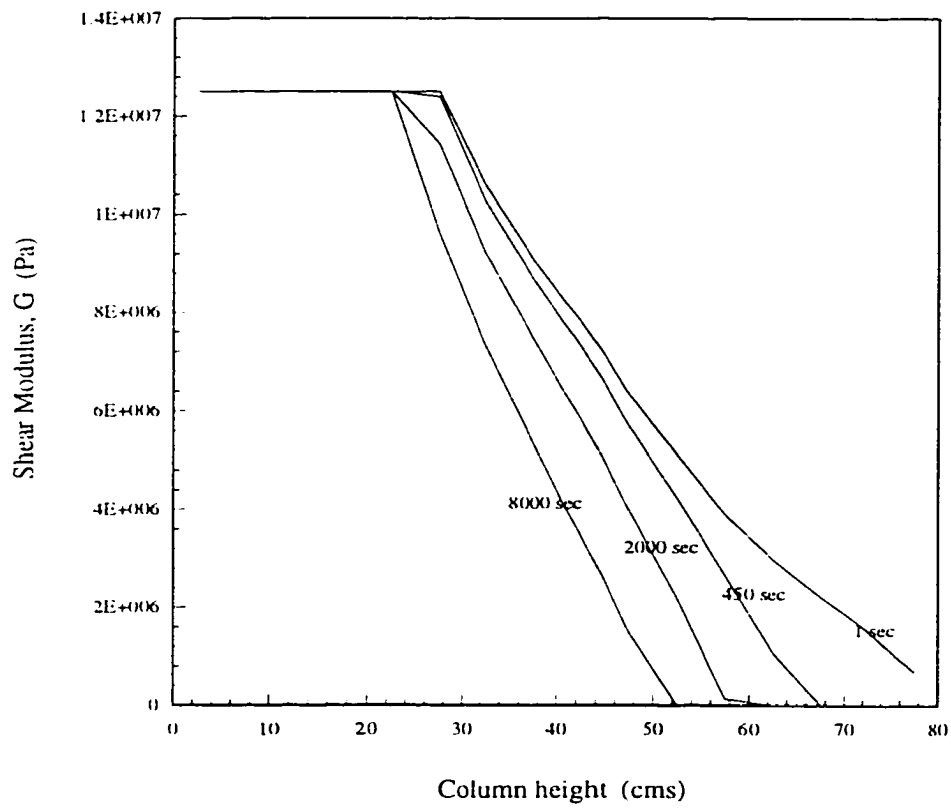
111

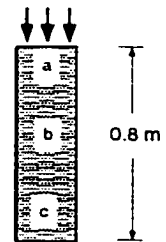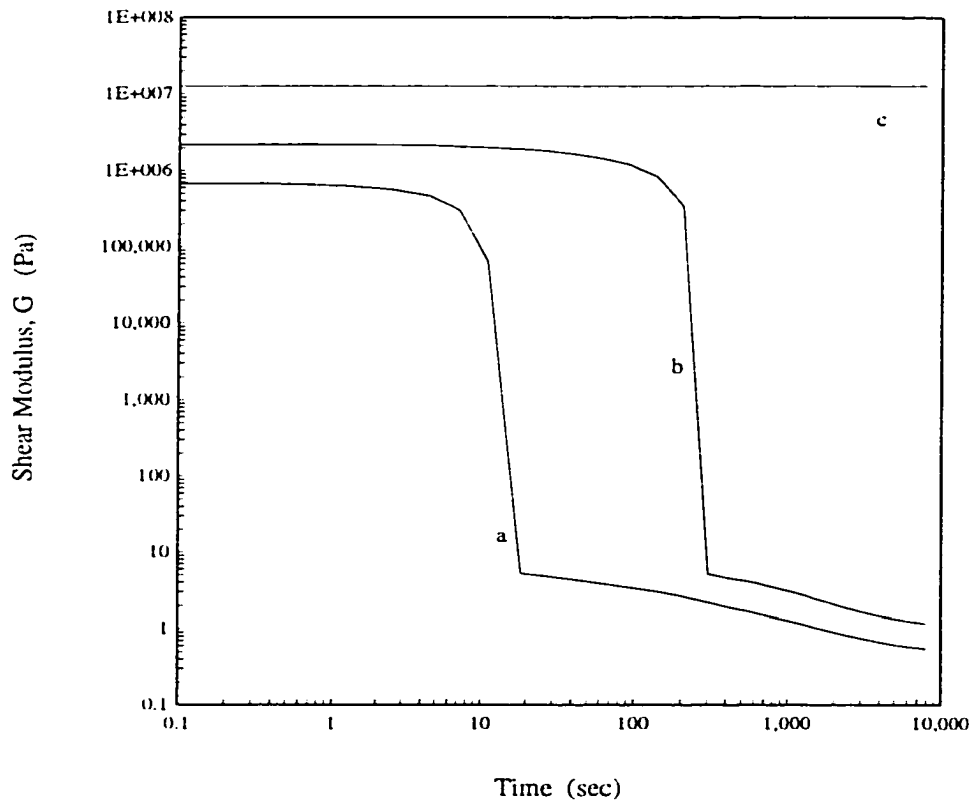Figure 5.15: Shear modulus degradation in the column for different time levels (indicated).

112

Figure 5.16: Shear modulus degradation as a function of time at three different points in the column (indicated).

All terms in A are known at the time $(n + 1)$, but the porosity gradient term is lagged to time n. The spatial derivatives are solved using the countour procedure (see Chapter 3).

The fact that the initial pore pressure is zero (i.e. the overpressure generated by the loading is added on to a base level that equals zero, rather than on to a hydrostatic profile) affects the porosity changes quantitatively. This is because there is a tendency in time to drain the column completely instead of dissipating the pore pressure generated in order to regain the hydrostatic equilibrium under the new loading conditions. In this case case some fluid volume will always remain to help support this load and porosity changes will have a limit different from zero. However, this calculation permits the effect of porosity changes to be isolated eluding gravity effects. To avoid numerical errors arising from having porosity magnitudes equal to zero, an arbitary value of limiting porosity of 0.1 was introduced. This will not be necesary if gravity is considered.

Porosity changes in the column are plotted for an initial water saturation of 0.35 (Figure 5.17). Even though there are dramatic changes in porosity over time, they have not affected pore pressure or displacement responses (Figures 5.19 and Figure 5.18). This observation obviously is a consequence of not including related changes in permeability that follow the deformation and porosity variations in the porous medium.
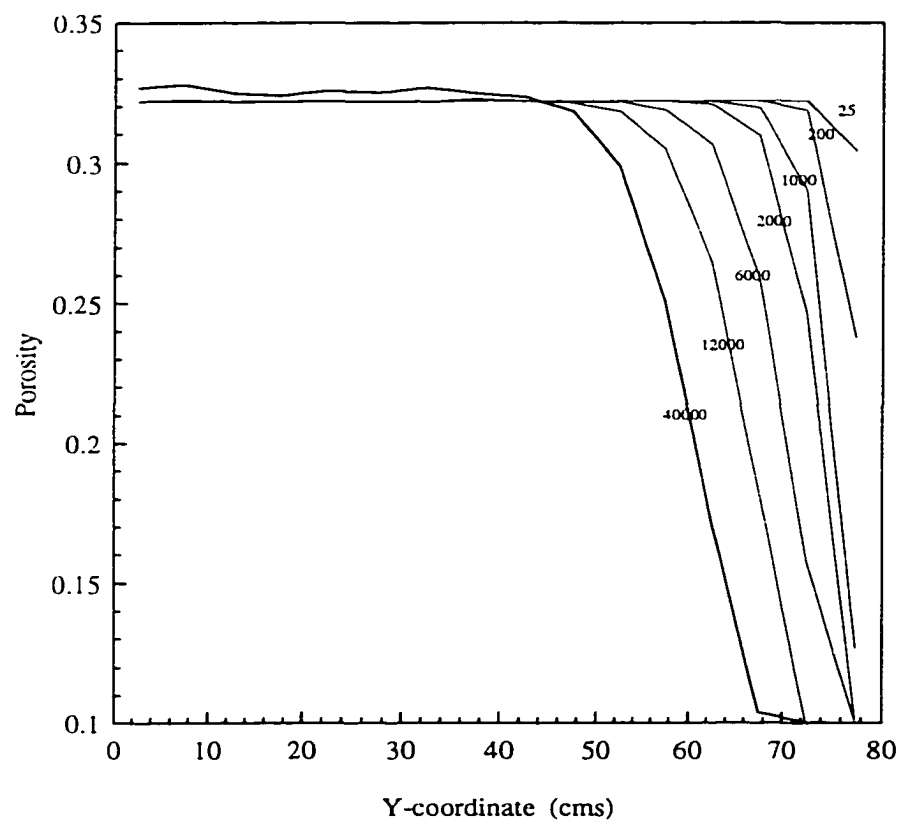
114

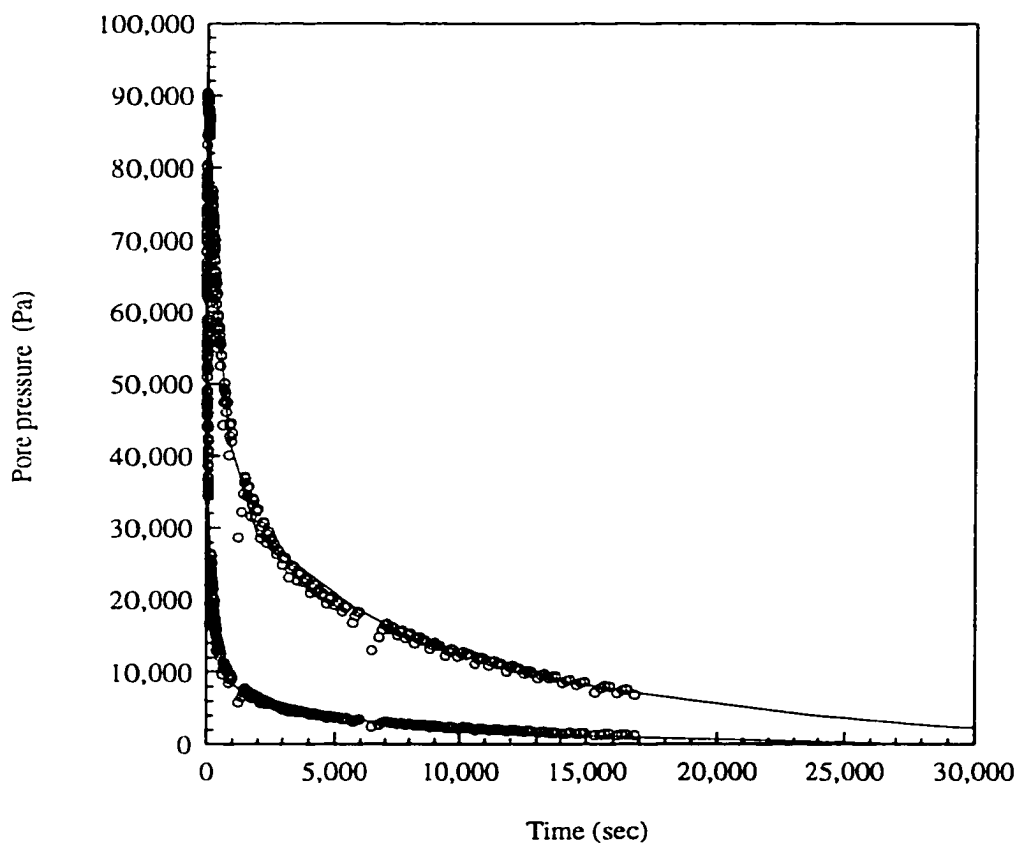Figure 5.17: Porosity changes in time (expressed in seconds) along the column height

Figure 5.18: Comparison of pore pressure results with porosity update (dots) and without porosity changes (line) for initial water saturation of 0.35
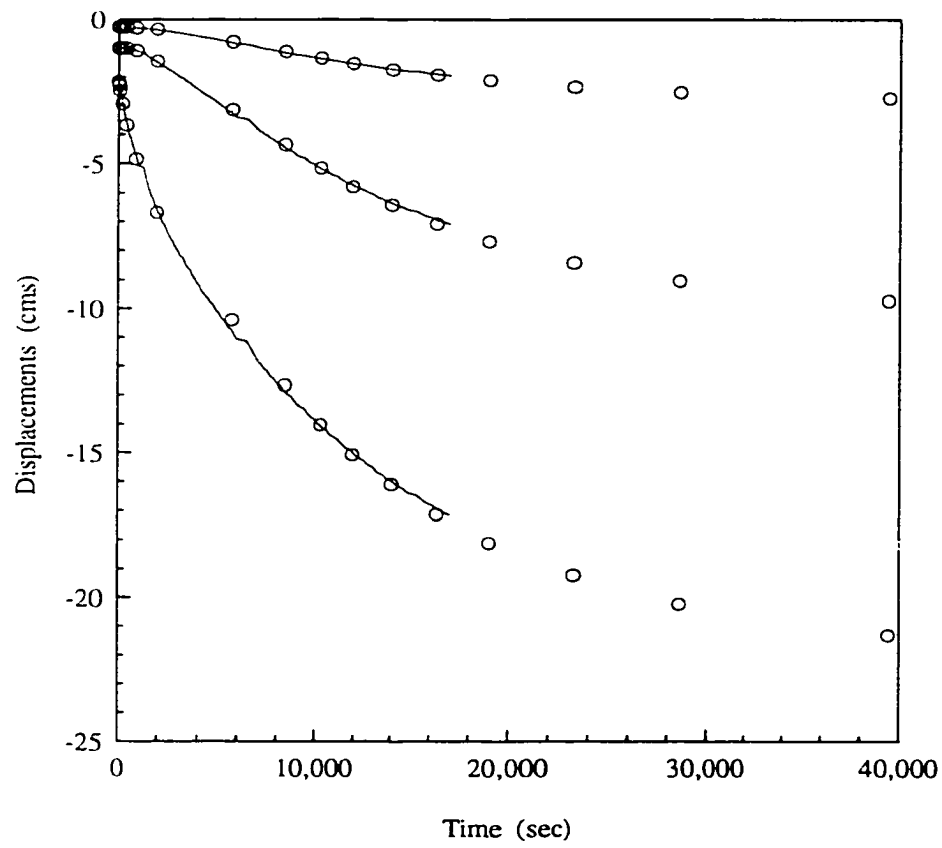
116

Figure 5.19: Comparison of displacement results with porosity update (dots) and without porosity changes (line) for initial water saturation of 0.35

117

Note To Users

The original document received by UMI contained pages with poor print. Pages were filmed as received.

118

This reproduction is the best copy available.

UMI

.l to 0.85, the

pe of the rela-

. is decreasing

dary or outlet

tions. Collins

the saturation

if the relative

curve. In the

ndary effect is

sed but rather

o zero.

.l saturations

ng, the water

ice is located)

5000 seconds

column. Any

column. Any

since almost

the column,

wo-phase flow

which is re-

er 6

ation Examples

)duction

of the code have been demonstrated in several example prob-

ext. First, two-phase flow coupled with solid deformations

or the column problem. Parametric studies were performed

ience of initial saturation, elastic properties and softening

ie excess of pore pressure dissipation and settlements.

mpaction of an idealized reservoir drained by a single well

der, side and overburden layers were included in the model,

w and deformations being taken into account in all layers.

softening of the reservoir rock, layer property contrast and

ipon the behavior of the reservoir was considered.

6.2 Consolidation problems

6.2.1 One-dimensional consolidation coupled with two-phase flow

The column problem presented in Section 5.5.1 was taken to model simultaneous flow of two fluids coupled with deformations of the material. The boundary conditions for both stress/displacements and fluid flow are the same as shown in Figure 5.7. In this example, the relative permeability curves have been taken from the literature [72] as:

$$k_{rw} = 0.733S_w - 0.1099$$
$$k_{ro} = -0.733S_w + 1.1099 \tag{6.1}$$

A hyperbolic function [34] was taken for the capillary pressure curve, from the same data set [72]:

$$P_c = \frac{13.159 - 10.8459S_w}{1 + 3.6262S_w} * 6980 \ (Pa) \tag{6.2}$$

In Figure 6.1, the excess pore pressure dissipation for different initial saturations is shown. The pore pressure dissipation is smaller for decreasing values of initial water saturation. In this case the capillary pressure has been ignored.

The change in water saturation along the column height is shown in Figure 6.2. As the oil is displaced out of the column, the water saturation increases begin from the top. At later times, the water saturation increases

119

PLEASE NOTE

Page(s) not included with original material and unavailable from author or university. Filmed as received.

UMI

stricted when several fluids are flowing at the same time.

The influence of the capillary pressure is presented in Figure 6.6 for an initial saturation of $S_{wo} = 0.35$. The capillary pressure enhances the flow such that a faster decrease in pore pressure occurs. At higher initial water saturations this effect is not important, since capillary pressure is very low at high water saturation values. The change in saturation considering the effect of capillary pressure is shown in Figure 6.7. The change in saturation is higher in the case where capillary pressure is present, because capillary forces are enhancing flow. For this particular case (elastic moduli, permeability and loads imposed), the capillary phenomenon is more important than the poroelasticity effects (excess of pore pressure due to stresses and deformations of the solid), but this is not always the case.
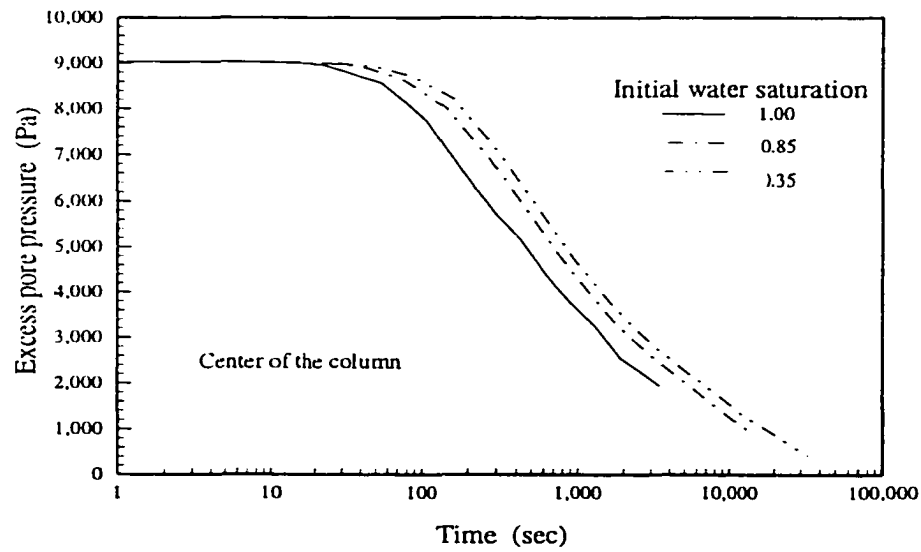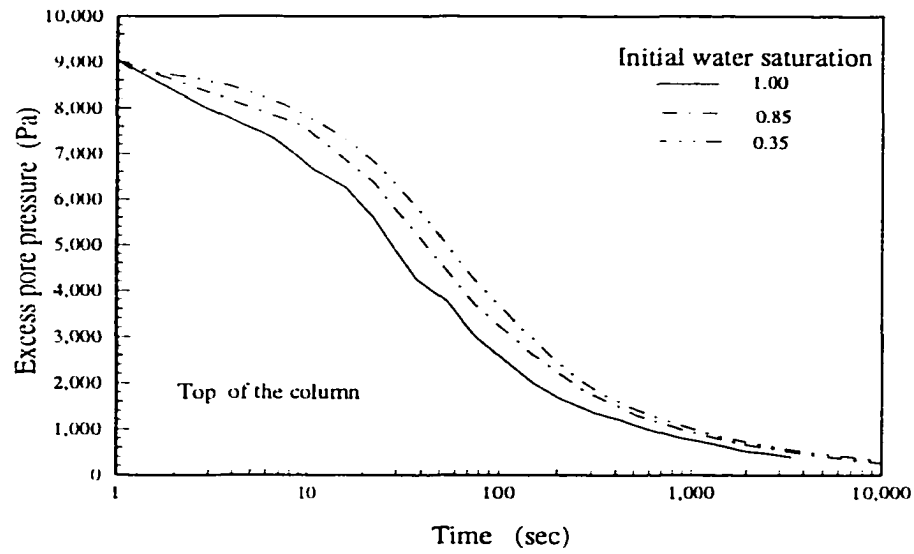
Figure 6.1: Pore pressure evolution in time for top and center of the column. Comparison for different initial saturations (two-phase flow).
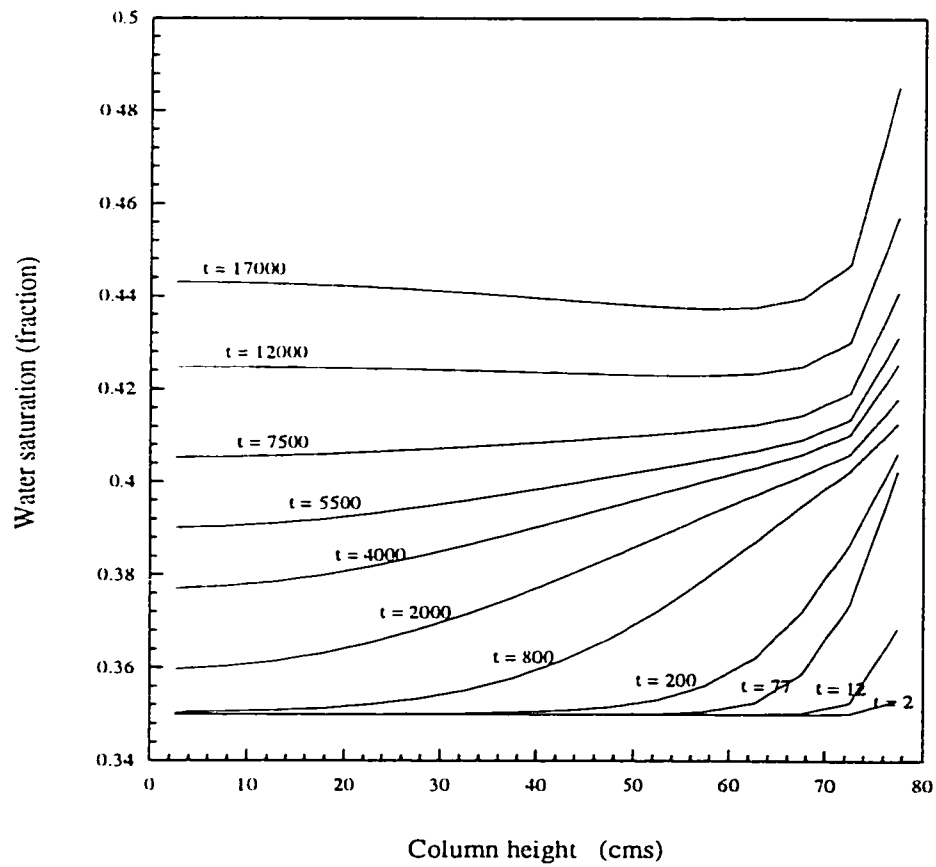
122

Figure 6.2: Saturation changes along the column height(top is at 80 cms) for two-phase flow conditions. Initial water saturation is $S_{wo} = 0.35$ (time in sec. is indicated over each curve).
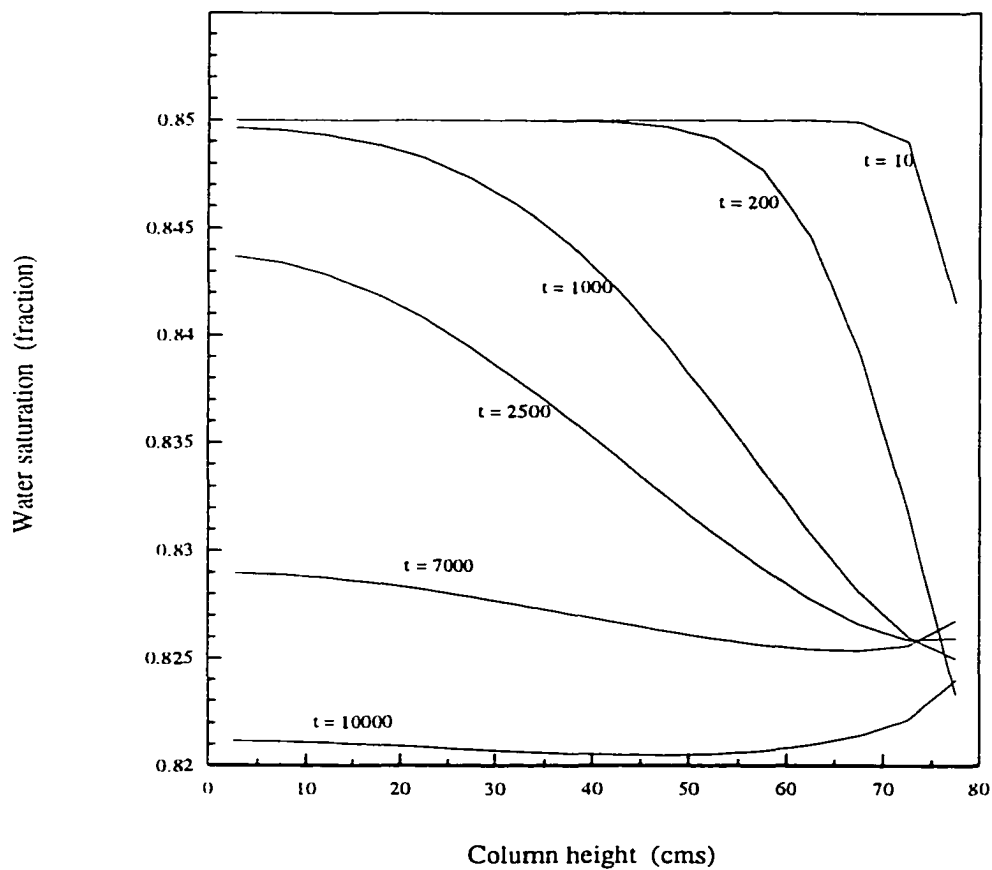
123

Figure 6.3: Saturation change along the column height (top is at 80 cms) for two-phase flow. Initial water saturation is $S_{wo} = 0.85$ (time in sec. is indicated over each curve).
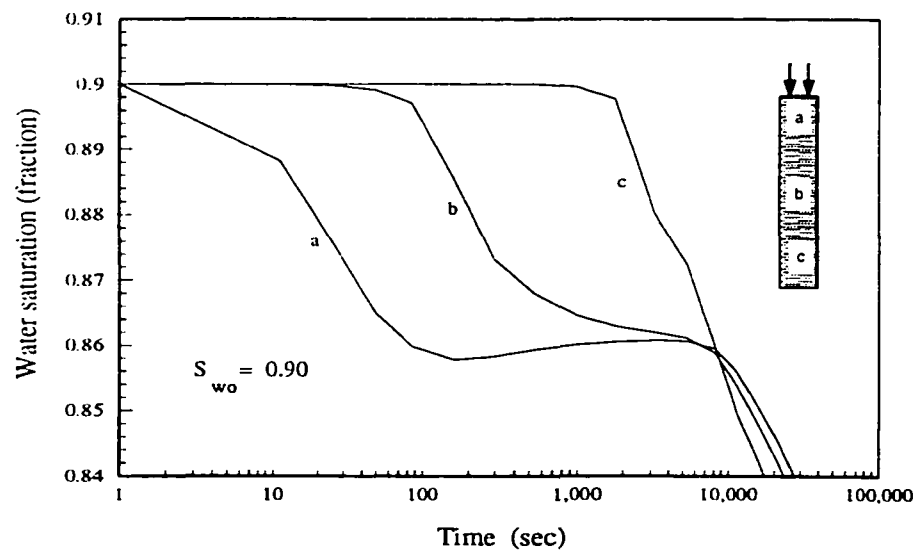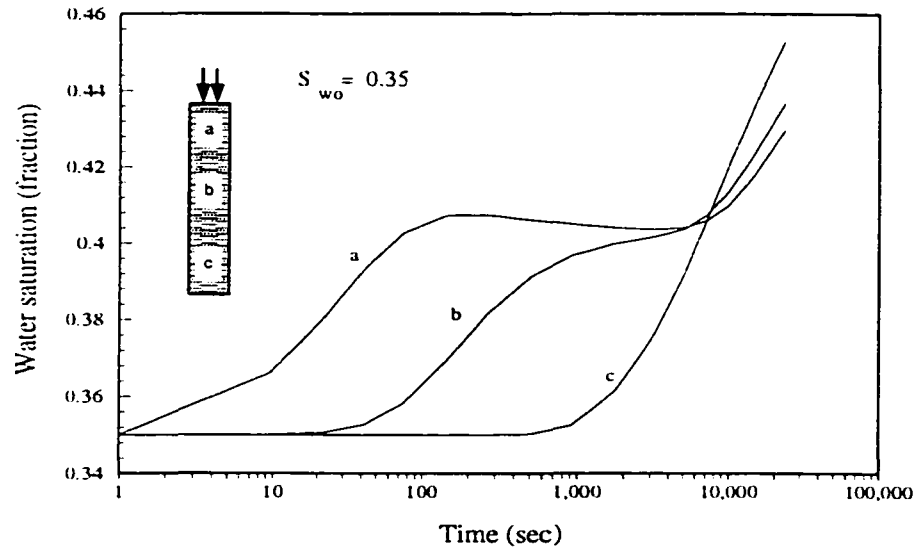
124

Figure 6.4: Change of saturation with time for: a) top, b) center; and c) bottom of the column.
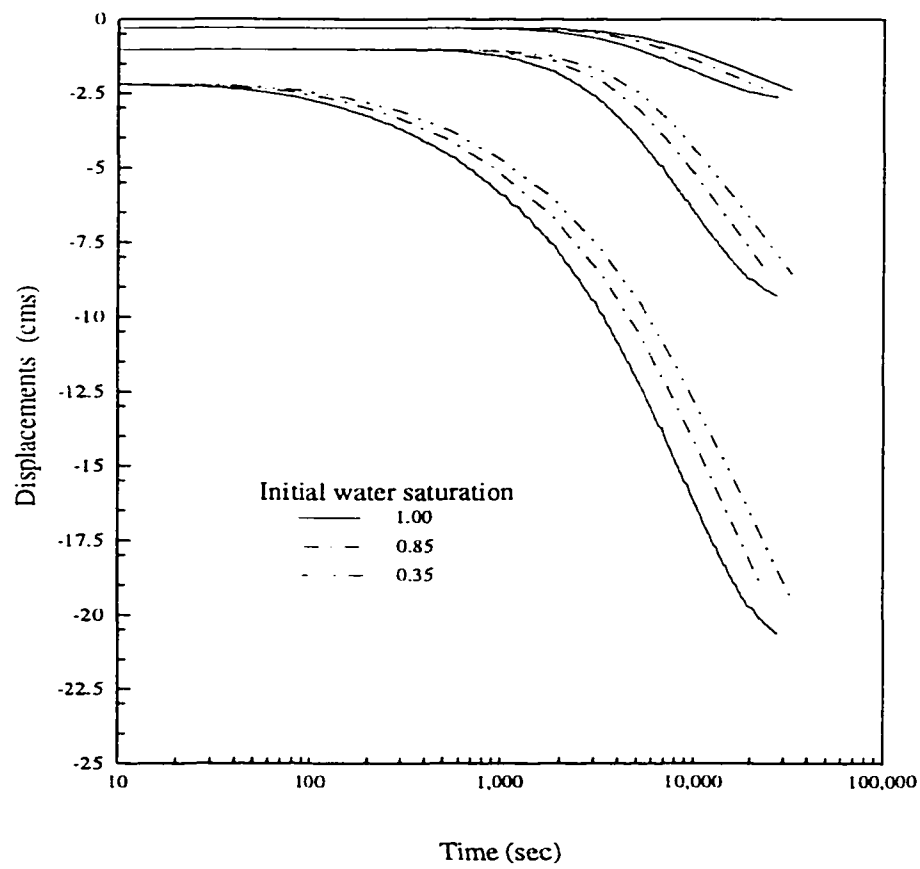
125

Figure 6.5: Displacements for different initial water saturation at: a) top; (b) center; and c) bottom of the column.
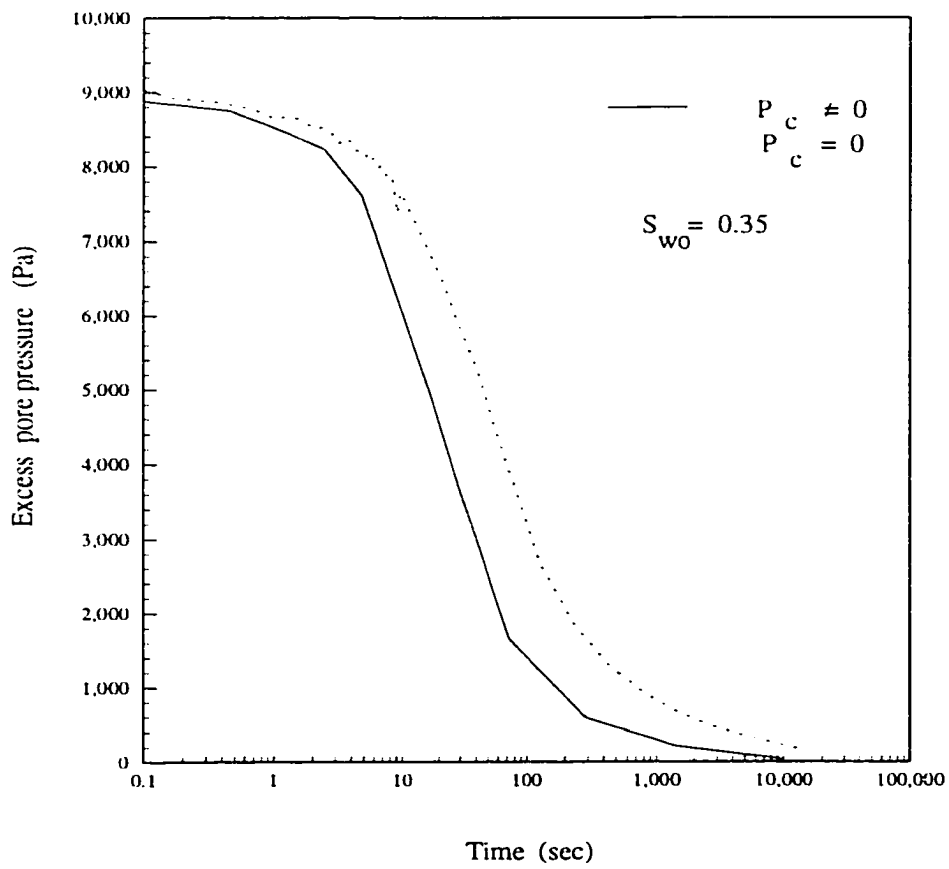
126

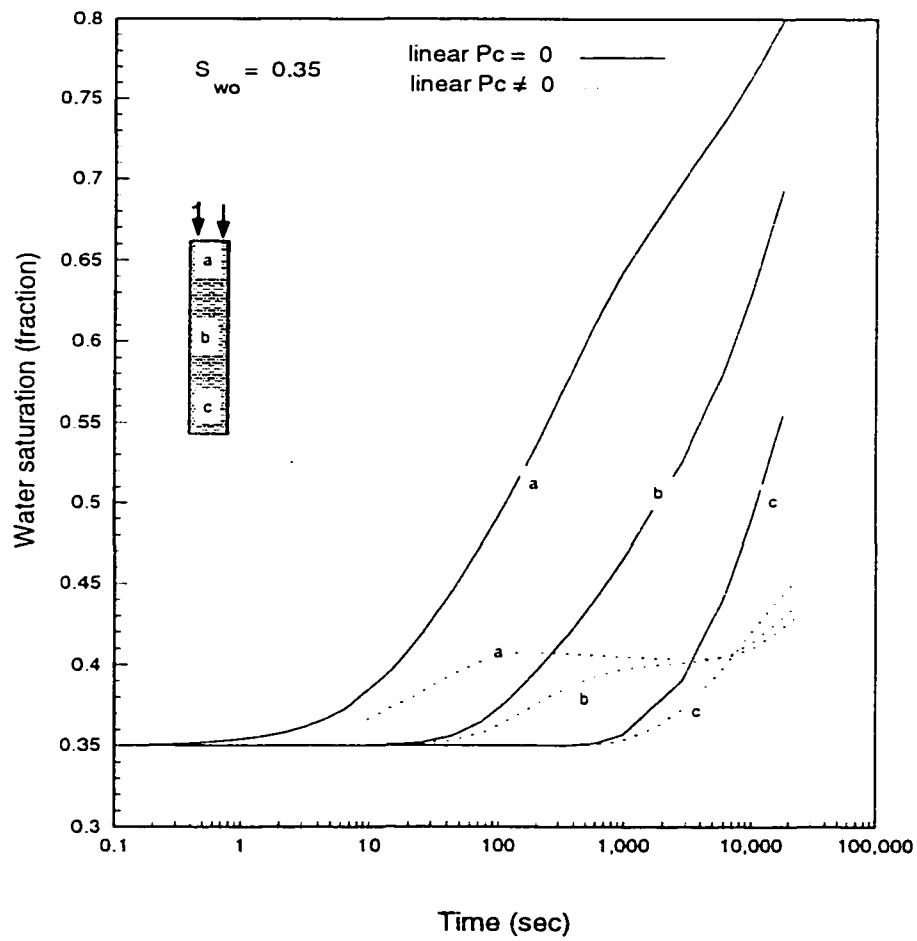Figure 6.6: Influence of capillary pressure on pore pressure dissipation for the top of the column.

Figure 6.7: Saturation changes with time for selected points; effect of capillary pressure.

128

6.2.2 One-dimensional consolidation problem with a trilinear constitutive equation

The case of two-phase flow in a column (same geometry than that used in the verification problem) having a trilinear constitutive equation with a softening segment (as described in Section 3.8.1) is considered next. The following figures compare the results for a linear elastic relationship vs. a trilinear constitutive equation. Initial saturation, and capillary pressure effects are varied to show the influence of these parameters in the overall behavior. The parameters for the trilinear constitutive equation used in this example are [2]: $\epsilon_{m1} = 1.0$; $\epsilon_{m2} = 10.0$; $\tau_{res} = 5.0 MPa$; $G_{initial} = 35 MPa$. All the remaining parameters are the same as shown in Figure 5.7.

In Figure 6.8 a comparison of excess pore pressure dissipation in the column for linear and trilinear material is presented. The excess of pore pressure is maintained longer for the trilinear material because there is additional pore pressure generation due to the volumetric strain produced by the column compaction as a function of time. The amount of undrained pore pressure generation is a function of the volumetric strain which is higher in the case of a material that loses its rigidity. Figure 6.9 shows the effect of including capillary pressure; the excess pore pressure is dissipated faster in this case. Again the material that softens maintains a higher pore pressure than does the linear material.

---

[2]Refer to Figure 3.6 in Chapter 3.

The saturation distribution along the colum, for selected times, is presented in Figure 6.10. At early times, there is no difference in the saturation profile for the column; however, as time progresses, the saturation changes affect deeper layers in the column for a material with softening behavior.

The displacements in the column are increased once the material starts to soften (see Figure 6.11). Figure 6.12 shows the degradation of the shear modulus as the strain process progresses in time. The influence of initial saturation and capillary pressure on shear modulus degradation is presented in Figure 6.13. When capillary pressure is present, since there is a faster depletion of excess of pore pressure, the material deforms faster and the shear modulus is degraded faster. The influence of initial saturation is not very important in this case.
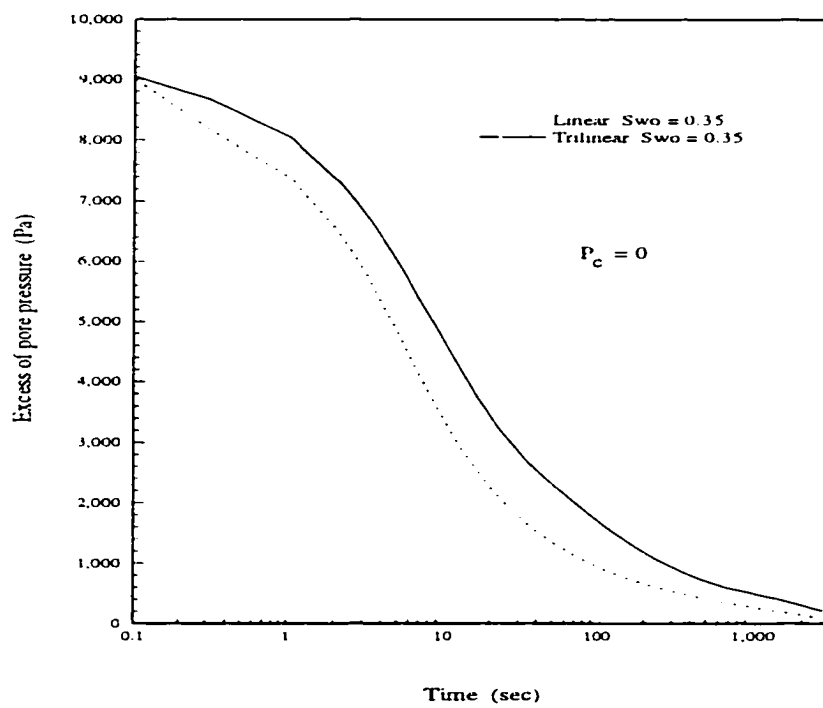
Figure 6.8: Pore pressure evolution with time. Comparison between materials with linear elastic and trilinear constitutive equations.
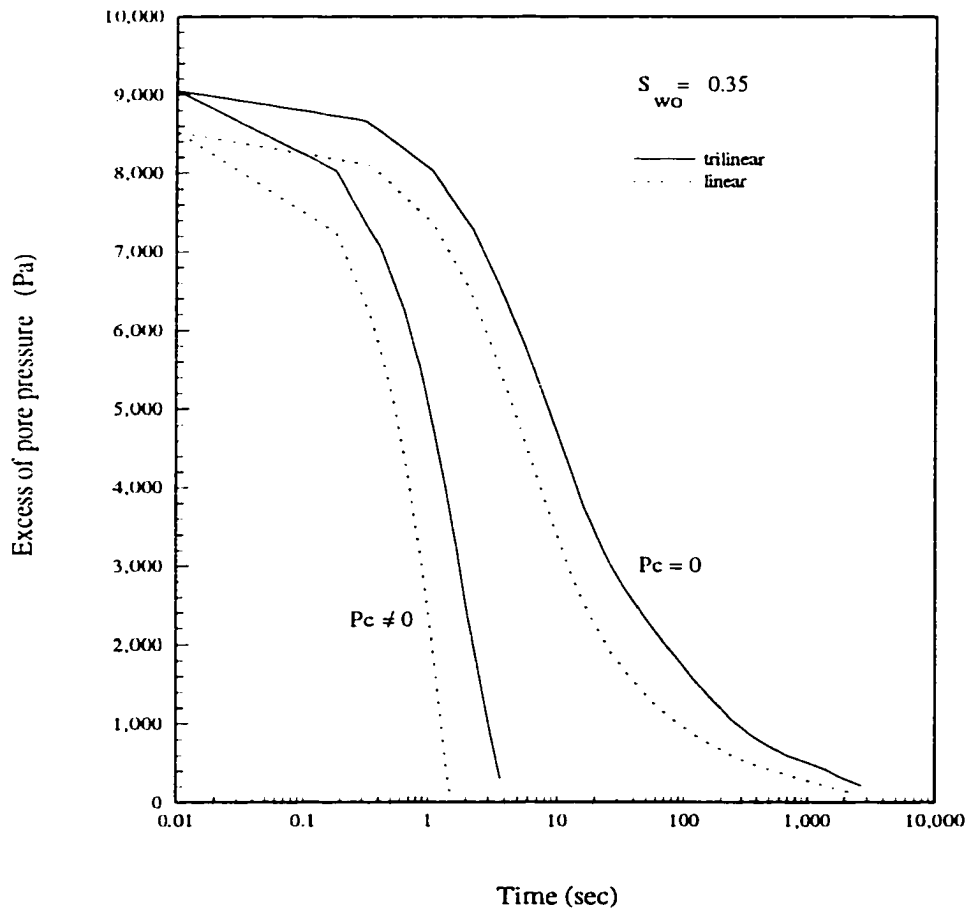
131

Figure 6.9: Pore pressure evolution with time. Comparison between materials with linear elastic and trilinear constitutive equations, considering capillary pressure.
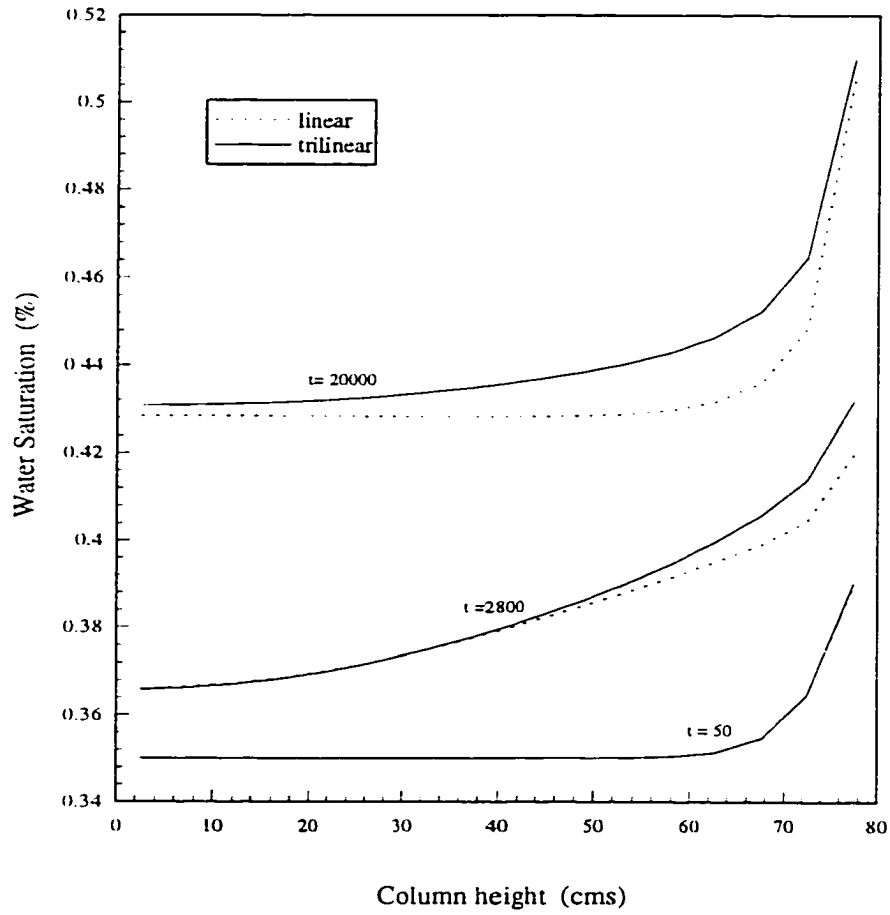
132

Figure 6.10: Change in saturation with time for selected points. Comparison between materials with linear elastic and trilinear constitutive equations.

133

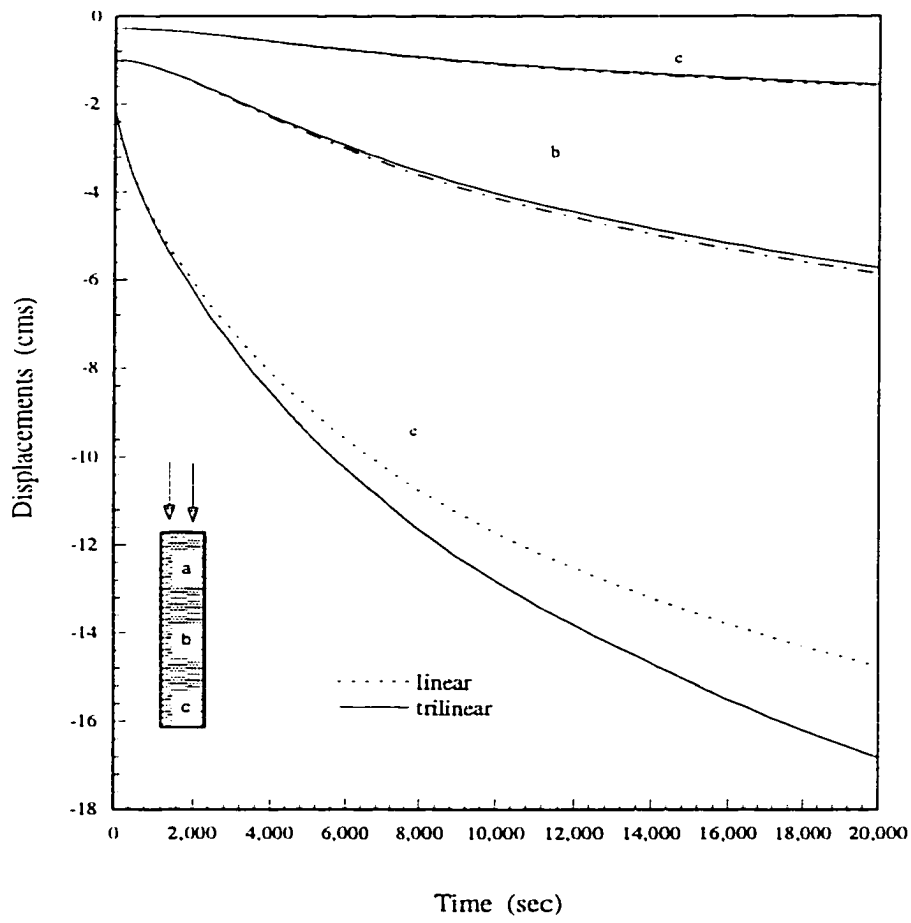Figure 6.11: Progress of settlement with time for selected points in the column. Comparison between materials with linear elastic and trilinear constitutive equations.
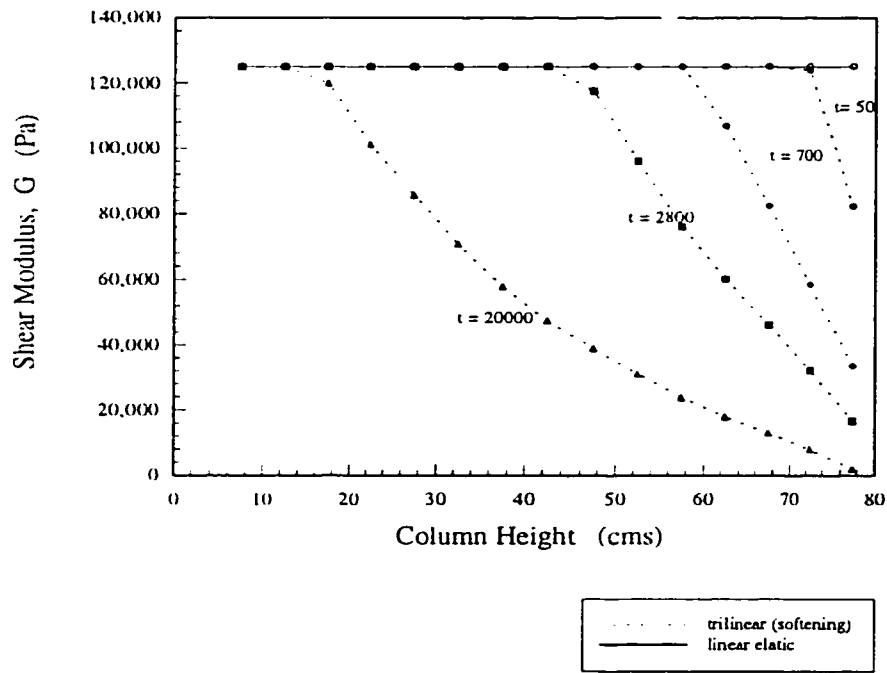
134

Figure 6.12: Change in shear modulus as the coupled strain-flow process evolves for a material with a trilinear constitutive equation.
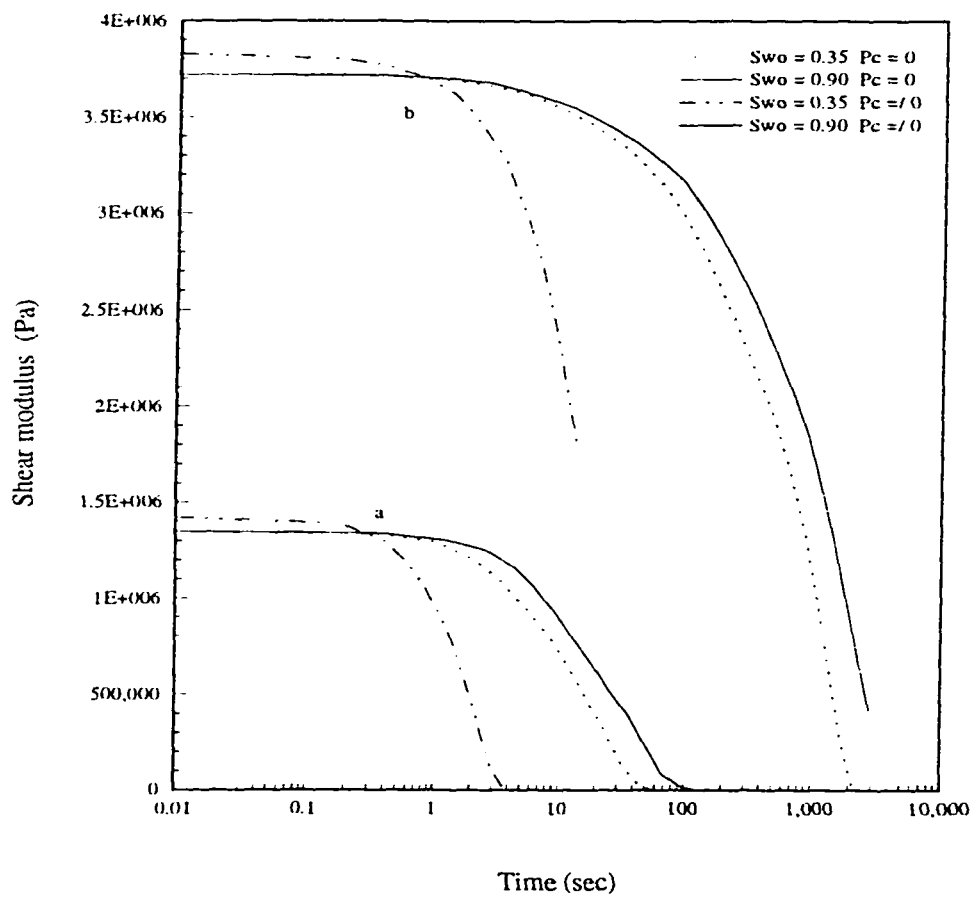
135

Figure 6.13: Change in shear modulus with time for top (a) and center (b) of the column.

6.3 Compaction of an idealized oil reservoir

6.3.1 Introduction

Compaction and subsidence problems have been treated traditionally without coupling, where production (fluid flow) and rock deformations (compaction and subsidence) are calculated in a staggered manner [55], [113], [18], [13], [19], [36], [74], [106]. That is, the pore fluid pressures are calculated using a reservoir simulator considering just fluid flow; and then, these are input into a stress-strain code (usually a finite element program) to determine the corresponding displacements. The uncoupled approach can not properly account for the additional pore pressure generated during compaction of the reservoir and overburden subsidence, neither can it consider arching effects of the surrounding layers. Besides, reservoir simulation studies with rock compressibility, C_r, as the unique parameter which accounts for rock mechanics can be misleading [44].

The major aspects to be considered when studying the complex processes occuring during compaction of a reservoir are: a) stress path during depletion and influence of different constitutive equations calibrated through laboratory test following these stress paths; b) effect of interaction of the overburden, side and underburden to account for arching effects; c) permeability changes during depletion; d) plastic yield or failure (shear and pore collapse mechanisms should be included for particular cases) and the possibility of exceeding these limits during depletion of the reservoir.

137

Recent in-situ stress measurements have demonstrated that many reservoirs follow stress paths [3] that are significantly different from the traditional hydrostatic stress or uniaxial strain boundary conditions [118]. Since rock behavior is dependent upon the stress path, and since the early stages of reservoir loading are generally unknown, modelling can be a powerful aid to study different particular scenarios and make estimations which can then be considered for determining the appropriate laboratory testing program to obtain the pertinent rock parameters.

6.3.2 Modelling of compaction of a reservoir with softening behavior

A hypothetical example has been considered to show how the model can give insights into the compaction of a reservoir. Figure 6.14 presents the geometry and boundary conditions of the problem. A reservoir 100 meters thick and 600 m wide (using the symmetry of the center line) was studied, since it would be costly to model all the layers. An additional load corresponding to 500 m overburden was input as a boundary condition and just 450 meters of overburden were actually included in the model. The complete section is 850 m high and 900 m wide. The left, bottom and right boundaries of the model are represented with rollers to indicate no deformation normal to these boundaries. There is no drainage on all boundaries, except for a short segment located at the symmetry line representing the left boundary of the

---

[3]Defined as (σ'_h/σ'_v).

138

reservoir, which is considered for the purposes of modelling as a boundary open to flow, resembling a well.

The modelling of the overburden has been considered to be a very important issue in this type of problem [118]. However, to the author's knowledge, the flow characteristics of the over/under and sideburden have been ignored in this type of analysis, so far. In this example these layers are considered including fluid flow and mechanical interaction in the overall behavior. The initial stress state consisted of the weight of the rocks, as the vertical stress component; and lateral stress increasing with depth with a horizontal to vertical stress factor, $K = 0.25$. The initial pore pressure was set to the corresponding hydrostatic pressure. Figure 6.15 show the initial conditions for the model. The initial conditions were input in the model and a few mechanical iterations were needed to equilibrate the system. Very little displacement occurred, but after inital mechanical equilibrium, displacements were reset to zero. Gravity forces were activited in this case.

A very simple well pressure history was considered as boundary condition for pressure at the face of the reservoir for a single well configuration example. Pressure at the 'wellbore' face was lowered to 500 kPa at time $t = 0^+$ and at $t = 100$ days it was set to 50 kPa. As a first example, only water flow was considered in all layers, next the reservoir initial saturation was set to $S_{wo} = 0.35$, while other layers were maintained with $S_{wo} = 1$.

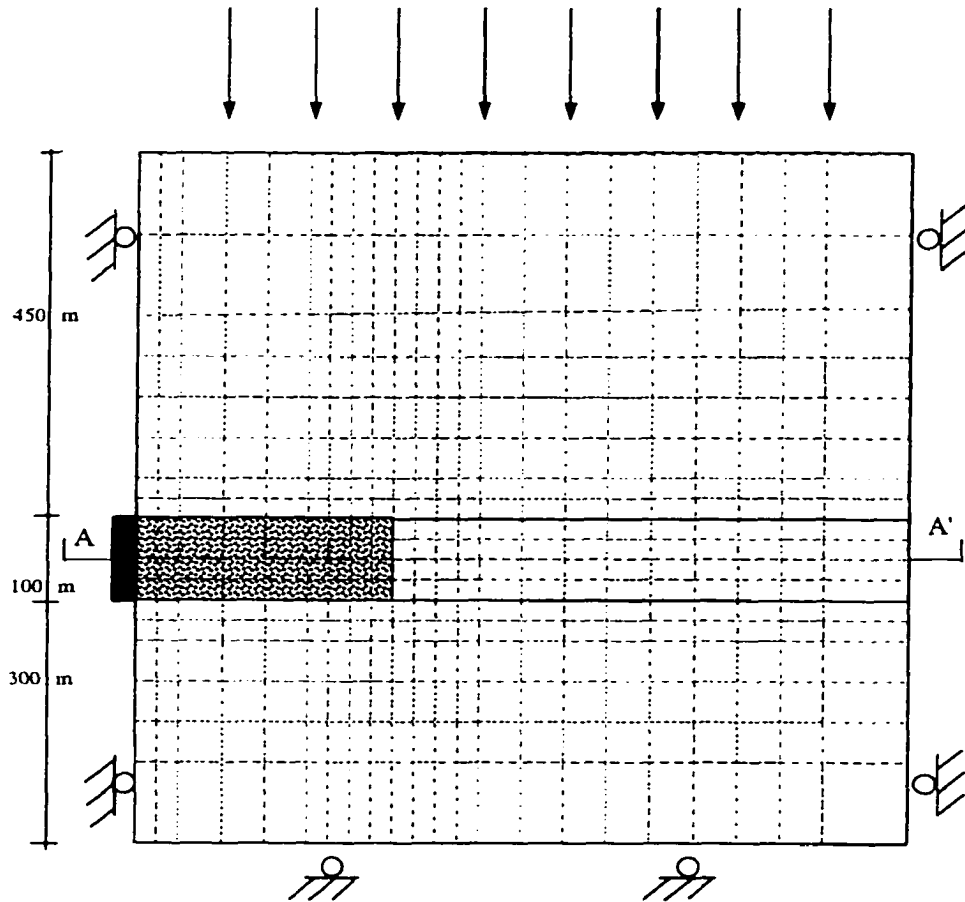The evolution of pore pressure in the reservoir and adjacent layers is

139

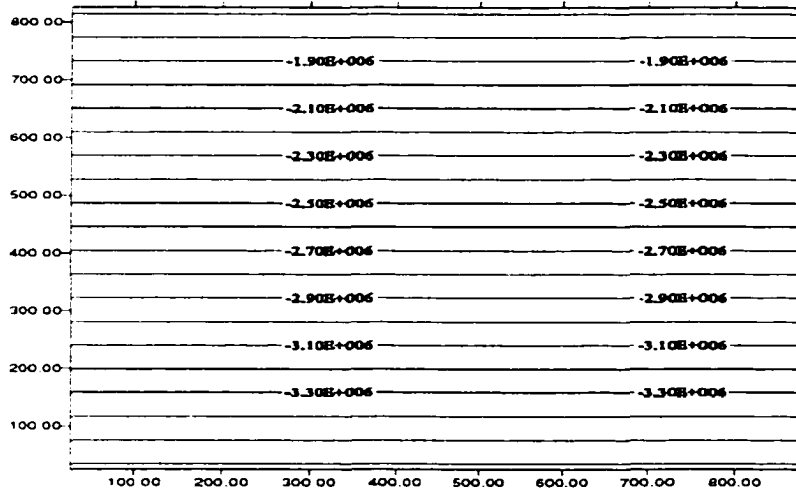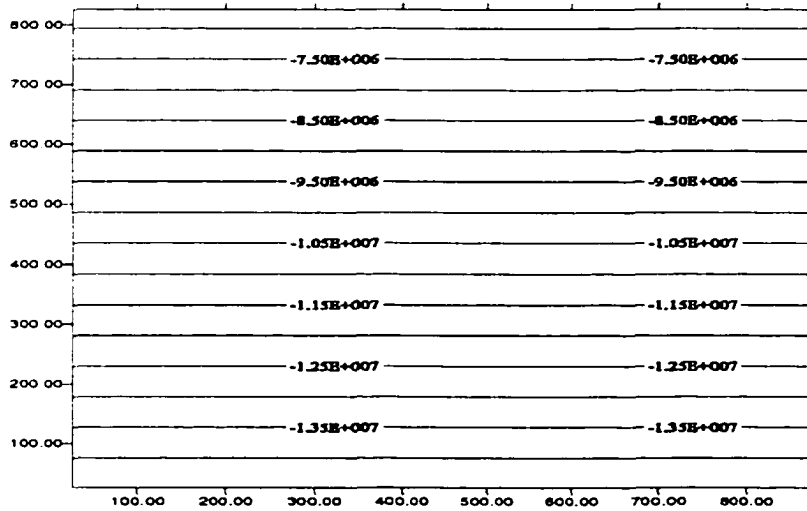Figure 6.14: Schematic representation of the reservoir, over and underburden. For reservoir $E = 6.9e^8$ Pa, $\nu = 0.2$, $\phi = 0.25$, $\kappa = 8.64e^{-7}$ $N - m^4/days$; for other layers $E = 6.9e^9$ Pa, $\mu = 0.2$, $\phi = 0.25$, $\kappa = 8.64e^{-8}$ $N - m^4/days$

Minor principal stresses (Pa)

Major principal stresses (Pa)

Figure 6.15: Pore pressure and stress initial conditions in the model

141

presented in Figures 6.16, 6.17 and 6.18. Pore pressure changes are limited to the reservoir layers at the beginning; but, for this particular case, even with one order of magnitude permeability difference, at 10 days the pore pressure field outside the reservoir is perturbed, which leads to additional deformation in the surrounding layers.

The effective major principal stress contours are presented in Figures 6.19 and 6.20. As time elapses, the effective stresses increase at the sideburden and over the flanks of the reservoir at the overburden. When pore pressure decreases because of production, the overburden loses support; and, because of its rigidity, stresses increase toward the flanks. This effect will limit the subsidence to some extent because the surrounding layers, which are one order of magnitude stiffer than the reservoir, are taking part of the resulting strains.

Pore pressure and effective major principal stresses along a line $A - A'$ (see Figure 6.14) are shown in Figure 6.21. There is a jump in pore pressure outside of the reservoir to accommodate permeability and stiffness contrasts betweeen reservoir and sideburden. It can be seen that pore pressure in the sideburden is higher than the original pore pressure, which is a consequence of the coupled poroelastic effects. At later times (after 160 days), the sideburden pore pressure started to deplete. The effective stresses responded similarly with a jump, increasing values at the reservoir side boundary.

Figure 6.22 shows the variation of stress path for the line $A - A'$ in

142
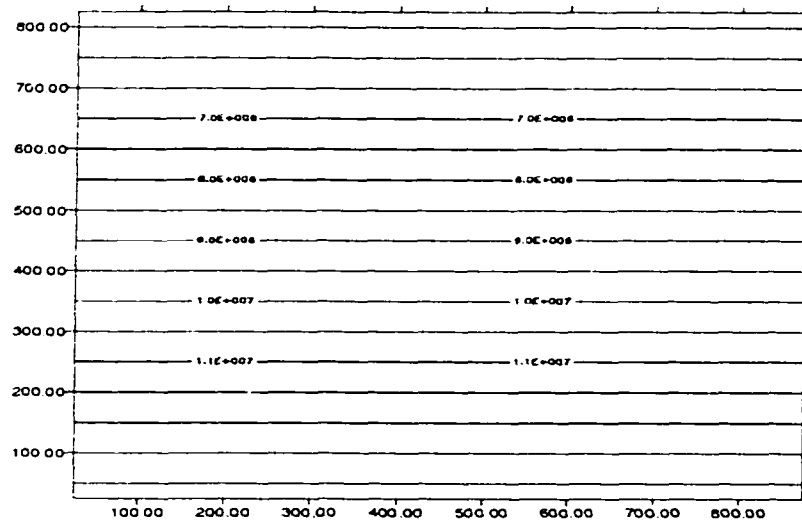
Initial pore pressure profile (Pa)
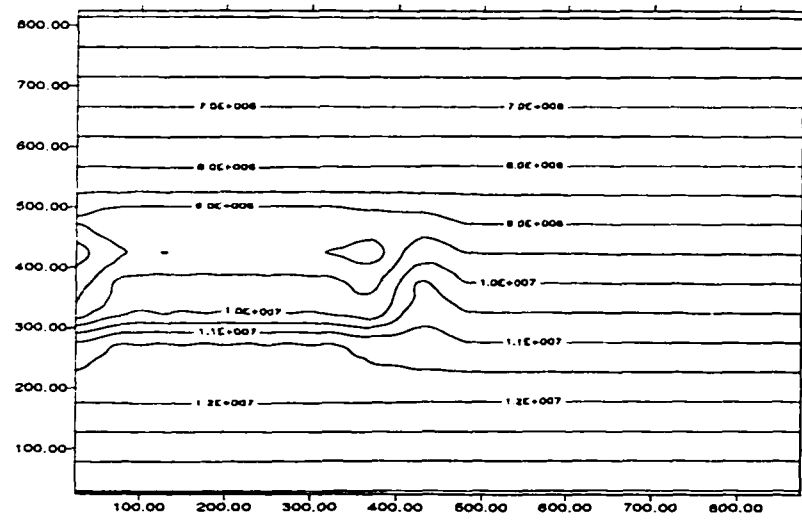
Pore pressure (t = 0.1 days)

Figure 6.16: Contours of pore pressure: a)Initial pore pressure; b) t = 0.1 day.
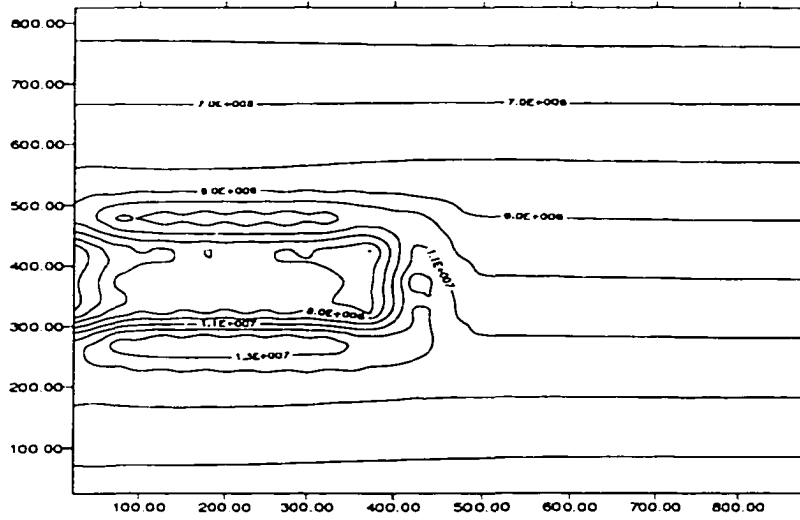
Pore pressure (t = 0.6 days)
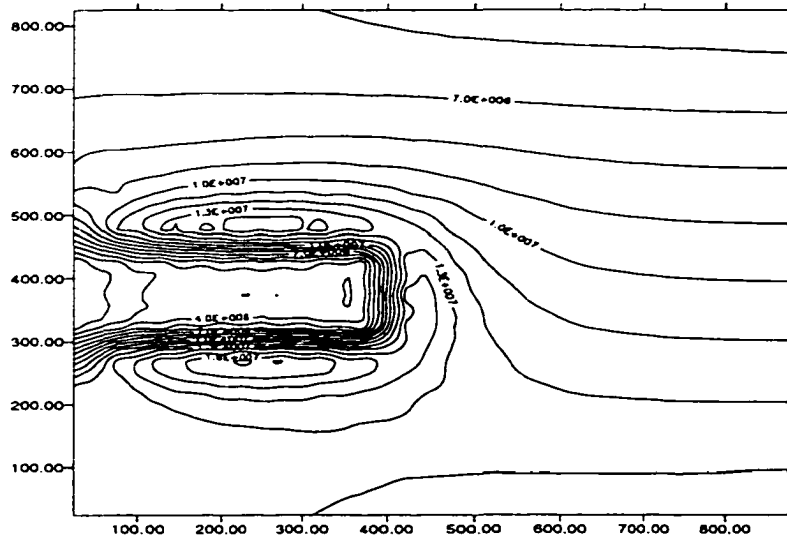
Pore pressure (t = 10 days)

Figure 6.17: Contours of pore pressure: a) t = 0.6; b) t = 10 days

144
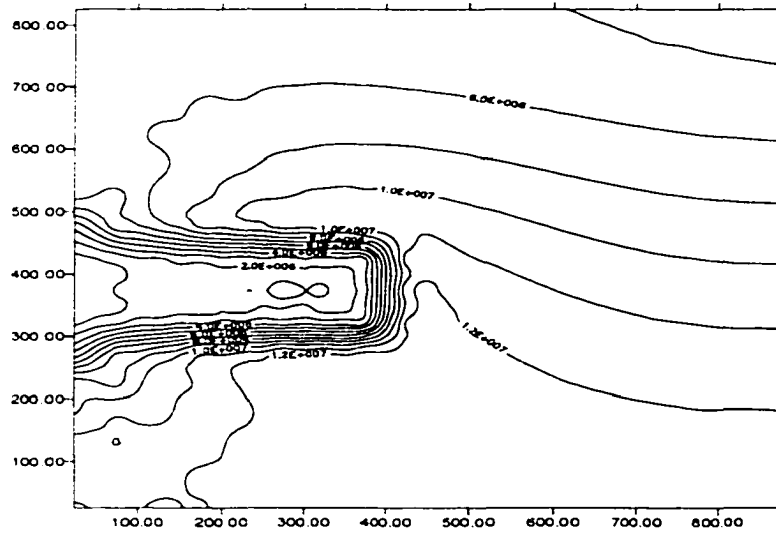
Pore pressure (t = 60 days)
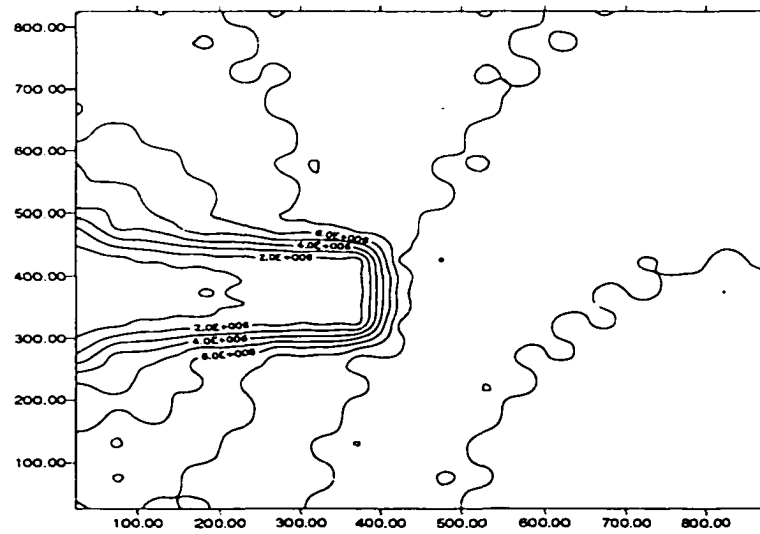
Pore pressure (t = 400 days)

Figure 6.18: Contours of pore pressure: a) t = 60 days; b) t = 400 days

145
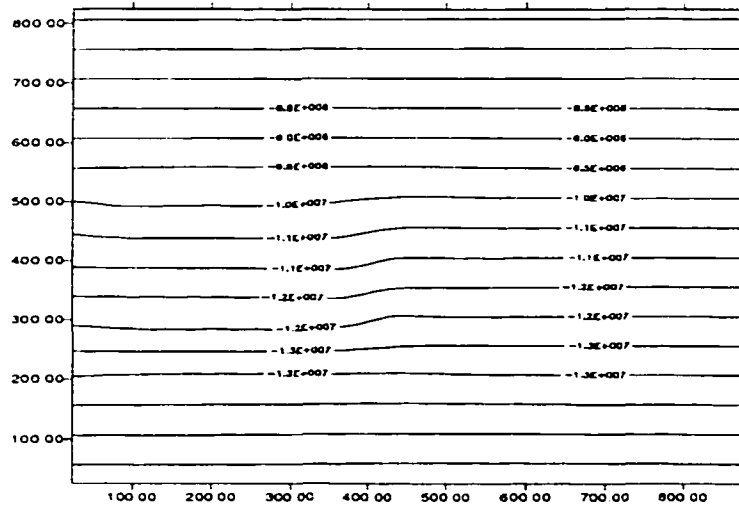
Effective major principal stresses (t = 0.1 day)
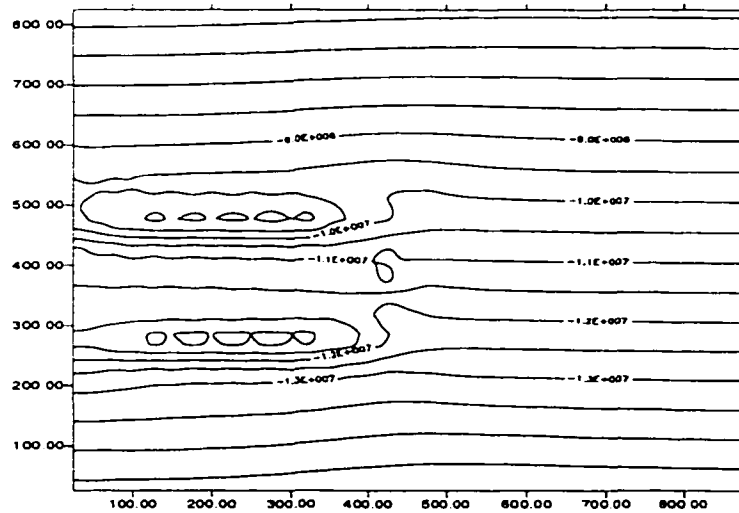
Effective major princpal stresses (t = 0.6 days)

Figure 6.19: Contours of effective major principal stresses: a) t = 0.1 days; b) t = 0.6 day

146
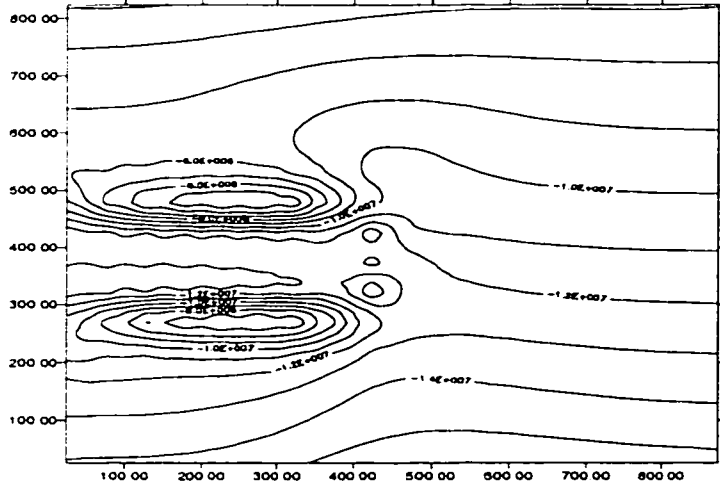
Effective major principal stresses (t = 10 days)
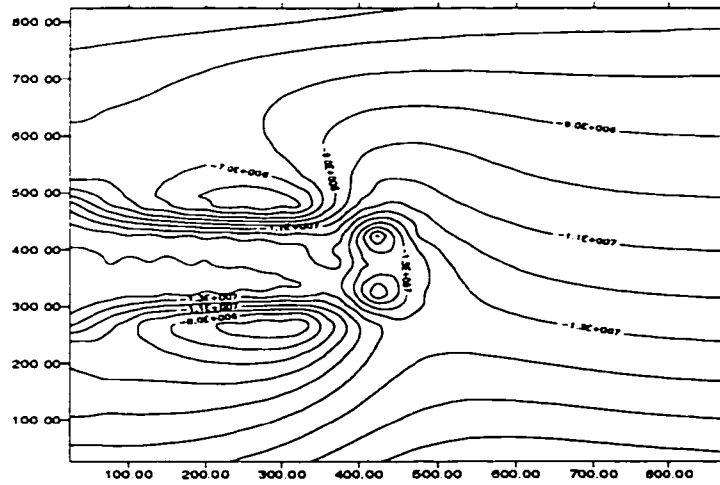
Effective major principal stresses (t = 60 days)

Figure 6.20: Contours of effective major principal stresses: a) t = 10 days; b) t = 60 days

147

the reservoir for different time levels and also the change of K'_o with time for selected points at varying distances from the center line along the line $A - A'$. The figure shows the initial value of $K'_o = \sigma'_h/\sigma'_v = 0.25$ along the width of the reservoir. However, the reservoir does not compact under a constant K'_o, but rather, due to coupling, it varies in space and time in a complex manner. This means that using a single constant value of rock compressibility for the whole reservoir, as in the conventional reservoir simulation approach, is meaningless. At most, rock compressibility should have been made to depend on the stress path at different locations in the reservoir.

The difference of considering a coupled approach vs. an uncoupled approach is shown in Figures 6.23, 6.24 and 6.25. For the uncoupled calculations, the undrained pore pressure generation during the mechanical part of the code was disabled. In this approach the program worked just by passing pore pressure information produced from the fluid flow calculations to the mechanical routines of the code (stress-strain calculations) to determine new effective stresses and the resulting strains.

As can be seen in these figures, even for the reservoir, there is an initial increase of pore pressure over the original values. This is occurring despite the fact that the 'well' pressure has been lowered and production in on going. Pore pressure, of course, decreases thereafter because of depletion of the reservoir. Note in Figure 6.25 that the coupled approach predicted higher pore pressures and only after a long period of time the values (coupled and

148
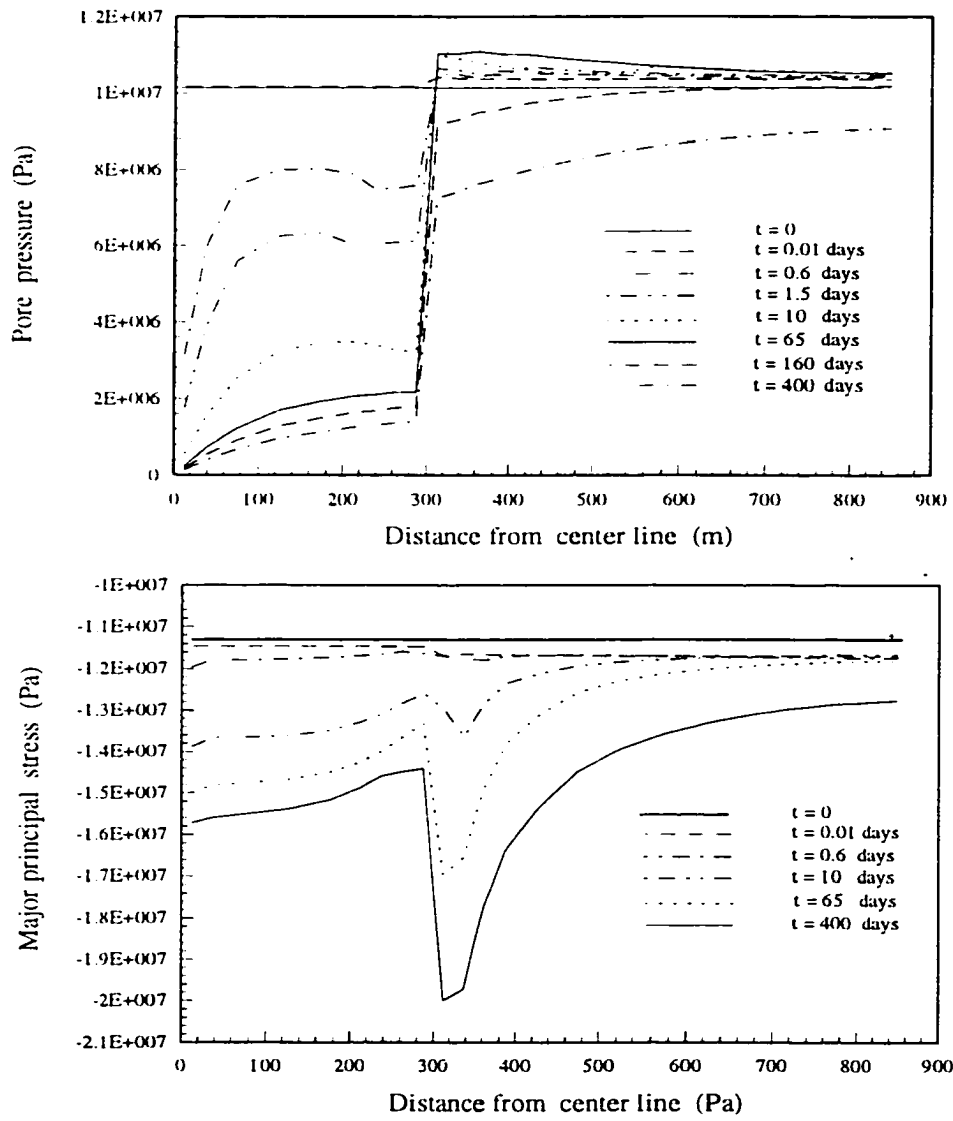
Figure 6.21: Pore pressure and major principal stresses at the center of the reservoir (line A-A') at different times.

149
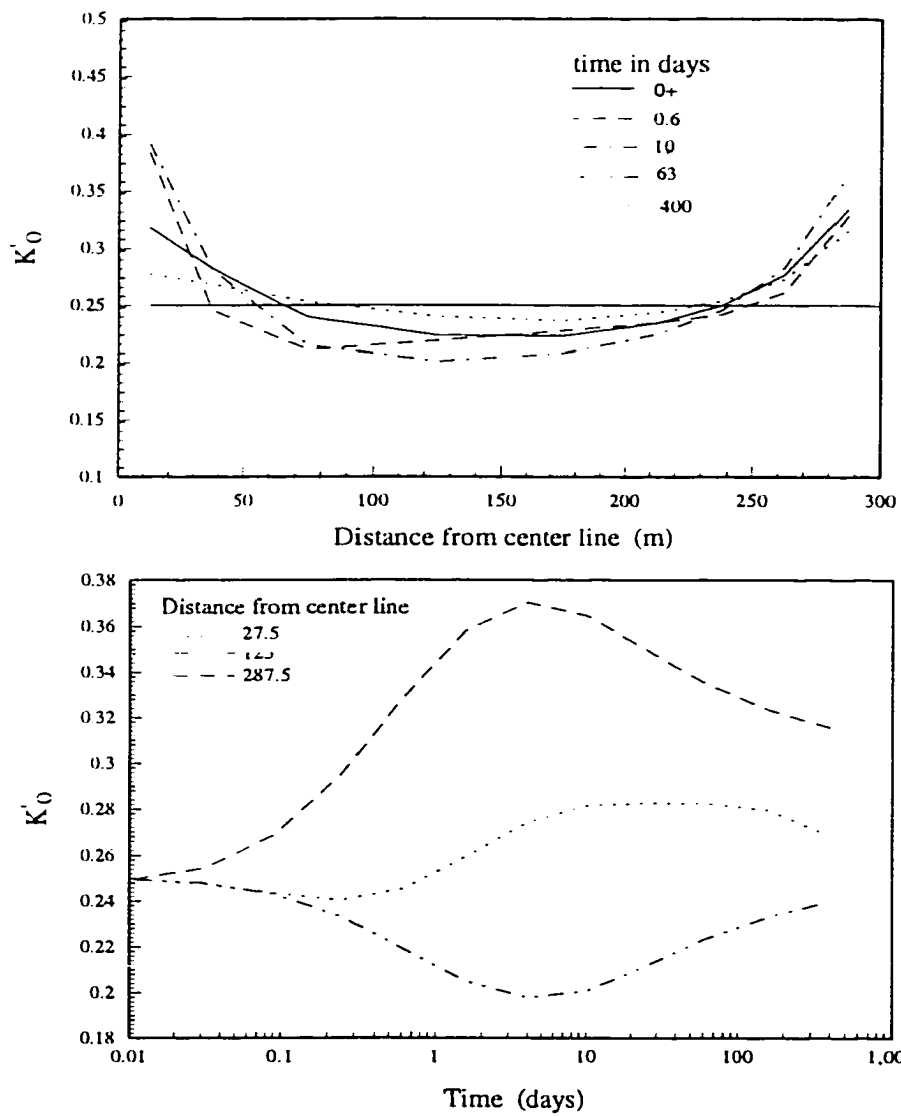
Figure 6.22: a) K'_o for the reservoir at the center line $(A - A')$ and b) change of K'_o for center, middle and flank of the reservoir vs. time.

150
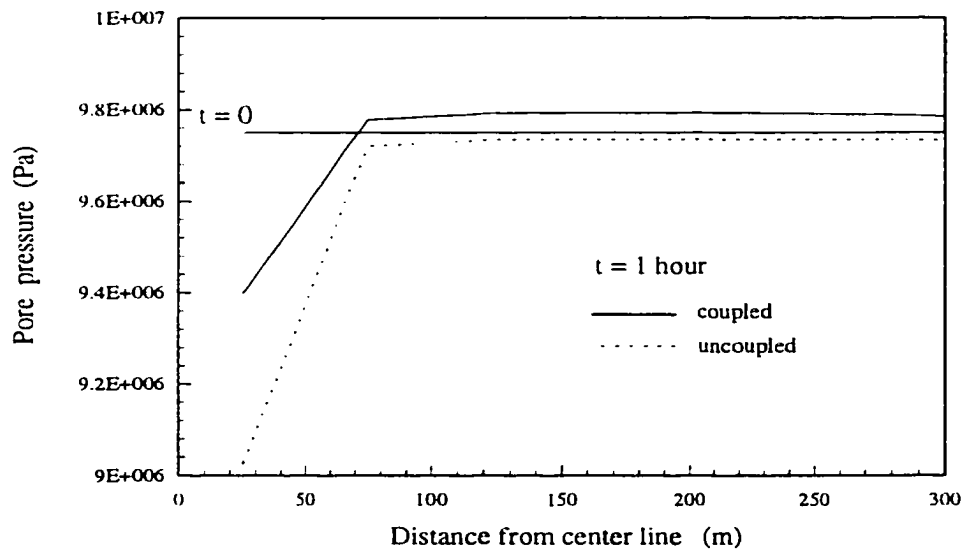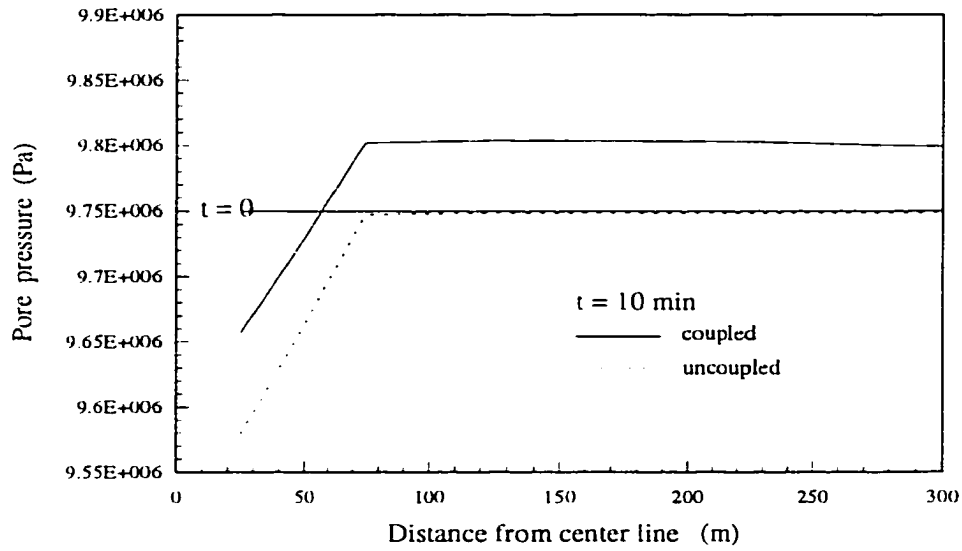
Figure 6.23: Effect of coupling on pore pressure response at 10 min and 1 hour.
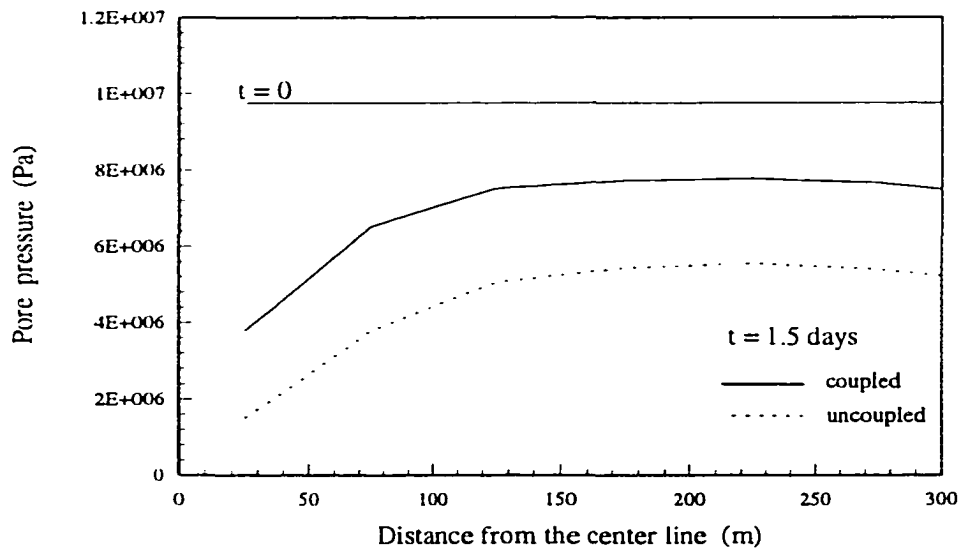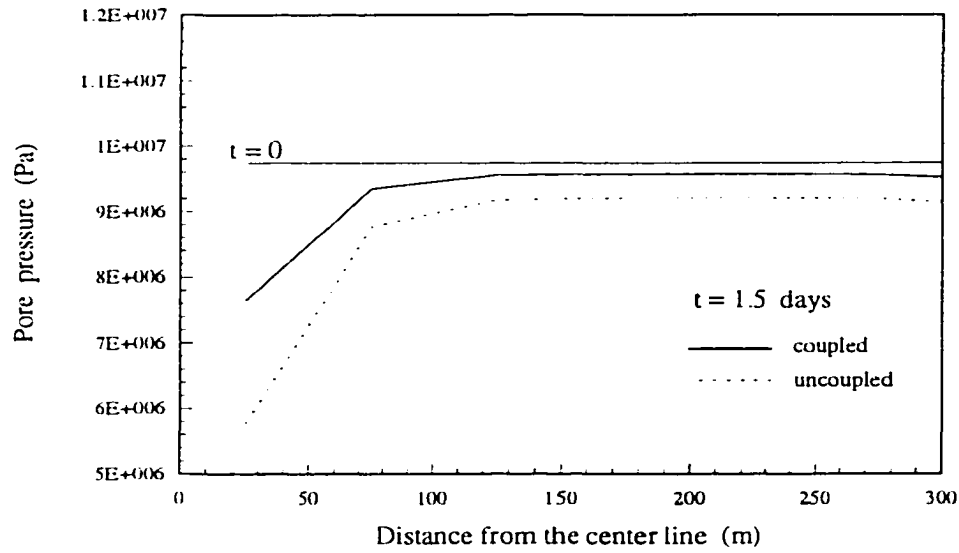
Figure 6.24: Effect of coupling on pore pressure response at 0.25 and 1.5 days.
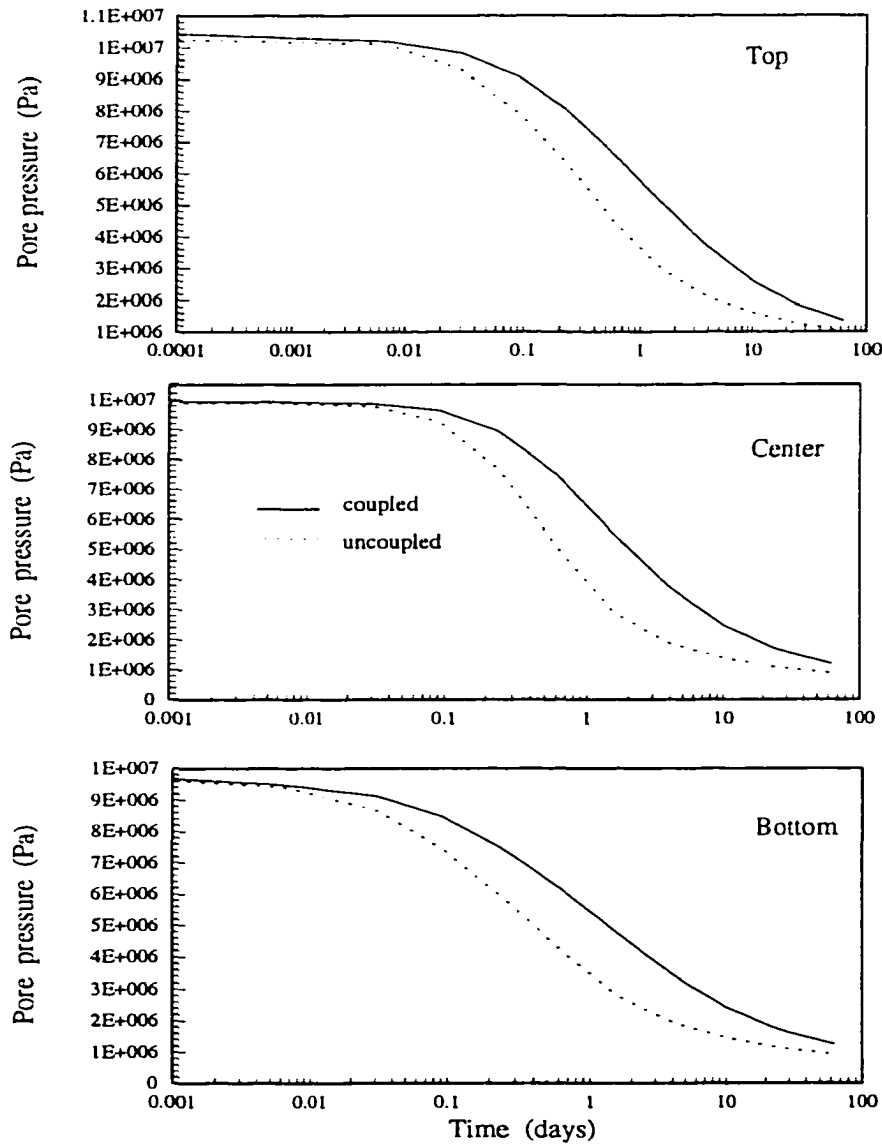
Figure 6.25: Effect of coupling on pore pressure response at top, center and bottom of the reservoir.

153

uncoupled) tend to match. Therefore, for this particular set of values, the use of an uncoupled approach tend to overpredict depletion in the reservoir.

It is remarkable that the behavior of the reservoir is not uniform in terms of displacements. Figure 6.28 shows that points below the center of the reservoir were lifted at the begining and later, settlements started. This is because the underburden is expanding. This uplifting can be appreciated in Figure 6.26 where deformed meshes are presented for different time levels. The original mesh is denoted with dotted lines. For later times (Figure 6.26(c)) the underburden just below the reservoir is almost in the same position that it was in the beginning, while the side and underburden compacted much more. The field of displacements is presented in Figure 6.27 with arrows whose lengths (exaggerated 100 times) represent the magnitude of displacements and point towards the corresponding displacement direction. Here the behavior of the adjacents layers of the reservoir is again clearly shown . The 'subsidence bowl' is well delineated in this figure.

The poroelastic (coupled) effects can also be noticed in the settlements as is shown in Figure 6.29, where the displacements predicted by the uncoupled approach are higher at the top of the reservoir than the ones resulting from the coupled calculations. However, at the bottom of the reservoir the uplift predicted by the uncoupled approach is higher than that resulting from the coupled approach.

The results of saturation changes for the case of two-phase flow in the

154

reservoir with coupled rock deformation (other parameters are the same as in the single-phase flow case are presented in Figure 6.30. Again results are not non-uniform for points at top, center and bottom of the reservoir. The fact that the water saturation increases less at the center is a consequence of the reservoir being 'squeezed' from both top and bottom; and consequently, oil is delivered from top and bottom layers of the reservoir.

Figure 6.31 shows the flowrate for top, center and bottom of the reservoir. Note that the higher oil flowrate occurred at the center of the reservoir. The water flowrate, however, is initially higher at the center but it decreases in time below the values for top and bottom.

All results presented before were for a linear elastic rock. The following figures compare the previous results with those obtained by changing the consitutive equation to a trilinear one, as has been defined previously Section 3.8 in Chapter 3). Only the constitutive equation for the reservoir was changed; the side, under and overburden layers remained with a linear elastic constitutive equation. Displacements at the top, center and bottom of the resevoir in Figure 6.32 are the same up to the point in which the reservoir rock started to soften and the displacements increased even 100% at the center of the column. The uplift at the bottom of the reservoir increased, as well.

The effect of the constitutive equation upon other parameters like pore pressure, flowrate, and water saturation is less dramatic for this particular

155
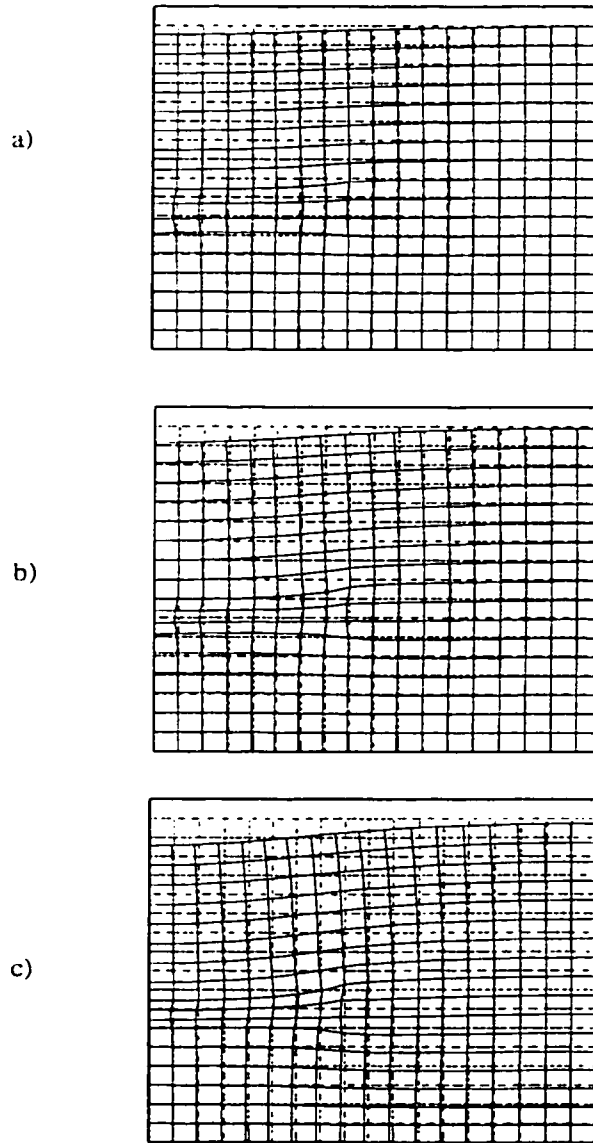
Figure 6.26: Deformed mesh as function of time: a) t = 10 days; b) t = 60 days; and c) t = 400 days.

156
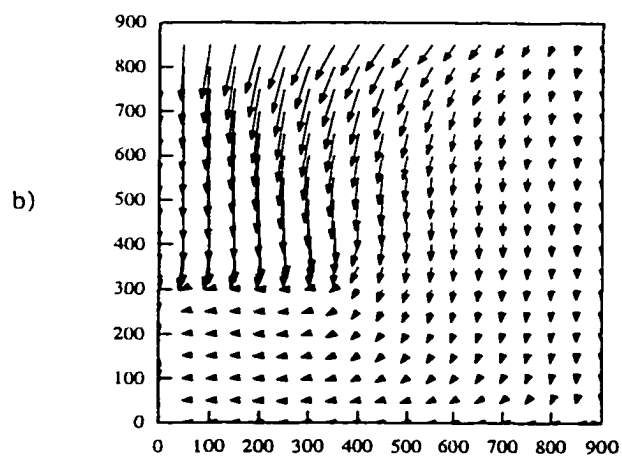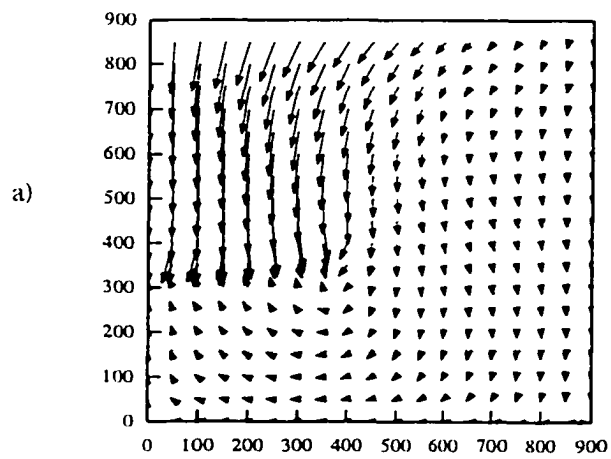
Figure 6.27: Displacement field vectors for different time levels: a) t = 60 days; b) t = 400 days.

157

a)

b)
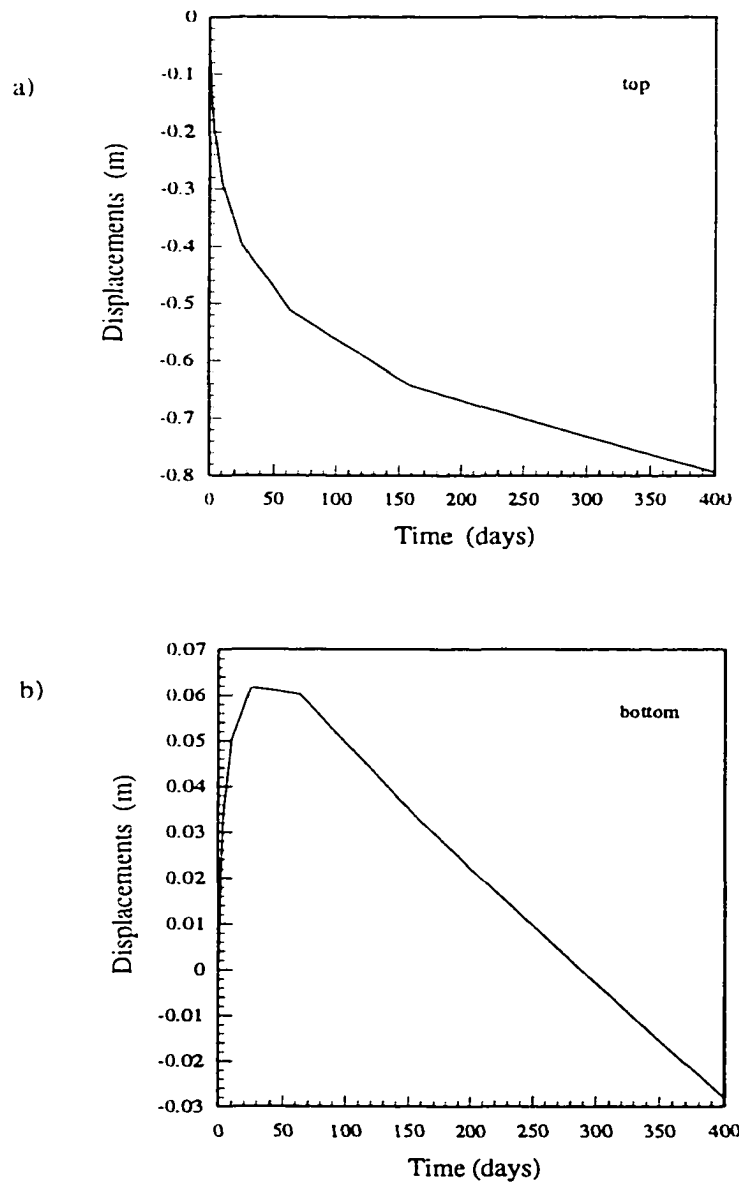
Figure 6.28: Displacements at the center line and top of the reservoir

158
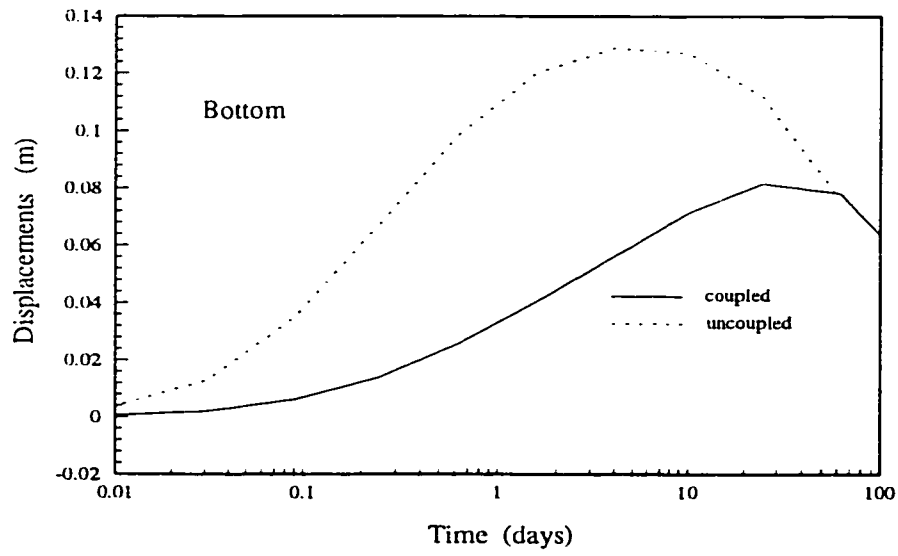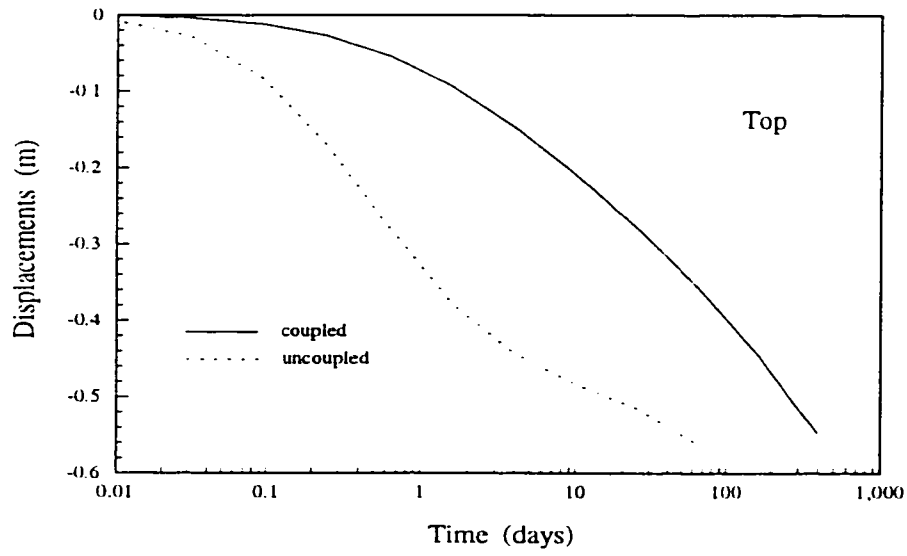
Figure 6.29: Displacements at a) center; and b) top of the reservoir.

159
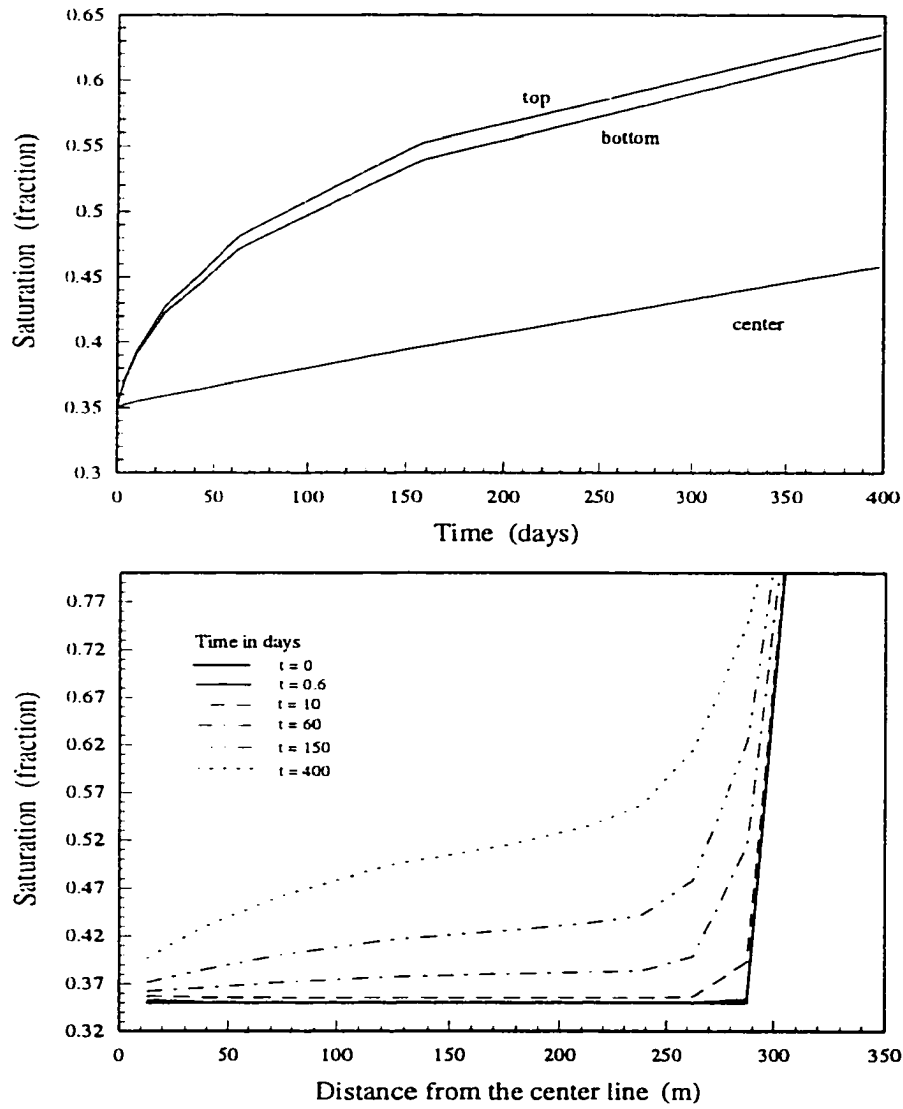
Figure 6.30: Change of water saturation in the reservoir: a) at top, center and bottom; b) at line A-A'.
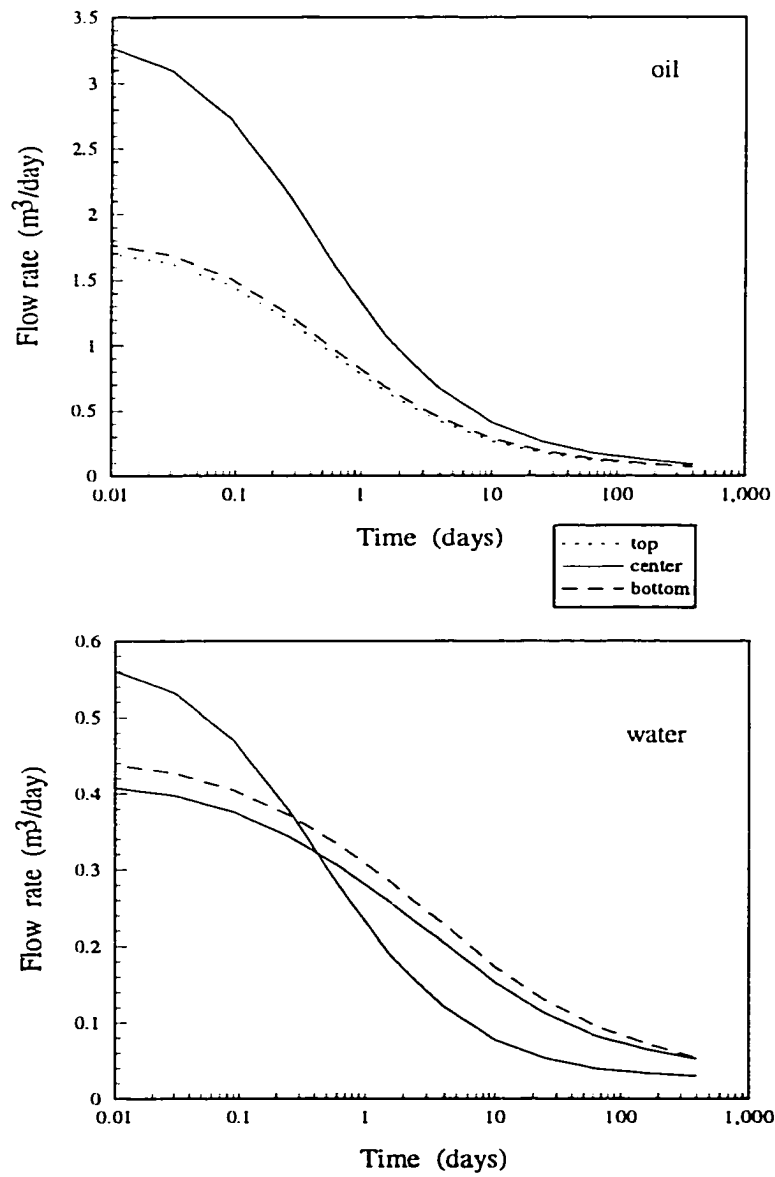
Figure 6.31: Flow rate at the face of the reservoir: a) oil; b)water.

161

set of parameters and geometry, as is shown in Figure 6.33.
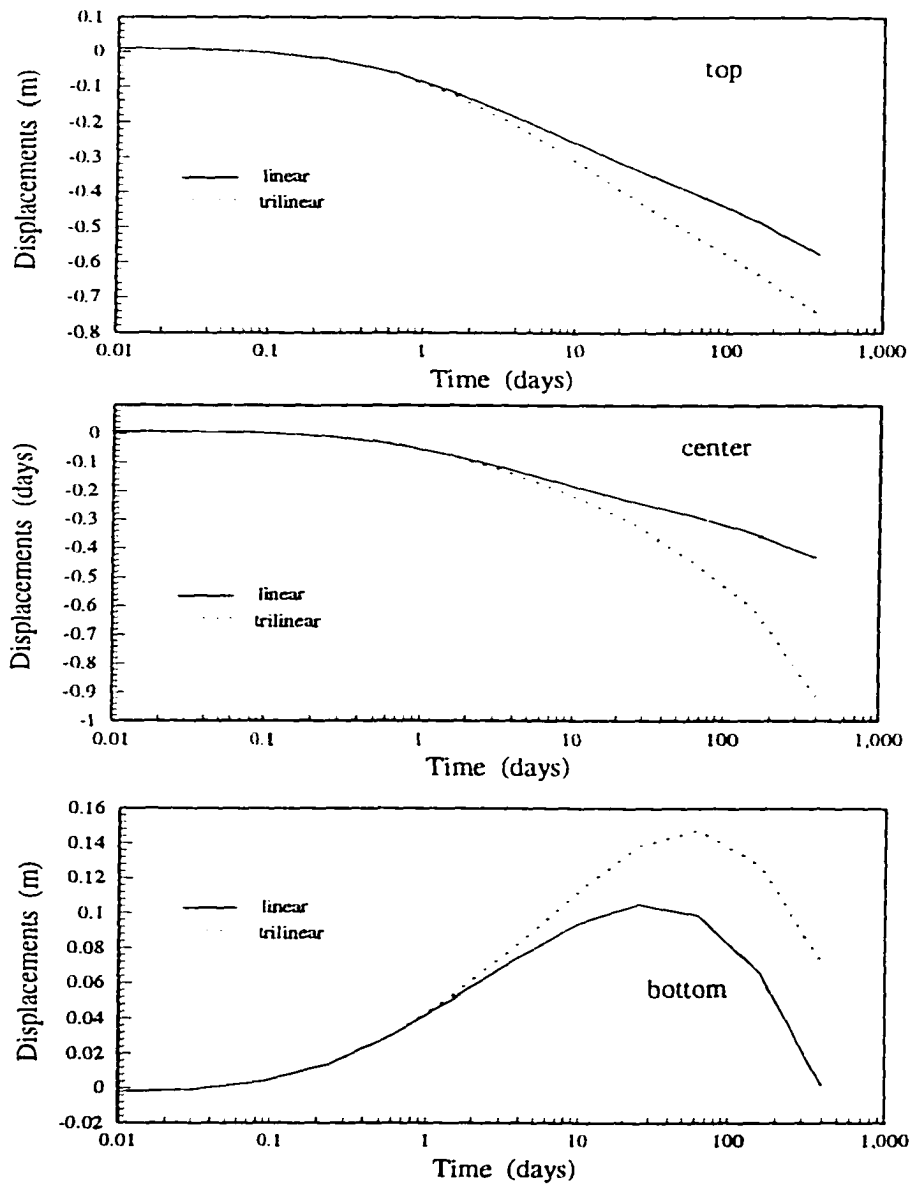
Figure 6.32: Comparison of displacements at a) top, b) center, and c) bottom of the reservoir for a linear and trilinear constitutive equations.
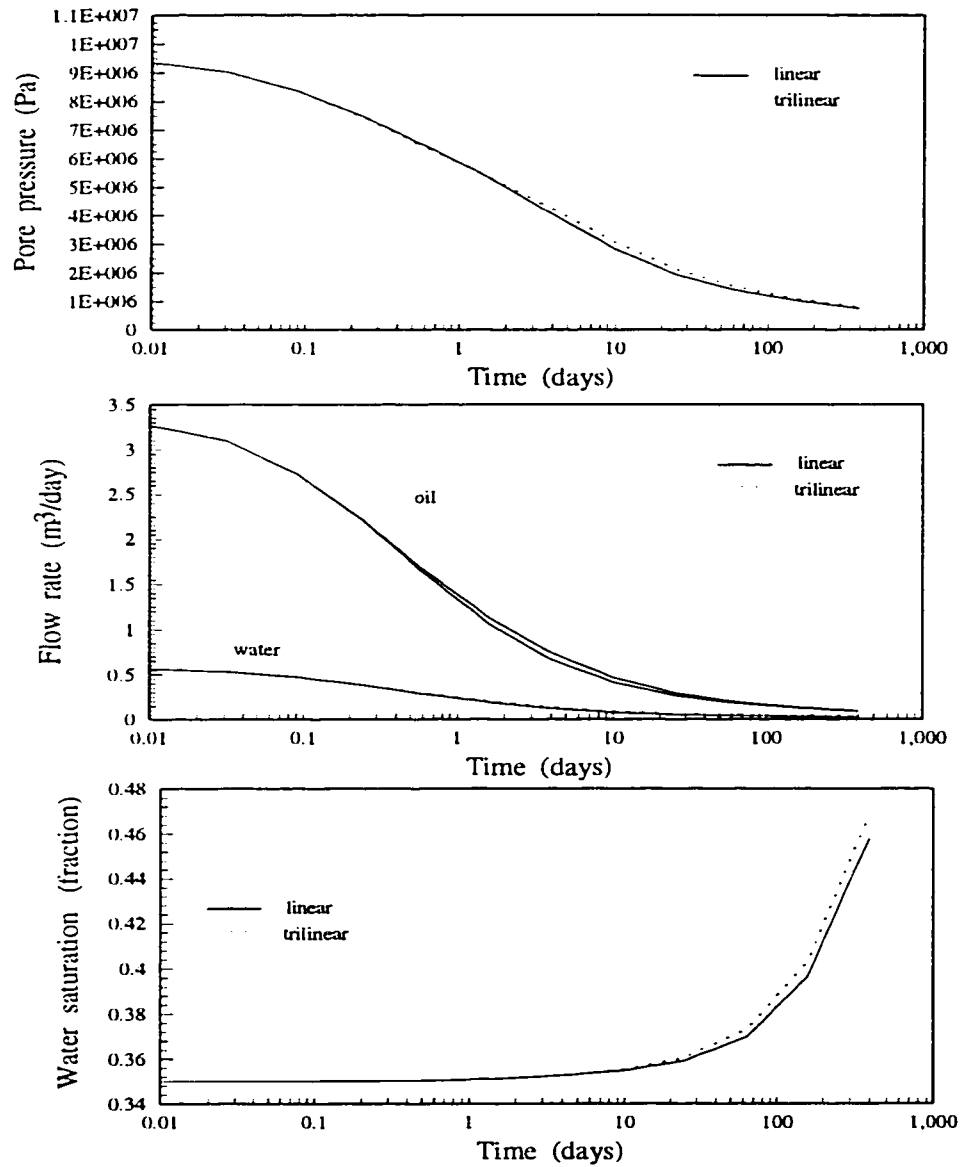
Figure 6.33: Comparison of results for linear and trilinear constitutive equations at the center of the reservoir: a) pore pressure; b) flow rate; and c) water saturation.

164

Chapter 7

Conclusions and Recommendations

In this dissertation, a two-dimensional explicit Lagrangian finite-difference code, fully-coupled with a two-fluid flow system in porous media, is developed. The solid deformation is considered using the dynamic relaxation procedure which allows the model to go into post-peak behavior of the material without creating numerical instability. This method is particularly powerful when deformation is by nonlinear/failure systems (i.e., work softening plasticity). To the author's knowledge, this is the first application of the Lagrangian finite difference method to coupled multi-phase flow in deformable porous media.

Even though such capabilities have been possible by the use of sophisticated finite element codes, the model proposed herein is simpler to use and more efficient when large and nonlinear problems are to be tackled. The reason for this resides in the choice of the numerical technique, as well as

165

solving procedure.

By maintaining strict coupling between the various pertinent mechanisms, the simulator allows studying not only pore pressure and saturation changes over time, but also takes into account capillary effects as well as the influence of in-situ stress conditions. Hence, parametric studies can easily be carried out to delineate the importance of pertinent parameters, helping to select the critical cases.

For a first trivial example, the one-dimensional compaction of a soil column was considered. It was evident that, as the material began to soften, pore pressure was maintained at a higher magnitude for much longer periods of time compared to the classical elastic solutions. This was obviously accompanied by larger deformations. From a practical point of view, this means that the compaction can be considered as a non-negligible driving mechanism and could explain why the reservoir pore pressure does not always decay as predicted. On the negative side, the associated vertical larger displacements might introduce additional shear stresses along the casing, leading to time-dependent buckling failure.

The second, more complex example consisted in a compacting reservoir. Even though such a problem had been considered before, the surrounding rocks masses were never included in the modelling itself but were merely introduced via what was perceived as appropriate boundary conditions. This dissertation clearly proved that this approach is not correct. Once the reser-

166

voir itself starts to compact due to depletion, stresses in the over-, side-, and under-burden changed accordingly, participating in the overall rock mass response. As expected, arching effects started to develop, mainly due to the stiffness contrast between the various layers. Less and less stress was carried by the weak failing member, and more load was transferred to the surrounding formations.

Practically speaking, this means that the consolidation rate will decrease with time and that total stresses in the reservoir will decrease. Pore pressure will also decrease at a faster rate and the associated production will obviously be affected. Moreover, this practical field example revealed a few other phenomena, some of which had been observed in the field but, so far, could not be explained.

- Pore pressure values rising above their original values, even during drawdown. This phenomenon, which occurs at early times, is a poroelastic effect. Uncoupled calculations indeed predict larger depletion and settlements. The simulator can reproduce such a condition by not allowing drainage of the pore pressure.

- Changes in in-situ stress ratios during the reservoir's life. This phenomenon, which was first detected by conducting a number of micro-hydraulic fracturing tests in the Ekofisk field, is also the result of coupled effects. The simulator has clearly shown that this ratio not only varies in time, but in space, too. In addition, this variation is not

167

monotonous and reverses with time. This suggests that a single value of rock compressibility, obtained for a particular stress condition, will not properly represent the stress path in the reservoir. This may provide misleading results, especially when computing the reserves-in-place.

- Reversal of displacements at different locations in the reservoir. This phenomenon is due to the influence of the surrounding layers where pore pressure values are also affected, perturbing the flow patterns and the overall behavior of the rock mass. This is not unexpected as it goes hand-in-hand with floor lifting observed in tabular mining; ore removal is indeed equivalent to considering a reservoir of infinite compressibility.

The observations discussed above clearly show that, when studying compaction of a reservoir due to drawdown or uplift due to injection, it is absolutely necesary to include coupling and also consider the surrounding formations as they fully participate in the overall reaction.

As far as recommendations are concerned, one needs to realize that this simulator is presently limited to two-dimensional situations and two fluid phases. However, as such it could be used to study a number of other applications to check the importance of some particular parameters:

- Study of borehole stability, especially when drilling underbalance. This approach is gaining popularity as it results in lesser formation damage.

- Study of perforation stability when wells are brought onto (and during)

168

production. Collapsed perforations are usually attributed to poor perforation treatments and/or high existing differential stress conditions. This code will allow considering the effect of fluid flow on this problem.

- Study of sanding problems, especially when flow is suddenly interrupted by closing/opening of downstream valves. It is well known that changing flow conditions often result in large temporary (sometimes permanent) sanding rates. The transient flow conditions can be simulated using this code. Another important use of the code in sanding is the study of the influence of water cut into the wells. It is well known that the beginning of water inflow is one of the most important factors, so the inclusion of capillary effects on the overall behavior can now finally be considered with this code.

169

Nomenclature

$\mathbf{a}$ — Acceleration vector

a — Borehole radius

A — Area of integration

b_i — Body force

C — Maximum wave speed

C_p — Dilatational wave speed

dA — Element of area

dL — Element of length

dS — Incremental arc

e — Volumetric strain

$\dot{e}_{ij}$ — Strain rate tensor

$\dot{e}_m$ — Volumetric strain rate

$\dot{e}_d^a$ — deviatoric strain rate for triangle a

f — vector field

170

$< f_{i,j} >$ — element of area

$< f_i^{\overline{12}} >$ — average value of f over side segment 12

f_i^l — value of the function f at the node 1

F — Scalar, vector, or tensor quantity

F_i^{body} — Nodal body force

F_i^{bdry} — Nodal boundary force

$F_i^{internal}$ — Internal nodal force

g_i — Gravitational acceleration

G — Shear modulus

GOR — Gas-oil-ratio

G_{eff} — Effective shear modulus for trilinear behavior

h — heigth over a datum

J — Jacobian

k_{ro} — Relative permeability to oil

k_{rw} — Relative permeability to water

K — Bulk modulus

K_t — Framework bulk modulus

K_s — Solid grains bulk modulus

K_w — Water stiffness

K_n — Oil stiffness

171

L —   Curve bounding an area

m_g —   Lumped gravitational mass at the node

m_{gp} —   Mass for each grid point in the triangle

m_n —   Net ficticious nodal mass

m_t —   Mass associated with the triangle

M —   Total number of sides

M_s —   Solid Mass

n —   outward pointing normal vector

N —   Side number

N —   Side number

P —   Pore pressure

P_c —   Capillary pressure

P_c' —   Slope of the capillary pressure curve

P_n —   Pressure of the non-wetting fluid phase (oil)

P_w —   Pressure of the wetting fluid phase (water)

$\dot{P}_w$ —   Derivative with respect to time of water pressure

P_1, P_2 —   Far field principal stress components

$\mathbf{q}$ —   Darcy's fluid velocity vector

r —   Distance from the borehole center

R_{wi} —   Momentum exchange

172

S —   Arbitrary closed surface or area

S_n —   Saturation of the non-wetting fluid phase (oil)

$\dot{S}_w$ —   Derivative with respect to time of water saturation

S_w —   Saturation of the wetting fluid phase (water)

S_{or} —   Residual oil saturation

S_{wi} —   Irreducible water saturation

S_{wo} —   Initial water saturation

S_{no} —   Initial oil saturation

S_w —   Saturation the wetting fluid phase (water)

S_n —   Saturation on the wetting fluid phase (water)

t_i —   traction vector

u_i —   solid velocity

u_r —   Radial displacements for the borehole problem

u_θ —   Tangential displacements for the borehole problem

U_{wi} —   Intrinsic water velocity vector

U_{ni} —   Intrinsic oil velocity vector

v_i —   oil velocity

V_s —   Solid volume

w_i —   water velocity

w_{ij} —   rotation tensor

173

x_i	—	Average value of the derivative of the vector
α	—	Biot Poroelastic coefficient
β	—	Damping term
δ_{ij}	—	delta of Kronecker
ΔS	—	Length of side segment
Δt	—	Real time step
Δt^*	—	Pseudo time step
Δx_{max}	—	Largest side of the triangle
ϵ	—	Minimum length of the zone edges or diagonals
ϵ_m	—	Radius of Mohr's circle of strain
ϵ_{m1}	—	Strain corresponding to peak value in stress-strain curve
ϵ_{m2}	—	Strain corresponding to start of residual strength
$\Lambda_{w_{ij}}$	—	Water mobility
$\Lambda_{v_{ij}}$	—	Oil mobility
μ_w	—	water viscosity
μ_n	—	oil viscosity
ν	—	Poisson's ratio
ω_{max}	—	Highest natural angular frequency of the undamped mesh
ϕ	—	Porosity
ρ_s	—	solid density

174

ρ_w — wetting fluid (water) density

ρ_w — non-wetting fluid (oil) density

ρ — mass density

σ_{ij} — Total stress tensor

σ'_{ij} — Effective stress tensor

σ_{xx}, σ_{xy} — Cartesian components of the stress tensor

σ_r — Radial component of the stress tensor

σ_θ — Tangential component of the stress tensor

$\dot{\sigma}_{ij}$ — co-rotational stress rate tensor

$\tau_{r\theta}$ — Shear component of the stress tensor

r_m — radius of Mohr's circle of stress

References

[1] Aadnoy B.S.: "A complete elastic model for fluid induced and in-situ generated stresses with the presence of a borehole", *Energy Sources*, Vol 9, pp.239-259, 1987.

[2] Aktan, T. and Ali, F.S.M.: "Finite element analysis of temperature and thermal stresses induced by hot water injection", *Trans. Society of Petroleum Engineers of AIME*, December, 1978.

[3] Ali, F.S.M. and Blunschi, J.: "Cyclic steam stimulation with formation parting", *Pet. Soc. of CIM* paper 83-34-45, presented at the 34th Annual Tech. Mtg., Banff, Alberta, 1983.

[4] Anderson, D.A., Tannehill, J.C., and Pletcher, R.H.: *Computational fluid mechanics and heat transfer*, Series in computational methods in mechanics and thermal sciences. Mimkowics, W.J. and Sparrow, E.M.,Editors, Taylor and Francis, 1980.

[5] Aziz, K. and Settari, A.: *Petroleum reservoir simulation*, Applied Science Publishers, Ltd, London, 1979.

[6] Bear, J. and Bachmat, Y.: "Transport phenomena in porous media - Basic equations", *Fundamentals of transport phenomena in porous media*, (Bear, J. and Corapcioglu, M.Y., eds.), NATO ASI series, Nijhoff, Dordrecht, 5-61, 1984.

[7] Bedford, A. and Drumheller, D.S.: "Theories of immiscible and structured mixture", *Int. J. Engng. Sci.*, 21, 863-960, 1983.

[8] Biot, M. A.: "Theory of three-dimensional consolidation", *J. Appl. Phys.*, 12, 155-164, 1941.

[9] Biot, M. A.: "Theory of elasticity and consolidation for a porous anisotropic solid", *J. Appl. Phys.*, 26, 182-185, 1955.

[10] Biot, M. A.: "Theory of deformation of a porous viscoelastic anisotropic solid", *J. Appl. Phys.*, 27, 452-469, 1956.

[11] Biot, M. A.: "Theory of propagation of elastic waves in fluid saturated porous solids", *J. Acoustical Soc. Am.* 28, 168-191, 1956.

[12] Bowen, R.M.: "Theory of mixtures", in Eringen Ed.,*Continuum physics*, Vol III, Academic Press, N.Y., 1976.

[13] Boade, R.R., Chin, L.Y. and Siemers,W.T.: "Forecasting of Ekofisk reservoir compaction and subsidence by numerical simulation", *JPT*, 723-728, 1989.

177

[14] Burridge, P. B.: "Failure of slopes", *Ph. D. Thesis*, California Institute of Technology, Pasadena, California, 1987.

[15] Brand. C.W. and Heinemann, Z.E.: "Fundamentals of griding techniques in reservoir simulation". paper presented at the *Fourth International Forum on reservoir simulations*, Salzburg, Austria, SPE, 1992.

[16] Chang,Y.W., and Gvildys, J., REXCO-HEP: "A two-dimensional computer code for calculating the primary system response in fast reactors", *Argonne National Lab., ANL/RAS-75-11*, 1975.

[17] Cheng H. and Dusseault, M.B.: "Development and application of a fully-coupled two-dimensional finite element approach to deformation and pressure diffusion around a borehole", *Journal of Canadian Petroleum Technology*, Vol. 32, No. 10, pp. 28-38, Dec., 1993.

[18] Chin, L.Y. and Boade, R.R.: "Full-field, three-dimensional finite-element subsidence model for Ekofisk", *Third North Sea chalk symposium*, Copenhagen, June, 1990.

[19] Chin, L.Y., Boade, R.R., Prevost,J.H. and Landa, G.H.: "Numerical simulation of shear-induced compaction in the ekofisk reservoir", *Int. J. Rock Mech. Sci. & geomech. Abts.*, Vol. 30, No. 7, pp. 1193-1200, 1993.

[20] Chin, L.Y., Boade, R.R., Nagel, N.B. and Landa, G.H.: "Numerical simulation of Ekofisk reservoir compaction and subsidence: treating the

mechanical behavior of the overburden and reservoir", *Eurock'94*, pp 787-794, 1994.

[21] Cleary, M.P.: "Fundamental solutions for a fluid-saturated porous solid", *Int. J. Solids Struc.* Vol. 13, pp. 785-806, 1977.

[22] Collins, R.E.: *Flow of fluids through porous materials*, Research and Engineering Consultant, Englewood, Colorado, 1961.

[23] Corey,A.T., Rathjens,C.H., Henderson,J.H. and Wyliie,M.R.: "Three-phase relative permeability", *Trans. Society of Petroleum Engineering of AIME*, 207, 349-351, 1956.

[24] Crichlow, H.: *Modern reservoir engineering* Prentice Hall, Inc., Englewood Cliffs, NJ, 1978.

[25] Cundall, P.: FLAC, Version 3.0 Users manual, 1984.

[26] Cundall, P.A.: "Report on Nessi and user's manual", *Shell research KSPEL*, Rijswjk, July, 1984.

[27] Cheng, A.H-D. and Ligget,J.A.: "Boundary integral equation method for linear porous-elasticity with application to fracture propagation", *Int. J. Numer. Meth. Engng.*, Vol. 20, pp. 279-296, 1984.

[28] Day, A.S.: "An introduction to dynamic relaxation:, *The Engineer*, London, vol 219, pp. 218-221, 1965.

[29] Derski,W., Izbicki R., Kisiel I. and Mroz Z.: *Rock and soil mechanics*, Developments in Geotechnical Engineering. Vol 48. Elsevier, 1989.

[30] Detournay, E. and Cheng, A.H-D.: "Poroelastic solution of a plane strain point displacement discontinuity", *Journal of Applied Mechanics*, Vol. 54, pp. 783-787, December, 1987.

[31] Detournay, E. and Cheng, A.H-D.: "Fundamentals of poroelasticity", *Comprehensive rock engineering*, Principles, Practice and Projects. Vol. 2, Rock Mechanics Continuum modelling. Eds Hudson J.A., Brown E.T., Fairhurst, C. and Hoek,E., 113-171, 1993.

[32] Detournay E. and Cheng A. H-D.: "Poroelastic response of a borehole in a non-hydrostatic stress field", *Int. J. Rock Mech. Min. Sci. & Geomech. Abstr.*, Vol 25, No. 3, pp171-182, 1988.

[33] Detournay, E. and Roegiers, J.-C.:" Some New Examples of Poroelastic Effects in Rock Mechanics," *U.S. Symposium on Rock Mechanics, Tucson, Arizona*, 1978.

[34] Donaldson,E.C., Ewal N. and Singh, B.: "Characteristics of capillary pressure curves", *Journal of Petroleum Science and Engineering*, Vol 6, pp.249-261, 1991.

[35] Ehlers, W. and Kubik, J.: "On finite dynamic equations for fluid saturated porous media", *Acta Mechanica*, Vol. 105, pp. 101-117, 1994.

[36] Finol A. and Ali, S.M.F.: "Numerical simulation of oil production with simultaneous ground subsidence", *Soc. Pet. Eng. J.*, 411-424, 1975.

[37] Fung, L.S.K., Buchannan, L. and Wan, R.G.: "Coupled geomechanical-thermal simulation for deforming heavy-oil reservoirs", *Proc. CIM Annual Tech. Conf.* Calgary, pp. 36-1 through 36-16, 1992.

[38] Giroux, E.D.: *HEMP Users manual*, Lawrence Livermore Lab., UCRL-51079, 1981.

[39] Gnirk, P.F.: "The mechanical behaviour of uncased wellbores situated in elastic/plastic media under hydrostatic stresses", *Society of Petroleoum Engineers Journal*, 49-59, Feb., 1972.

[40] Goudreau, G.L. and Hallquist J.O.: "Recent developments in large-scale finite element lagrangian hydrocode technology", *Computer Methods in Applied Mechanics and Eng.*, Vol. 33, 725-7757, 1982.

[41] Green, A.E. and Naghdi, P. M.: "A dynamical theory of interacting continua", *Int. J. Eng. Sci.*, 3, 231-241, 1965.

[42] Green, A.E.: "On basic equations for mixtures", *Quart. J.Mech. Appl. Math.*, 22, 427-438, 1969.

[43] Gurtin, M.E.: *An introduction to continuum mechanics*, *Academic Press*, New York, 1981.

[44] Guterrez, M. and Hansteen, H.: "Fully coupled analysis of reservoir compaction and subsidence", *European Petroleum Conference, SPE 28900*, London, Oct. pp 339-347, 1994.

[45] Hancock, S.L.:"Equations for forces in axisymmetric Lagrange zones", *International Conference on computational methods in nonlinear mechanics*, Austin, Texas, 1979.

[46] Hancock, S. L.: "Finite difference equations for PISCES 2DELK, A coupled Euler-Lagrange continuum mechanics computer program", *Physics Intl. Co.*, Tech Memo TCAM, 76-2, 1976.

[47] Hancock, S.L.: "Finite difference equations for PISCES 2DELK, a coupled Euler-Lagrange continuum mechanics computer programs", *Physics Intl. Co.*, Tech Memo TCAM 76-2, 1976.

[48] Hassanizadeh, M. and Gray, W.G.: "General conservation equations for multiphase systems: 1. Averaging procedure", *Adv. Water Resources*, 2, 131-144, 1979.

[49] Hassanizadeh, M. and Gray, W.G.: "General conservation equations for multiphase systems: 3. constitutive equations for porous media flow", *Adv. Water Resources* , 25-40, 1989.

[50] Hassler, G. L. and Brunner, E.: "Measurement of capillary pressures in small core samples", *Trans., AIME*, 160, pp. 114-23, 1945.

[51] Herrmann, W., and Bertholf, L.D., "Explicit Lagrangian Finite-difference methods", *Computational methods for transient analysis*, Belytschko, T. and Hughes, T.J.R., eds., Elsevier Science Publishers, Amsterdam, pp 361-416, 1983.

[52] Hildebrand, F.B.: *Finite difference equations*, Prentice Hall, Englewood Cliffs, NJ, 338 pp, 1958.

[53] Jaeger, J.C. and Cook, N.G.W.: *Fundamentals of rock mechanics*, Chapman and Hall, London, 1969.

[54] Jing L., Tsang, C.-F. and Stephansson, O.: DECOVALEX -An International Co-operative Research Project on Mathematical Models of Coupled THM proccesses for safety analysis of radioactive waste repositories. *International J. Rock Mech. Min. Sci. & Geomech. Abst.* Vol 32, No. 5, pp-389-398, 1995.

[55] Jones, M. and Mathiesen, E.: "Pore pressure change and compaction in North Sea chalk hydrocarbon reservoirs", *Int. J. Rock Mech. Min. Sci. & Geomech. Abstr.*, Vol. 30, No. 7, pp 1205-1208, 1993.

[56] Killins, C. R., Nielson, R. F. , and Calhoun, J. C. Jr.: "Capillary desaturation and imbibition in rocks", *Proc. Monthly*, Vol. 18, No. 2, 30-39, 1953.

[57] Jones, M.E., Leddra, M.J. and Potts, D.: "Ground motions due to hy-drocarbon production from the chalk", *Proceedings of the International Chalk Symposium*, London, pp. 341-347, 1990.

[58] Last, N.C. and Harkness, R.M.: "Explicit Finite difference technique ap-plied to geomechanics. Part I: Continua", *Advanced Geotechnical Anal-ysis*, Chapter 8, Banerjee and Butterfield, Editors, 1993.

[59] Last, N.C. and Harkness, R.M.: "Kinematic (or hourglass) mode control for a uniform strain quadrilateral by an assumed strain technique", *Int. J. Num. Analyt. Met. Geomech.*, Vol 13, pp 381-410, 1989.

[60] Leddra, M.J., Jones, M.E. and Goldsmith, A.S.: "Laboratory investiga-tions of the compaction of chalk under conditions of increasing effective stress", *Proceedings of the Third North Sea Chalk Symposium*, Session 3, paper 4, 36 pages. NPD, Stavanger, Norway, June, 1990.

[61] Lewis,R.W. and Schrefler, B.A.: "The finite element method in the deformation and consolidation of porous media", *Wiley and Sons*, In-terscience Publication, New York, 1986.

[62] Lewis, R.W. and Sukirman, Y.: *Finite element modelling of three-phase flow in deforming saturated oil reservoirs, International Journal for Nu-merical and analytical methods in geomechanics*, Vol. 17, pp. 577-598, 1993.

[63] Li, S., Li, Y., Li, Y., Wu, Z. and Zhou, G.: "Permeability-strain equations corresponding to the complete stress-strain path of Yinzhuang sandstone", *Int. J. Rock Mech. Min. Sci. and Geomech. Abst.*, Vol. 31, No. 4, pp. 383-391, 1994.

[64] Li, X., Zienkiewicz, O.C. and Xie, Y.M.: "A numerical model for immiscible two-phase fluid flow in a porous medium and its time domain solution", *International Journal for Numerical Methods in Engineering*, Vol 30, 1195-1212, 1990.

[65] Li, X., Zienkiewicz, O. C. and Xie, M.: "A numerical model for immiscible two-phase fluid flow in a porous medium and its time domain solution", *International Journal for numerical methods in Engineering*, Vol. 30, 1195-1212, 1990.

[66] Li, X. and Zienkiewicz, O. C.: "Multiphase flow in deforming porous media and finite element solutions", *Computers & Structures*, Vol. 45, No. 2, 211-227, 1992.

[67] Li, X.: "Finite-element analysis for immiscible two-phase fluid flow in deforming porous media and an unconditionally stable staggered solution", *Communications in applied numerical methods*, Vol. 6, 125-135, 1990.

[68] Maenchen, G. and Sack, S.: "The TENSOR code", *Meth. Comp. Phys.*, 3, pp. 181-210, 1964.

185

[69] Marti, J. and Cundall, P.: "Mixed discretization procedure for accurate modelling of plastic collapse", *International Journal for Numerical and Analytical Methods in Geomechanics*, Vol. 6, pp. 129-139, 1982.

[70] Mase, G.E. *Continuum mechanics for engineers*, Boca Raton:CRC Press, 1992.

[71] Mase, G.E.: *Theory and problems of continuum mechanics*, Schaum Outlines, McGraw-Hill Inc.

[72] Mattax, C.C. and Dalton, R.L.(eds), *Reservoir simulation*, Monograph volume 13, SPE, Henry L. Doherty Series, 1989.

[73] Meehan, N.: "Rock mechanics issues in petroleum engineering", *Proceedings of NARMS I*, Austin, Texas, 1993.

[74] Merle A., Kenthie,G.H., Opstal van, G.H.C. and Schneider, G. M. H.: "The bachaquero-study: a composite analysis of the behavior of a compaction drive/solution gas drive reservoir", *J. Pet. Tech.*, 1107-1114, 1976.

[75] Meroi, E. A., Schrefler, B. A. and Zienkiewicz, O. C.: "Large strain static and dynamic semi-saturated soil behavior", *Int. Journal for Numerical and Analytical Methods in Geomechanics*, Vol. 19, pp. 81-106, 1995.

[76] McLellan, P.J. and Wang, Y.: "Predicting the effects of pore pressure penetration on the extent of wellbore instability: application of a versatile poro-elastoplastic model", Eurock'94, Balkema Rotterdam,Holland, 1994.

[77] Nagtegaal, J.C., Parks, D.M. and Rice, J.R.: "On numerical accurate finite element solutions in the fully plastic range" *Comp. Mech. in Appl. Mech. and Eng.*, 4, 153-177, 1984.

[78] Naylor, D.J., Pande, G.N., Simpson, B. and Tabb, R.: *Finite elements in Geotechnical Engineering*, Pineridge Press, Swansea, UK, 1981.

[79] Needleman, A. and Tvergaard, V.: On the finite element analysis of localized plastic deformation, *Finite Elements - Special problems in solid mechanics 5*, in J.T. Oden and G.F. Carey, Eds., Prentice-Hall, ENglewood Cliffs, NJ., 115-142, 1981.

[80] Ortiz, M., Leroy, Y. and Needleman, A.: A finite element method for localized failure analysis, *Computational Meth. Appl. Mech. Engng.*, Vol. 61, pp. 189-214, 1987.

[81] Otter,J.R.H. and Cassell, A.C.: "Dynamic relaxation", *Proc. Instn Civ. Engrs*, 35 pp 633-656, 1965.

[82] Owens, W.W. and Archer, D.L.: "The effect of rock wettability on oil-water relative permeability relationships", *Trans. SPE of AIME. JPT*, 251,pp. 873-878, 1971.

[83] Papadrakakis, M. A.: "Method for the automated evaluation of the dynamic relaxation parameters", *Computer Methods in Appl. Mech. and Eng.*, Vol. 25, pp. 35-48, 1981.

[84] Papanastasiou, P.C. and Vardoulakis, I.V.: "Numerical treatment of Progressive Localization in relation to Borehole stability", *Int. Journal for Numerical and Analytical Methods in Geomechanics*, Vol. 16, pp. 389-424, 1992.

[85] Papanastasiu, P C.: "Numerical Analysis of Localization Phenomena with Application in deep Borehole", Ph D. Thesis, University of Minnesota, 1990.

[86] Paslay, P.R. and Cheatham, J.B.: "Rock stresses induced by flow of fluids into boreholes", *SPEJ*, pp. 85-94, March, 1963.

[87] Patankar, S.V.:*Numerical heat transfer and fluid flow*, in Minkowycs, W.J. and Sparrow E.M. eds., Series in computational methods in mechanics and thermal sciences, Hemisphere,Washington, DC., 1980.

[88] Potts, D., Jones, M.E. and Berget, O.P.: "Subsidence above the Ekofisk oil reservoir", *Proceedings of the international conference on behavior*

188

of off-shore structures, 1 (Geotechnics), pp. 113-127, Tapir, Trondheim, Norway, 1988.

[89] Press, W.H., Flannery, B.P., Teukolsky, S.A. and Vetterling, W.T.: *Numerical recipes. The art of Scientific Computing, (Fortran Version)*, Cambridge University Press, New York, 1990.

[90] Prevost, J.: "Mechanics of continuos porous media", *Int. J. Engng. Sci.*,Vol 18, pp. 178-800, 1980.

[91] Purcell,W.R.: "Capillary pressures- Their measurement using mercury and the calculation of permeability therefrom", *Trans., AIME*, 186, pp. 39-48, 1949.

[92] Rice, J. R. and Cleary, M. P.: "Some basic stress-diffusion solutions for fluid saturated elastic porous media with compressible constituents", *Reviews of Geophysic and Space Physics*, Vol. 14, No. 2, May, 1976.

[93] Rothenburg, L., Bratli, R.K. and Dusseault, M. B.: "A poro-elastic solution for transient fluid flow into a well", *JPT*, pp. 1272-1278, October, 1991.

[94] Rudnicky, J.W.: "On Fundamental solutions for a fluid-saturated porous solid", *Int. J. Solids Structures*, Vol 17, pp. 855-857, 1981.

[95] Rudnicky, J.W.: "Fluid mass sources and point sources in linear elastic diffusive solids", *Mechanics of Materials*, Vol. 3, 243-250, 1987.

[96] Schrefler, B.A., Simoni, L., Li, X. and Zienkiewicz, O.C.: "Mechanics of partially saturated porous media", *Numerical methods and constitutive modelling in geomechanics*, CISM Lecture notes, eds. Desai, C.S. and Gioda, G.,169-209, Springer Verlag, Wien, 1990.

[97] Sharma, M.: *Petrophysics lecture notes*, CEPET PDVSA, Venezuela, 1990.

[98] Settari. A. and Mouritz, F.M.: "Coupling of geomechanics and reservoir simulation models", *Computer Methods and Advances in Geomechanics* pp. 2151-2157, 1994.

[99] Settari, A., Ito, Y. and Jha, K.N.: "Coupling of a fracture mechanics model and thermal reservoir simulator for tar sands", *Can. J. Petrol. Tech.*, V. 31, No. 9, pp. 20-28, 1992.

[100] Settari, A. and Aziz, K.A.: "Computer model for two-phase coning simulation", *Soc. Petrol. Eng. J.*, Vol. 14, No. 3, pp. 221-36, 1974.

[101] Silling, S. A.: "Finite difference modeling of phase changes and localization in elasticity". *Computer Methods in Applied Mechanics and Eng.*, Vol. 70, 251-273, 1988.

[102] Silling, S. A.: "Numerical studies of loss of ellipticity near singularities in an elastic material",*J. Elasticity*, 19, 213-239, 1988.

190

[103] Silling, S. A.:"Incompressibility in Dynamic Relaxation",*Journal of Applied Mechanics*, Vol. 54,539, 1987.

[104] Silling, S. A.: " Singularities and phase-transitions in elastic solids", *Numerical Studies and stability analysis*, Ph.D. Thesis, California Institute of Thechnology, Pasadena, California, 1986.

[105] Silva, A.A. and Toscas, C.: "Analysis of reservoir compaction and subsurface subsidence using an elastoplastic critical state soil model", *Rev. Tech. Intevep*, 4(1), 35-40, 1984.

[106] Slobod,R. L., Chambers, A. and Prehn,W. L. Jr.: "Use of centrifuge for determining connate water, residual oil and capillary pressure curves of small core samples", Trans., AIME, 192, pp. 127-34, 1951.

[107] Snell, R.W.: "Three-phase relative permeability permeability in unconstituted sand", *J. Inst. Petrol.*, 84, pp. 80-88, 1962.

[108] Sonier, F., Besset, P.H. and Ombret, R.: "A numerical model of multiphase flow around a well", *Soc. Petrol. Eng. J.*, Vol. 13, No. 6, pp 311-20, 1973.

[109] Stone, H. L.: "Probability model for estimating Three-phase relative permeability", *JPT*, Trans. AIME, 249, 1970.

[110] Strauss, W.A.: *Partial differential equations. An introduction*, John Wiley and sons, Inc. New York, 1992.

191

[111] Sukirman, Y. and Lewis, R.W.: "A finite element solution of a fully coupled implicit formulation for reservoir simulation", *International Journal for Numerical and Analytical Methods in Geomechanics*, Vol. 17, pp. 677-698, 1993.

[112] Sulak, R.M., Thomas, L. and Boade, R.R.: "Three-dimensional reservoir simulation of Ekofisk compaction drive", *JPT*, pp. 1272-1278, October, 1991.

[113] Szabo, M. T.: "New methods for measuring imbibition capillary pressure curves and electrical resistivity curves by centrifuge", *Soc. Pet. Eng. J.*, 243-52, June, 1974.

[114] Tejchman, H., and Wu, L.:, "Numerical study on patterning of shear bands in a Cosserat continuum", *Acta Mechanica* 99, 61-74, 1993.

[115] Terzaghi, K.: *Theoretical soil mechanics*, Wiley, New York, 1943.

[116] Teufel, L.W., Rhett, D.W. and Farrell, H.E.: "Effect of reservoir depletion and pore pressure drawdown on in-situ stresses and deformation in the Ekofisk Field, North Sea", *Rock mechanics as a multidisciplinary science*, Proceedings of the 32nd U.S. Symposium, Ed. J.-C. Roegiers, pp. 63-72, 1991.

[117] Teufel, L.W. and Rhett, D.W.: "Geomechanical evidence for shear failure of chalk during production of the Ekofisk field", *SPE 22755*,

66th. annual technical conference and exhibition of the SPE, Dallas, Tx . October 6-9, 1991.

[118] Tortike, W. S. and Ali, F.S.M.: "A framework for multiphase non-isothermal fluid flow in a deforming heavy oil reservoir", *Society of Petroleum Engineers 16030* Ninth SPE Symposium on reservoir simulation, San Antonio, Texas, February 1-4, 1987.

[119] Tortike, W.S. and Ali, F.S.M.: "Modelling thermal, three-dimensional, three-phase flow in a deforming soil", *Numerical methods in geomechanics*. Swoboda, Eds., Innsbruck, 1988.

[120] Truesdell, C. and Toupin, R. A.: "The classical field theories", in S. Flugge (Ed.), *Handbuch der Physic, Bd III/I* Springer-Verlag, 1960.

[121] Underwood,P.: "Discussion on dynamic relaxation", *Computational methods for transient analysis* Belytschko, T. and Hughes,T.J.R.,eds., Elsevier Science Publishers, Amsterdam Holland, pp 245-265, 1983.

[122] Vardoulakis, I. V. and Papanastasiou, P.C.: "Bifurcation analysis of deep boreholes:I. Surface instabilities", *International Journal for Numerical and Analytical Methods in Geomechanics*, Vol 12, 379-399, 1988.

[123] Vazari, H.H.: "Theoretical analysis of stress, pressure and formation damage during production", *Journal of Canadian Petroleum Technology*, pp.111-117, Nov-Dec, 1988.

[124] Verruijt, A.: "Generation and dissipation of pore-water pressures", *Finite Elements in Geomechanics*, Ch. 9 p-293-317, 1987.

[125] Wang,Y. and Dusseault, M.B.: "Borehole yield and hydraulic fracture initiation in poorly consolidated rock strata - Part II. Permeable media", *Int. J. Rock Mech. Min. Sci. and Geomech Abstr.*, Vol.28, No. 4, pp 247-260, 1991.

[126] Wilkins, M.L.: "Calculation for elastic-plastic flow", *Lawrence Radiation Laboratory*, Report UCRL-7322, 1969.

[127] Willhite,G. P., *Waterflooding*, SPE Textbook Series, Richardson, TX., 1986.

[128] Yanguan, Y.G. and Abousleiman, Y.: "Poroelasticity capacity in ABAQUS", *Report RMC-93-05*, Rock Mechanics Consortium, University of Oklahoma, School of Petroleum and Geological Engineering, 1993.

[129] Zienkiewicz, O. C. and Shiomi, T.: "Dynamic behaviour of staurated porous media, the generalized Biot formulation and its numerical solution", *International Journal for Numerical and Analytical Methods in Geomechanics*, Vol 8, 71-96, 1984.

194

[130] Zienkiewicz, O.C. and Taylor, R.L.: "Coupled problems-a simple time stepping procedure", *Communications in Applied Numerical Methods*, Vol. 1, 233-239, 1985.

[131] Zienkiewicz, O.C. , Wood, W.L., Hine, N.W., and Taylor, R.L.: "A unified set of single step algorithms. Part 1: General formulation and applications", *International Journal for Numerical Methods in Engineering*, Vol. 20, 1529-1552, 1984.